EPFL

Thèse n° 8422

A novel approach for SPICE modeling of light and radiation effects in ICs

Présentée le 29 janvier 2021

à la Faculté des sciences et techniques de l'ingénieur
Groupe de scientifiques IEL
Programme doctoral en microsystèmes et microélectronique

pour l'obtention du grade de Docteur ès Sciences

par

Chiara ROSSI

Acceptée sur proposition du jury

Prof. C. Dehollain, présidente du jury
Dr J.-M. Sallese, directeur de thèse
Prof. M. Rudan, rapporteur
Prof. B. Iñiguez, rapporteur
Prof. C. Enz, rapporteur

École
polytechnique
fédérale
de Lausanne

2021

Above all, don't fear difficult moments.
The best comes from them.
— Rita Levi-Montalcini

To my family

Acknowledgements

First of all, I would like to thank my thesis supervisor Jean-Michel Sallese, without whom this work would not have been possible. I am extremely grateful for his guidance and precious advice, and I would like to thank him for having always supported and encouraged me in this four years, for having taught me so much and fueled my passion for research.

I am thankful to the jury members of this PhD thesis defense committee, Prof. Christian Enz, Prof. Massimo Rudan, Prof Benjamin Iñiguez and Prof. Catherine Dehollain, for the insightful comments and stimulating discussion, for having examined this thesis and helped me in improving the quality of this manuscript.

I would like to express my gratitude to all my colleagues. Thanks to Jacopo and Georgi: I shared most of the PhD experience with them and they were always there to support me, inside and outside the office. Thank you for your help in so many situations, for your patience in listening to me, for the countless fun moments together and for your precious friendship. I am grateful to Farzan for all his advice and recommendations, for always being ready to help me and available to answer any question I had (and also for taking care of my plants in our office). I also thank Amin, with whom I shared the office during his exchange in EPFL, for our interesting talks and fun moments. Thanks to André, who spent his summer internship working with me, for your commitment and hard work: I was very lucky to have the opportunity to work with a student like you. I am grateful to Rosane, my *conference-mate*, for all the amazing trips (work-related and not), lunches, dinner, coffee breaks and for always offering me her help in any situation.

I am thankful to Pietro and Camillo for their precious help. They explained me everything about their research work, helped me to solve my issues with Cadence and they were always ready to answer all the questions I had, even when they left EPFL.

I would like to acknowledge Cédric Meinen for the assistance in using the server and Raymond Sutter for the IT support. My gratitude goes also to Lucie Auberson, Isabelle Buzzi and Karin James that helped me with all the administrative and bureaucratic issues.

My gratitude also goes to the third floor friends for their support, for the enjoyable corridor chats, meals and coffee breaks and for the amazing time we spent together inside and outside EPFL. Thanks to Nicolò for always welcoming me in his office and at his home, where I could find laughs and hugs but also cheering up in difficult time; thank you for all the fun moments, for your patience during hikes and for your dedication in expanding my cinematographic culture. Thanks to Carlotta, my *afternoon tea-mate*, for all your help, for the quality time together, including the late evenings in the office, and for being the perfect neighbor (I love our boardgame-and-tea nights): thank you for everything we have shared in these years. Thanks to Emanuele for his help and suggestions and for being the *senior PhD* also for me when I needed advice; thank you also for the countless wonderful moments during coffee breaks, dancing rock'n'roll, cooking, playing scopone and much more. Thanks to Matteo, fellow last year PhD student: we were going through this challenging part of the PhD journey almost at the same time and his encouragement, support, comprehension and help were precious to me. Thanks to Luca for the stimulating discussions over coffee, all the food he cooked and all the fun moments spent together. Thank to Maneesha for the cheerful moments, in EPFL and outside, and for always being thoughtful and caring. I am thankful to all the *nanolunchers* for the lunches and coffee breaks together, it was really nice to share this daily time with you.

I want to thank Clarissa, we shared most of our university experience in Torino and I was so lucky that we got to share also the PhD experience. We managed to shorten the distance between Lausanne and Zurich with our phone calls for the latest updates about our journey but also to discuss about feelings, problems and future aspirations.

Huge thanks to Giulia for always being there for me and for being my reference point for any problem I had, providing help, encouragement, understanding and wise recommendations. Thank you for having supported me in these years, for the great time spent together and for our strong friendship.

During my PhD years I shared the flat with wonderful people: Daniel, Elisabetta and Julius. Thank you for the cozy, friendly and welcoming environment you created, for the help with Swiss bureaucracy, for the dinners, parties and evening chats we shared. Thanks also for all the happy moments during the long lockdown that we spent together.

Thanks to Ivan, Nadia, Francesco, Eleonora, Mariazel, for all the dinners, parties, hikes that have made so fun my life outside EPFL. I thank also all the other people I met in EPFL and in Lausanne, I enjoyed a lot the campus events and the vibrant social environment that enriched my PhD experience and also my network.

I would like to thank my friends back in Italy, Alessandra, Giusi, Valentina and Alessandra, that despite the physical distance are always present. Even though the time we could spent together was short, it was of great importance for me. Thank you for your endless friendship.

A very special thank you goes to my parents, my brother and all my family for their love, support, encouragement, help and for always believing in me. Finally, thank you Paride, for your continuous support, for your patience, for always being on my side and for your love.

Abstract

Modeling the interaction of ionizing radiation, either light or ions, in integrated circuits is essential for the development and optimization of optoelectronic devices and of radiation-tolerant circuits. Whereas for optical sensors photogenerated carriers play an essential role, high energy ionizing particles can be a severe issue for circuits, as they create high density of excess carriers in ICs substrate, causing parasitic signals. In particular, recent advances in CMOS scaling have made circuits more sensitive to errors and dysfunctions caused by radiation-induced currents, even at the ground level. TCAD simulations of excess carriers generated by light or radiation are not dedicated to large scale circuit simulations since only few devices can be simulated at a time and computation times are too long. Conversely, SPICE simulations are faster, but their accuracy is strictly dependent on the correctness of the compact models used to describe the devices, especially when dealing with photocurrents and parasitic radiation-induced currents.

The objective of this thesis is to develop a novel modeling approach for SPICE-compatible simulations of electron-hole pairs generated by light and by high energy particles. The approach proposed in this work is based on the Generalized Lumped Devices, previously developed to simulate parasitic signals in High Voltage MOSFET ICs. Here, the model is extended to include excess carriers generation. The developed approach allows physics-based simulations of semiconductor structures, hit by light or radiation, that can be run in standard circuit simulators without the need for any empirical parameter, only relying on the technological and geometrical parameters of the structure, and without any predefined compact model. The model is based on a coarse mesh of the device to obtain an equivalent network of Generalized Lumped Devices. The latter predicts generation of excess carriers and their propagation, recombination and collection at circuit nodes through the definition of equivalent voltages, proportional to the excess carrier concentrations, and equivalent currents, proportional to the excess carrier gradients. The model is validated with Sentaurus TCAD numerical simulations for different scenarios. Regarding light effects, the proposed strategy is applied to simulate various optoelectronic devices. Complete DC

I-V characteristics of a solar cell and transient response of a photodiode are studied. Next, phototransistors are considered. After, a full pixel of a 3T-APS CMOS image sensor is analyzed. The photosensing device, described with Generalized Devices, is co-simulated with the in-pixel circuit, described with compact models. The impact of semiconductor parameters on pixel output and on crosstalk between adjacent pixels is predicted. Finally, radiation-induced soft errors in ICs are examined. Alpha particles at different energies hitting the substrate are simulated. Parasitic currents collected at contacts are studied as a function of particles position and energy. Funneling effect, which is a phenomenon specific to high injection, is also included in the model.

This work shows that the Generalized Lumped Devices approach can be successfully used for SPICE simulations of optoelectronic devices and for prediction of radiation-induced parasitic currents in ICs substrate. This thesis is a first step towards a complete and flexible tool for excess carriers modeling in standard circuit simulators.

Keywords - SPICE, modeling, Generalized Lumped Devices, optoelectronics, radiation effects, Single Event Effects, ICs, soft errors, solar cell, photodiode, phototransistor, CMOS APS, alpha particles, funneling

Riassunto

Sviluppare modelli accurati per simulare l'interazione della radiazione ionizzante (luce o particelle pesanti) con i circuiti integrati è essenziale per lo sviluppo e l'ottimizzazione di circuiti optoelettronici e di circuiti resistenti alle radiazioni. Mentre i portatori fotogenerati giocano un ruolo fondamentale nei sensori ottici, particelle ionizzanti ad alta energia possono causare danni importanti nei circuiti integrati, dato che generano una alta densità di carica nel substrato, causando segnali parasitici. In particolare, i recenti progressi nella riduzione delle dimensioni dei transistor hanno reso i circuiti più sensibili agli errori causati dalle correnti parassite indotte dalle radiazioni. Le simulazioni numeriche TCAD delle cariche generate dalla luce o dalla radiazione non sono adatte a circuiti complessi con molti transistor, infatti solo pochi dispositivi possono essere simulati contemporaneamente; inoltre, i tempi di simulazione sono molto lunghi. D'altro canto, le simulazioni SPICE sono molto veloci, ma la correttezza dei risultati dipende dalla precisione dei modelli analitici utilizzati per descrivere i singoli dispositivi presenti nel circuito e le correnti generate dalla luce o dalle particelle ionizzanti.

L'obiettivo di questa tesi è lo sviluppo di un nuovo approccio per simulare con software SPICE le coppie elettrone-lacuna generate in una struttura semiconduttiva dalla luce e dalla radiazione. L'approccio proposto è basato sui cosiddetti Generalized Lumped Devices, cioè degli elementi contenenti un modello che vengono interconnessi tra loro per ottenere una descrizione completa di una struttura, che sono stati precedentemente sviluppati per la simulazione di segnali parasitici in circuiti High Voltage MOSFET. In questo lavoro, il modello è esteso per includere la generazione di portatori nel semiconduttore. Il modello sviluppato non è empirico, ma è basato sui modelli fisici dei semiconduttori. Le simulazioni di questo modello possono essere effettuate con simulatori convenzionalmente usati per i circuiti elettronici, senza bisogno di parametri empirici o di fitting ma solo usando i parametri fisici e tecnologici della struttura simulata. L'approccio si basa sulla rappresentazione della struttura tramite un circuito equivalente costruito con i Generalized Lumped Devices. Questi ultimi simulano la generazione di coppie elettrone-lacuna, la loro ricombinazione e il

loro trasporto fino ai contatti elettrici attraverso la definizione di tensioni equivalenti, proporzionali alle concentrazioni dei portatori, e correnti equivalenti, proporzionali ai gradienti delle concentrazioni di portatori. Il modello sviluppato è stato validato per diverse strutture e applicazioni usando simulazioni numeriche, effettuate con il software Sentaurus TCAD. Per quanto riguarda la luce, sono state simulate le caratteristiche di un fotodido, di una cella solare e di un fototransistore. Inoltre, è stato anche studiato un pixel di un sensore CMOS 3T-APS. Il pixel comprende sia il sensore ottico, cioè un fotodiodo, che un circuito di lettura formato da tre transistor. Il fotodiodo è stato descritto dal circuito equivalente di Generalized Lumped Devices mentre i transistor con i modelli compatti tradizionali, che sono stati connessi direttamente al circuito equivalente, in modo da simulare tutto il pixel contemporaneamente. È stato studiato anche l'impatto dei parametri del semiconduttore sull'uscita del circuito di lettura del pixel e sul crosstalk tra due pixel adiacenti. Infine, sono stati analizzati gli errori nei circuiti integrati dovuti alle radiazioni ionizzanti. In particolare, è stata simulata l'interazione tra particelle alfa, con differenti energie, e il substrato di silicio dei circuiti integrati. Le correnti parassite indotte ai contatti elettrici sono state studiate in funzione della posizione e dell'energia della particella alfa. L'effetto di funneling, che insorge quando la concentrazione di portatori è piu alta del doping vicino ad una giunzione p-n, è stato incluso nel modello.

Questa tesi mostra come l'approccio basato sui Generalized Lumped Devices può essere utilizzato per simulare accuratamente i dispositivi semiconduttivi optoelettronici e per predire le correnti parassite indotte nei substrati dei circuiti integrati. Questo lavoro è il primo passo verso lo sviluppo di un "metodo" completo e flessibile per la simulazione delle coppie elettrone-lacuna nei dispositivi elettronici utilizzando software SPICE.

Contents

List of Figures

Acronyms

1D One dimensional.

2D Two dimensional.

3D Three dimensional.

APS Active Pixel Sensor.

CAD Computer-aided design.

CMOS Complementary metal-oxide-semiconductor.

CMOS APS CMOS Active Pixel Sensor.

DD Displacement Damage.

EPFL École Polytechnique Fédérale de Lausanne.

GLD Generalized Lumped Devices.

HVMOSFET High Voltage MOSFET.

ICs Integrated circuits.

LET Linear Energy Transfer.

MCC Minority Carriers Circuit.

MOSFET Metal-oxide-semiconductor field-effect transistor.

PDEs Partial Differential Equations.

SEEs Single Event Effects.

SI International System of Units.

SNS Sah-Noyce-Shockley.

SPICE Simulation Program with Integrated Circuit Emphasis.

SRH Shockley-Read-Hall.

SRIM Stopping and Range of Ions in Matter.

TCAD Technology Computer-Aided Design.

TCC Total Current Circuit.

TID Total Ionizing Dose.

1 Introduction

1.1 Radiation and light effects in semiconductors

The interaction of ionizing radiation, either electromagnetic radiation or ions, with a semiconductor results in the generation of electron-hole pairs, if the energy of the radiation is sufficiently high. This effect can be responsible for severe dysfunctions in electronic components and systems, especially when dealing with particles that are not stopped by the external packaging. The generated charge in the semiconductor causes parasitic signals in circuits, leading to errors in the operation, data disruptions, bit flipping, permanent damages or even complete failure [9, 10, 11, 12, 13]. But radiation effects are not an issue only restricted to space missions or aerospace applications, as recent advances in CMOS transistor scaling have made integrated circuits more susceptible to ground level particles, coming from cosmic rays [14, 15, 16]. However, this charge generation does not only cause undesirable parasitic effects but can also be actively exploited for detection purposes or energy conversion. Examples are photodetectors, such as photodiodes and phototransistors, radiation dosimeters, radiation detectors for particle tracking, and solar cells [3, 17, 18].

The physics mechanisms behind electron-hole pairs generation in semiconductors by ions and photons are different. Ions, that are particles heavier than electrons, cause ionization through a process of inelastic collision with atomic electrons of the target material (Coulomb interaction) [19, 2]. Instead, the process associated to the interaction with light (zero mass photons) is the internal photoelectric effect: the photon is absorbed if its energy is higher than the bandgap and an electron-hole pair is created. For semiconductors with indirect bandgap, phonons are involved in order to conserve momentum [3]. Nonetheless, for what concerns electronic devices and circuits, the ultimate result is the same, i.e. excess carriers in the semiconductor structure, even though with different concentration and space distribution. And the modeling of generation, transport and collection of these excess carriers has a crucial importance in both fields of application for systems reliability.

Following the commonly used expressions in literature, the term *radiation* will be used when referring specifically to ions, not including also electromagnetic radiation, for which the term *light* will be used.

1.2 Simulation of excess charge in devices and circuits

Modeling and simulation have always been widely used in microelectronics during the design phase for rapid prototyping and optimization as they provide insight in the system operation without the long and expensive process of testing. Today, with the scaling of transistor dimensions, integrated circuits contain several billions of transistors and the design of such architectures would not be feasible without software packages that simulate the circuit operation before its fabrication [20]. Computer-aided design (CAD) and computer-aided circuit analysis started in the early 1950's with the first digital computers [21]. Several simulators, based on different algorithms, were developed during the following years but most of them were hard to use and had difficulties in converging [21]. The first SPICE (Simulation Program with Integrated Circuit Emphasis) program was firstly released in 1971, placed into the public domain and presented at a conference in 1973 [22]. SPICE1 evolved from CANCER program, developed during an undergraduate class project in the academic year 1969-1970. SPICE became very popular due to several important characteristics: it was public, it was multipurpose, allowing DC, AC, transient, noise, and sensitivity analyses in the same program (while most of the other programs were quite specific), it was very robust, as the heavy use by students resulted in many improvements, it could handle large circuits and it was written in portable FORTRAN [1]. The program was further developed in the next years. SPICE2 was released in 1975 [23], and SPICE2G6 in 1981, becoming the worldwide industry standard. In 2011, SPICE was named an IEEE Milestone (Fig. 1.1). SPICE simulators are based on devices compact models, i.e. they need analytical models of the components in the circuit. With CMOS transistor scaling, numerical solutions to carriers transport equations started to be required. Several

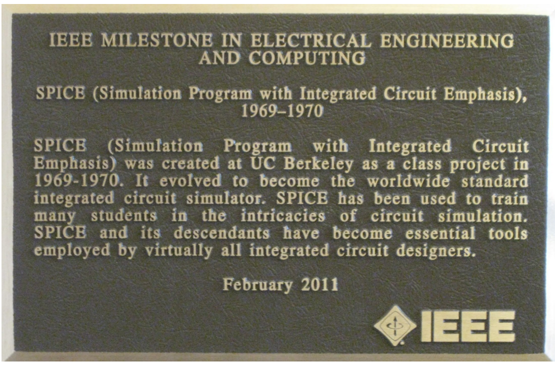

Figure 1.1 – SPICE is an IEEE Milestone (adapted from [1]).

TCAD (Technology CAD), i.e. the numeric simulation of semiconductor processes and devices, software programs were developed, such as MINIMOS [24, 25], HFIELDS [26], FIELDAY [27], CURRY [28], SUPREM and PISCES [29]. With the debut of PISCES II in 1984, numerical device simulation became mainstream. The increase of computational power in modern computers made possible the extensive use of TCAD tools and, as a consequence, the advancement of their complexity and capability. Today, the main suppliers of commercial TCAD tools are Synopsys (Sentaurus) and Silvaco (ATLAS).

Simulation of excess carriers in semiconductor structures, generated by light or radiation, are typically performed using SPICE or TCAD tools. TCAD tools provide full numerical simulations at device level, solving numerically a set of physics equations that model the electrical behavior of a device taking into account its geometry, materials and doping profiles. These equations also model excess charge generation and transport inside a device [2]. The device-under-test is represented with a mesh (example of a mesh is reported in Fig. 1.2), which is used for the linearization of the physics equations (the Poisson equation for the electro-static problem, the continuity equations for the carrier dynamic balance, and one or several equations to treat the transport problem [2]). TCAD simulations are very accurate and give access to internal quantities of the device structure that cannot be measured, helping with the understanding of the underlying physics mechanisms. The significant drawback of this approach is the long computational time, which depends on the mesh number and nature of equations [2]. Moreover, it is not possible to simulate complex circuits with several devices. This latter limitation can be partially overcome by using a mixed-mode approach, in which only a single device of the circuit (for example the one in which radiation-induced charge generation occurs) is simulated numerically while the rest of the circuit is simulated using compact models (see Fig. 1.3). However, the computation time is still quite high and coupling effect between devices are not taken into account. Fast simulations of complex circuits are performed with SPICE simulators, that use compact models to describe the different elementary devices in

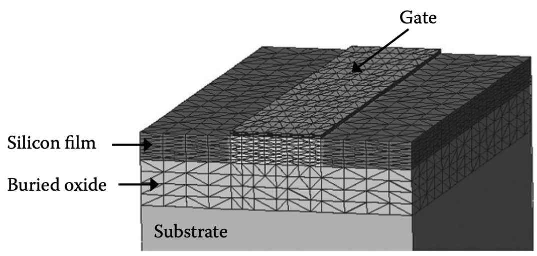

Figure 1.2 – Example of a 3D mesh in an SOI MOSFET for TCAD simulaitons (adapted from [2]).

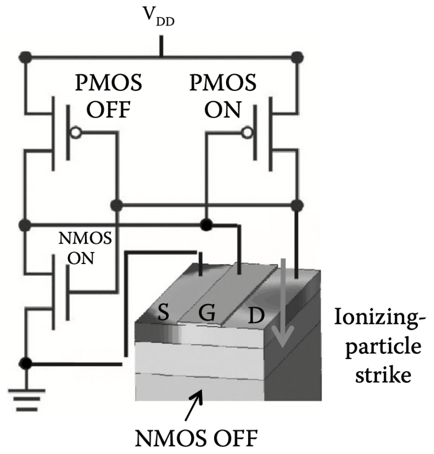

Figure 1.3 – Schematic illustration of the mixed-mode simulation approach (adapted from [2]).

the circuit. Compact models consist in a simplified set of equations that describe analytically the device operation. This result in a short computation time. Excess carriers generated by light or radiation are usually injected in the circuit by means of an equivalent current, using an external current source, as shown in Fig. 1.4. The accuracy of the result depends on the correctness of the models used in the simulation. Compact models often use semiempirical analytical expressions with fitting parameters that have no clear physical meaning. The challenge is thus to extract the correct values of these model parameters. This can be done by using experimental data of real devices or data from device numerical simulations [2, 20].

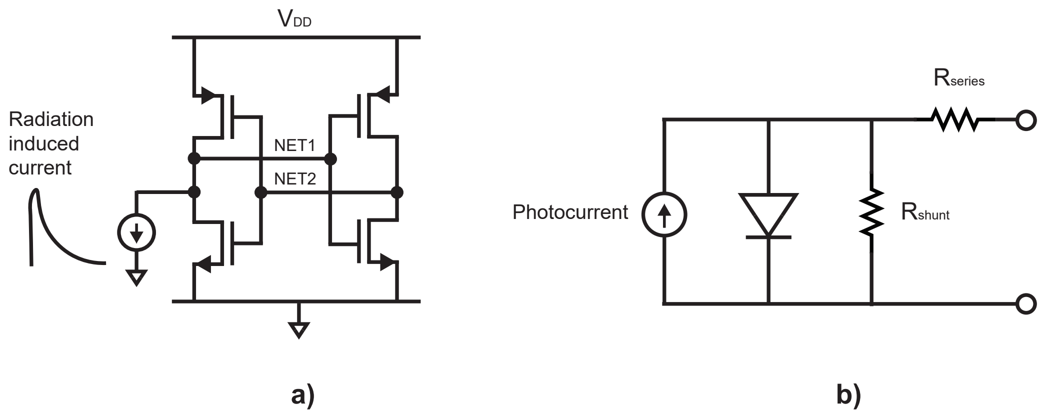

Figure 1.4 – SPICE modeling of generated charges involve the injection of a current in the circuit: a) SRAM hit by radiation, the parasitic current is injected at the struck node; b) solar cell circuit model, the photocurrent is represented by a current source.

1.3 Generalized Lumped Devices modeling approach

The novel SPICE-compatible modeling approach based on the so-called Generalized Lumped Devices was firstly introduced in the framework of the SNF project *"A global approach to model induced minority carrier parasitic currents in HV-MOSFET's integrated circuits"* [30, 31, 32] and then extended in the *Automics* European Project for simulation of parasitic signals in Smart Power ICs using standard circuit simulators [33, 34, 6, 35, 36]. The goal of these works was to obtain a complete description of the ICs substrate, taking into account both drift and diffusion currents, for all injection levels, i.e. simulating both majority and minority carriers. In fact, classical substrate noise analyses were based on the description of ICs substrate with a network of doping dependent resistors and capacitances at the boundaries of PN junctions. The classical approach is valid when only drift current is involved, with no minority carriers, and only for low injection regimes [6].

The novel substrate model based on the Generalized Lumped Devices relies on a semi-compact modeling approach: regions with electric field that rapidly changes in space (PN junction interfaces and MOSFET channel regions) are modeled with compact models while the rest of the substrate is modeled with a distributed model. The distributed model is derived from the discretization (with Finite Difference Method (FDM)) of continuity and drift-diffusion equations, in order to handle the spatial dependency of the system through a meshing scheme of the substrate [6]. The system complexity is reduced by assuming the quasi-neutrality hypothesis: in this way the Poisson equation can be removed and the continuity equation can be solved for just one type of carriers. The FDM is thus only used for the minority carrier continuity equation, which is transformed into a system of algebraic equations whose number depends on meshing. These simplifications imply also that the electric field is piecewise constant, taking a different value in each mesh box but still changing over space. Finally, since the distributed model is applied only where the electric field is slowly changing, the mesh can be much rougher than the one employed in TCAD tools, decreasing considerably the computational time. Solving this linearized continuity equation gives information about minority carrier concentration and gradient. In order to be solved by SPICE-like simulators, these quantities must be transformed in electrical quantities that can be handled by such tools. To this purpose, equivalent voltages and currents are defined: the equivalent voltages are proportional to excess minority carrier concentration and the equivalent currents are proportional to excess minority carrier gradient. Thanks to this definitions, the linearized continuity equation can be described as an equivalent circuit, i.e. the Minority Carriers Circuit (MCC). The MCC is solved directly in SPICE simulators, obtaining information on minority carriers, and the results are used to couple back the effects on *real* currents and

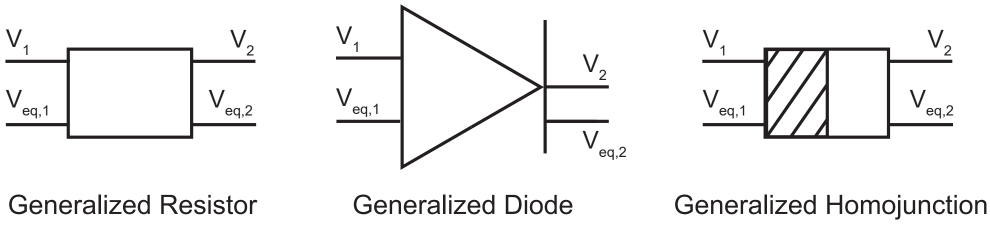

Figure 1.5 – The three Generalized Lumped Devices developed to model minority carrier parasitic currents in HVMOSFET's integrated circuits.

voltages in the substrate, simulated by the Total Current Circuit (TCC). The substrate model is thus composed by a network of Generalized Lumped Devices (connecting the mesh nodes) which embed the MCC and the TCC and have 4 terminals (two for TCC, i.e. real voltages and currents, and two for MCC, i.e. equivalent voltages and currents) [6]. Three different types of Generalized Devices, shown in Fig. 1.5, are derived:

- generalized resistor: to model a piece of substrate with constant doping;
- generalized homojunction: to model the doping discontinuities present at electrical contacts;
- generalized diode: to model the pn junctions.

The result is a comprehensive tool able to correctly simulate propagation, recombination, collection and injection of minority carriers in the substrate of ICs using standard SPICE-like circuit simulators. Moreover, a back-to-back connection of two Generalized Diodes correctly simulates the behavior of a parasitic NPN bipolar transistor while the a front-to-front connection models a PNP bipolar transistor. This is possible thanks to the propagation of minority carriers through the MCC, whereas in standard diode compact model they would be *recombined*, lost at the compact model end pins. The Generalized Devices models have been coded in Verilog-A and the substrate of a HVCMOS benchmark has been simulated with Spectre circuit simulator. The model predictions were verified by both TCAD numerical simulations and experimental measurements [6]. Regarding TCAD simulations, it is important to mention that the same geometry and technology parameters were used for the TCAD structure and the Generalized Devices equivalent substrate network. The latter, in fact, does not need any fitting or empirical parameters. Simulations with Generalized Devices were about 1000 times faster that TCAD simulations. Finally, this novel approach is not dependent on the geometry of the wells in the substrate or on the technology, hence it can be applied to any circuit layout [6].

1.4 Motivation and aim of this work

Modeling of excess carriers in semiconductors is essential for the development and optimization of optoelectronic devices and radiation-tolerant circuits. These latter are increasingly required, as recent advances in CMOS scaling have made circuits increasingly sensitive to errors and dysfunction caused by ionizing radiation. TCAD simulations of excess carriers generated by light or radiation are limited by long computation times. Moreover, specialized TCAD simulators are needed and only few devices can be simulated at a time. Conversely, SPICE simulations are fast but their accuracy is strictly dependent on the correctness of the employed compact models. This is even more relevant for simulation of excess charge: the results depend on the precision of the photo- or radiation-induced current injected in the circuit as stimulus input. The derivation of this current is quite challenging and it is typically done analytically with a certain number of fitting and empirical parameters.

The objective of this work is to extend the substrate modeling approach based on the so-called Generalized Lumped Devices (GLD), previously developed for SPICE simulation of minority carrier parasitic currents in HVMOSFET ICs, to obtain a comprehensive tool that can simulate excess carriers generation, transport and collection in a semiconductor structure. The goal is not to obtain results as precise as TCAD simulations, but to have a flexible and reliable SPICE model that does not depend on specific compact models or on extensive fitting and that provides short computation times. The SPICE compatibility is a key feature of the model, as it allows not only the possibility to simulate excess carriers directly with standard circuit simulators, but also to *co-simulate* any semiconductor structure described using the proposed approach with any external circuit.

The main objective is thus to develop, extend and optimize the Generalized Lumped Devices approach for excess carriers modeling in SPICE environment. The model will be adapted to two different applications:

- simulation of photogenerated carriers in optoelectronic devices;
- simulation of radiation-induced carriers in ICs substrate.

The capability of the model will be tested by simulating a variety of scenarios, starting with optoelectronic devices, such as photodetectors, solar cells, phototransistors and CMOS APS, to conclude with soft-errors prediction in ICs hit by radiation.

1.5 Thesis outline

The thesis is divided into two parts:

Part I presents how the Generalized Lumped Devices model is extended and applied for simulation of light-induced excess carriers in optoelectronic devices.

Chapter 2 provides an overview on light-semiconductor interaction and defines the quantities that will be used. A literature review on SPICE models for simulation of photogenerated carriers and currents with standard circuit simulators is reported. After, the extended Generalized Lumped Devices model, including photogeneration, developed in this work, is described. The full derivation of the model is detailed, including the discretization of continuity and drift-diffusion. The equivalent circuits describing the Generalized Lumped Devices internal models are depicted. The novel Generalized Devices, i.e the Surface Recombination Element, entirely developed in this work for optoelectronics application, is presented and its model derived in details. Finally, the meshing strategy to obtain the network of Generalized Devices describing a given semiconductor structure is reported.

Chapter 3 presents the simulations of various optoelectronic devices using the Generalized Lumped Devices (GLD) approach. First of all, a solar cell in DC operation and a photodiode in transient operation are studied. Then, the model is employed to predict the optically-triggered current amplification in a bipolar phototransistor. Finally, the operation of a pixel of a CMOS image sensor and the crosstalk between adjacent pixels are simulated. In particular, a 3T-Active Pixel Sensor, that includes the photosensing element and a read out circuit made of 3 transistors, is analyzed. The network of GLD describing the photodiode is directly connected to the in-pixel circuit, described with transistor compact models, and the whole pixel is simulated in a single run with a circuit simulator. The model is validated with TCAD Sentaurus numerical simulations. The same geometrical and technological parameters are used for the GLD model and TCAD simulations, hence no fitting or empirical parameter is inserted in the model.

Part II presents the extension of the Generalized Lumped Devices approach to model radiation-induced carriers in ICs substrate and its application for alpha particle strike on silicon substrates.

Chapter 4 provides an introduction on radiation-semiconductor interaction, detailing the mechanisms that can cause circuit dysfunctions at ground level. Radiation effects in ICs are described, with an emphasis on Single Event Effects, which are caused by radiation-induced excess carriers in ICs substrate. After, a literature review on Single Event Effects modeling is presented. Finally, the extension of the Generalized Devices models developed in this work for radiation-induced excess carriers SPICE simulation is reported. A new meshing strategy and high-injection phenomena are discussed, including funneling effect, that occurs when excess carriers with density higher than the doping are generated in proximity of a p-n junction.

Chapter 5 reports simulations of alpha particles impinging on silicon substrates.

The parasitic currents induced on n^+ wells in p-substrate (representing source/drains of n-MOSFETs) are studied as a function of alpha particle energy and position in the substrate. Then, an alpha particle whose track in silicon crosses a p-n junction, triggering a funneling effect, is analyzed. Also in this case, TCAD simulations are employed for validation of the GLD model, using the same geometrical and technological parameters.

Chapter 6 summarizes the conclusions of this work and suggests further extensions that would enable future applications of the Generalized Lumped Devices approach in new fields.

Optoelectronics Part I

2 Modeling of photocarriers in silicon

2.1 Basics of light-semiconductor interaction

A photon that impinges on a semiconductor can be reflected at the surface, absorbed in the bulk if its energy is higher than the semiconductor bandgap energy E_G, or transmitted through the material if its energy is lower than the bandgap. When the photon is absorbed, it excites an electron from the valence band to the conduction band, generating an electron-hole pair in the semiconductor, i.e. a pair of excess carriers. Two types of band-to-band transitions are possible: direct and indirect. If a semiconductor has a direct bandgap, for example GaAs, the top of the valence band and the bottom of the conduction band are characterized by the same crystal momentum (k-vector), as shown in Fig. 2.1, on the right. The interaction is a two-particle process: the photon with energy higher than E_G causes the transition of the electron. Conversely, for indirect bandgap semiconductors the top of the valence band and the bottom of the conduction band are associated to different values of crystal momentum. In this case, two scenarios have to be distinguished. If the photon has an energy higher than the indirect bandgap but lower than the direct bandgap (the minimum difference between valence band and conduction band at the same crystal momentum) the interaction is a three-particle process. Phonons are involved in order to conserve momentum, i.e. to move horizontally, following the red arrow in Fig. 2.1. Phonons, with energy E_P, can be either absorbed or emitted [3]. If the photon energy is higher than the direct bandgap, the interaction happens in the same way as direct bandgap semiconductor.

The optical properties of a semiconductor can be described by the complex refractive index $\bar{n}$:

$$\bar{n} = n_r - i k_e \tag{2.1}$$

The real part n_r defines the velocity of the light traveling in the material, whereas the imaginary part k_e, i.e. the extinction coefficient, defines the absorption coefficient

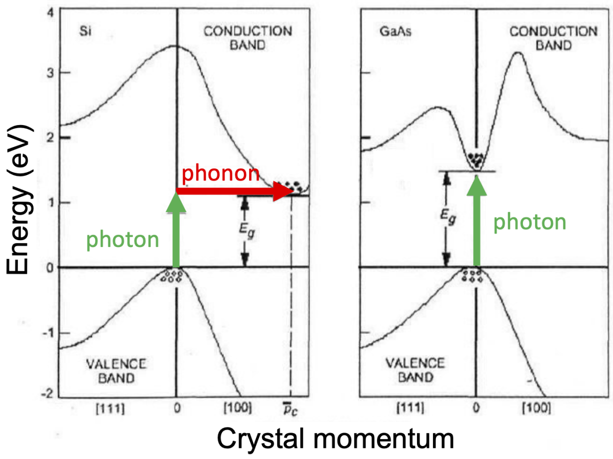

Figure 2.1 – Example of direct bandgap semiconductor, i.e. GaAs (right) and indirect bandgap, i.e. silicon (left).

α [3]:

$$\alpha = \frac{4\pi k_e}{\lambda} \tag{2.2}$$

where λ is the light wavelength. For a direct band-to-band transitions:

$$\alpha = \propto (h\nu - E_G)^{\gamma} \tag{2.3}$$

while for an indirect band-to-band transitions:

$$\alpha = \propto (h\nu - E_G \pm E_P)^{\gamma} \tag{2.4}$$

where $h\nu$ expresses the photon energy and γ is a constant. The absorption coefficient describes the amount of light absorbed by the material. Light intensity I decreases with the distance traveled in the material x according to the equation:

$$\frac{dI(x)}{dx} = -\alpha I(x) \tag{2.5}$$

that gives as a solution

$$I(x) = I_0 e^{-\alpha x} \tag{2.6}$$

where I_0 is the incident light intensity (after reflection at the surface). Eq. 2.6 is the well-known Lambert-Beer law.

The absorption depth is defined as the inverse of the absorption coefficient and represents the point in the material at which the light intensity is equal to 36% of the incident intensity. The absorption coefficient depends on the light wavelength: short wavelengths (high photon energy) have a higher absorption coefficient (shorter

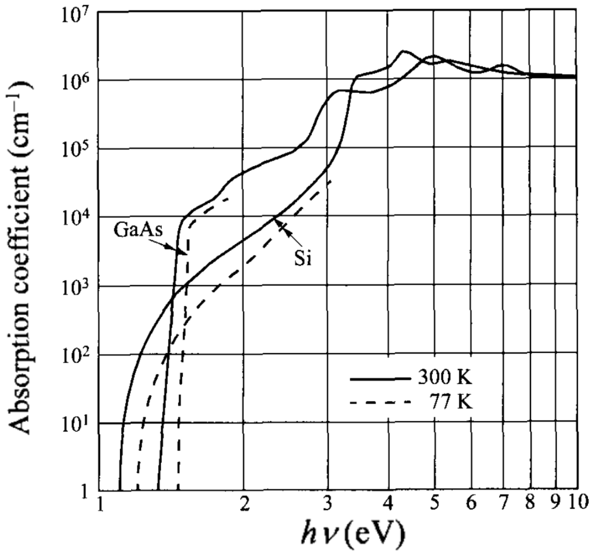

Figure 2.2 – Measured absorption coefficient for Si and GaAs. Adapted from [3].

absorption depth) whereas long wavelengths (lower photon energy) have a lower absorption coefficient (longer absorption depth). Fig. 2.2 shows the absorption coefficients for Si and GaAs, measured experimentally. For a value of 10^4 cm^{-1}, 63% of the light will be absorbed in one micron of semiconductor [3]. In Fig. 2.3 absorption coefficient and depth for visible light in silicon are presented. Data are obtained from measurements at 300K [37].

The spatial distribution of the generation rate G of electron-hole pairs, induced by the incident light, can be extracted from Eq. 2.6. In fact, the generation rate is determined by the loss in light intensity (which results in electron-hole pairs generation). First of all, the photon flux $N(x)$ has to be derived:

$$N(x) = N_0 e^{-\alpha x} = \frac{I_0}{h\nu} e^{-\alpha x} = I_0 \frac{\lambda}{hc} e^{-\alpha x} \tag{2.7}$$

The generation rate $G(x)$ is obtained by differentiating Eq. 2.7:

$$G(x) = \frac{dN(x)}{dx} = \frac{\alpha\lambda}{hc} I_0 e^{-\alpha x} \tag{2.8}$$

Thus, the generation rate follows the exponential decay of the light intensity in the material. It is expressed in cm^{-3}s^{-1}. For a light intensity of 1000 W/m^2 the generation rate[1] at the surface, considering a wavelength of 600 nm (red light), is equal to $1.25{\cdot}10^{21}$ cm^{-3}s^{-1}.

[1]The value 1000 W/m^2 is referred as the peak solar radiation and corresponds to the typical value of the solar irradiance at sea level on a clear day when the sun is at zenith.

Wavelength(nm)	absorption coefficient α (1/cm)	absorption depth (m)
400	9.52E+04	1.05E-05
410	6.74E+04	1.48E-05
420	5.00E+04	2.00E-05
430	3.92E+04	2.55E-05
440	3.11E+04	3.22E-05
450	2.55E+04	3.92E-05
460	2.10E+04	4.76E-05
470	1.72E+04	5.81E-05
480	1.48E+04	6.76E-05
490	1.27E+04	7.87E-05
500	1.11E+04	9.01E-05
510	9.70E+03	1.03E-04
520	8.80E+03	1.14E-04
530	7.85E+03	1.27E-04
540	7.05E+03	1.42E-04
550	6.39E+03	1.56E-04
560	5.78E+03	1.73E-04
570	5.32E+03	1.88E-04
580	4.88E+03	2.05E-04
590	4.49E+03	2.23E-04
600	4.14E+03	2.42E-04
610	3.81E+03	2.62E-04
620	3.52E+03	2.84E-04
630	3.27E+03	3.06E-04
640	3.04E+03	3.29E-04
650	2.81E+03	3.56E-04
660	2.58E+03	3.88E-04
670	2.38E+03	4.20E-04
680	2.21E+03	4.52E-04
690	2.05E+03	4.88E-04
700	1.90E+03	5.26E-04

Figure 2.3 – Absorption coefficient and absorption depth for Si (data measured at 300K).

2.2 State-of-the-art of SPICE simulation of photogenerated carriers and currents

TCAD simulators provides a powerful tool for accurate numerical simulations of excess carriers photogeneration, transport and collection in semiconductor devices. Thus, the resulting photocurrent in a semiconductor device can be correctly predicted. In literature several examples of 3D simulations of photodetectors and other optoelectronic devices can be found, including rigorous analysis of complex architectures and layout [38, 39, 40, 41, 42, 43, 44, 45]. TCAD simulations are particularly useful for prototyping and optimization of novel designs at device level, but are not dedicated to large scale circuit simulations since only few devices can be simulated at a time. In addition, long computation times and not widely available software packages further limit their use in circuit design process. Conversely, SPICE simulations are extensively employed.

SPICE-compatible simulation of photocarriers is based on the analytical or empirical modeling of the photo-induced current. The equivalent circuit model of a photodiode is reported in Fig. 2.4. The photocurrent I_{ph} is described with a current source, which is in parallel with the classical compact model of the diode [46, 47, 48, 49]. Other parameters, such as shunt and series resistances (R_{sh} and R_s) and junction capacitance (C_j) can be added to the model. CMOS pn junction photodiode represents the

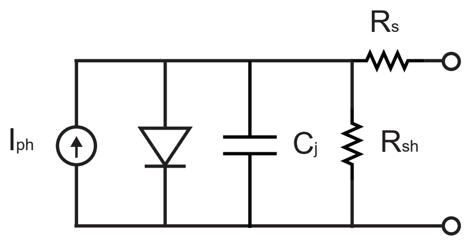

Figure 2.4 – Equivalent circuit model for a photodiode.

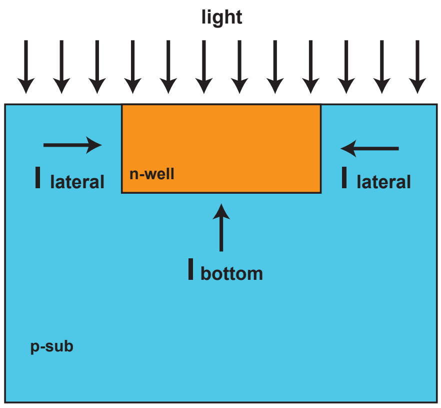

Figure 2.5 – Bottom and lateral collection in CMOS photodiode.

most common photosensing device employed in solid-state image sensors, due to its availability and ease of use [50]. Photocarriers are collected by the bottom and lateral junctions (see Fig. 2.5). Collection through the bottom junction (photocarriers generated deep in the substrate) is the major contribution to the total photocurrent for large devices, whereas lateral collection is an essential component in highly scaled CMOS technologies. Accurate photodiode models need to address both these contributions.

Different semi-analytical approaches have been developed. These are very useful for certain applications, such as compact modeling for circuit simulations [50], but they need extensive fitting with experimental data. In [51, 52, 53], CMOS Active Pixel Sensor[2] (APS) cells were fabricated, using a 0.5-μm CMOS process, and tested. A first semi-analytical expression of the photocurrent including the lateral collection, as a function of the geometrical shape and process data, was derived. Other studies on semi-analytical models for 0.35-μm, 180-nm and 90-nm CMOS technology are presented in [54, 55, 56].

[2]A CMOS APS is an image sensor in which each pixel include a photodiode and a read-out in-pixel circuit.

Several analytical models for photodetectors can be found in literature. Finding an analytical solution is a complex problem. The continuity equation including the optical generation rate has to be solved [50]. Typically, the steady-state continuity equation, assuming zero electric field, is considered:

$$\Delta \hat{u} - \frac{\hat{u}}{\tau D} + \frac{G}{D} = 0 \tag{2.9}$$

where $\hat{u}$ is the excess carrier concentration, τ and D are the lifetime and diffusion coefficient and G is the generation rate (photogenerated electron–hole pairs per unit volume and time). Analytical solutions in 1D do not consider lateral effects [57, 47, 58, 48] and can be used only for devices with large areas. Lateral photocurrent modeling requires at least a 2D solution of the continuity equation. In [59] an array of uniformly spaced stripe collectors are firstly studied. Thanks to the geometrical symmetry, considering a constant optical generation rate and neglecting the variation of the diffusion current in vertical direction, the diffusion equation is reduced to a 1D equation and analytically solved. For the second geometry considered, i.e. hexagonal matrix of small circular collectors, the total photocurrent is expressed using the modified Bessel and Hankel functions. Other studies focus on different geometries (vertical [60, 61, 62], lateral [63], fingered [64], backside illuminated [65], etc.) or on different types of junction (pn, pn$^+$, p-epi-n, n-p$^+$, p-epi-pn$^+$, etc.), photon frequency (visible, ultraviolet, infrared, X-ray, etc.), and other parameters, that require different assumptions [50]. These approaches provide high accuracy and agree well with measured data or numerical simulation, but are very specific to the considered structure. Moreover, they are not easily obtained, introduce several approximations or result in complex expressions that cannot be used for compact models [66]. In [66, 67], a pn$^+$ and a pn CMOS square-shape photodiodes are considered and the continuity equation is solved in 2D. The boundary condition at the surface include the surface recombination effects while the boundary condition at the bottom of the wafer is set by the presence of a metal contact. A 2D analytical solution for the total photocurrent, i.e. bottom and lateral current, is obtained as a function of photodiode size and the surrounding collecting area, that is suitable for compact modeling. It has been coded in Verilog-AMS [68] and employed in CAD environments.

The 2D analytical solution developed in [66, 67] is also used for analytical modeling of electrical crosstalk, as the latter requires an estimation of lateral currents as a function of geometrical features (photodiodes dimensions and spacing). Electrical crosstalk in an image sensor originates when photocarriers generated in an illuminated pixel diffuse towards neighbors pixels, as sketched in Fig. 2.6, producing an unwanted signal in these pixels. Optical crosstalk arises due to reflection, refraction, and scattering of photons at the different internal and external optical interfaces of

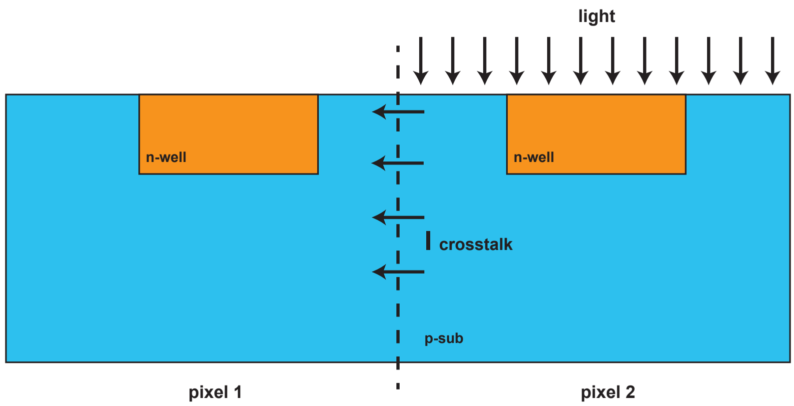

Figure 2.6 – Electrical crosstalk in two adjacent pixels.

the chip (including packaging) [69]. In [70] a closed-form and compact expression for crosstalk as a function of illumination and physical, geometrical, and process parameters is reported. This is among the very few crosstalk models available in literature. Other studies are presented in [53], which proposes a semi-analytical approach approximating the pixel geometrical shape, and in [71], although the lateral diffusion is not considered due to modification in a standard fabrication process, and thus crosstalk effects are probably underestimated [50].

Finally, few examples of 3D modeling are found in literature [72, 73]. The approaches are based on the Fourier series and consider a periodic illumination and a mesa structure. However, the full analytical solution is obtained only for particular conditions, such as semi-infinite substrate and specific elements geometry.

The compact modeling approach presented in Fig. 2.4 is widely employed for the simulation of solar cells in photovoltaic systems. Variations to this circuital equivalent, presented in Fig. 2.7.a, Fig. 2.7.b, and Fig. 2.7.d, are found in literature, but are less popular [4]. In fact, series resistance R_s and parallel resistance R_p affect the I–V characteristics of a solar cell and should be correctly modeled to obtain accurate simulations. In particular, the parallel resistance reduces the available current, whereas the series resistance affects the output voltage [4]. The goal of a solar cell compact model is to predict the IV characteristics, shown in Fig. 2.8, and in particular the three characteristic points: short-circuit point, open-circuit point and maximum power point. These three points allows the optimization of the photovoltaic system according to the specific application. Regarding the 5-parameter model (5-p), in Fig. 2.7.c), several studies are found in literature [74, 75, 76, 77, 78, 79, 80], using different mathematical models, parameter extraction procedures, and major hypotheses and simplifications, demonstrating acceptable levels of accuracy [4]. However, the 5-p model does not consider that the saturation current of the solar cell results from a linear superposition

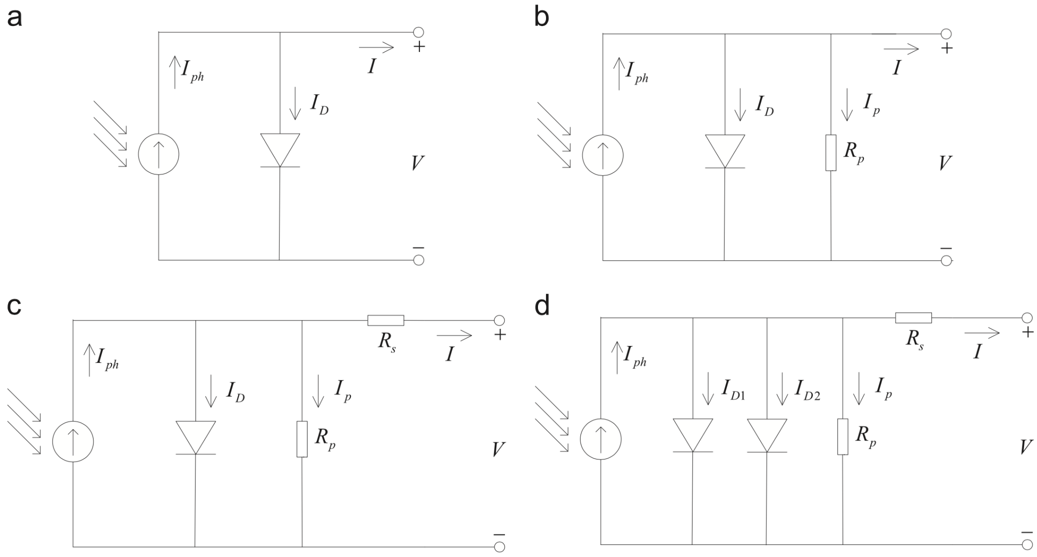

Figure 2.7 – Equivalent circuit models for a solar cell: a. ideal model; b. one-diode only with a parallel resistance R_p (4-p model); c. one-diode with series resistance R_s and parallel resistance R_p (5-p model) and d. two-diode model (7-p model). Model c is the most commonly used. Adapted from [4].

of charge diffusion and recombination in the space-charge region [81]. To correctly model this aspect, the two-diode model, shown in 2.7.d was proposed [81, 82, 83]. The additional diode increases the number of unknown parameters and inserts another exponential term. The model is thus quite complex and requires long computational time. For this reason, and because the benefits in accuracy are important mainly for

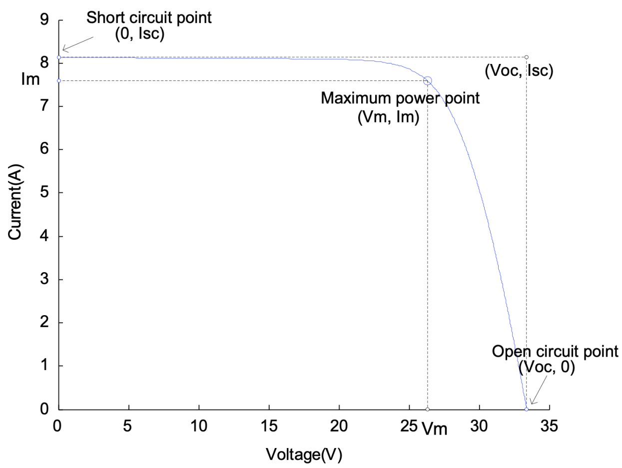

Figure 2.8 – IV characteristics of a solar cell. Adapted from [4].

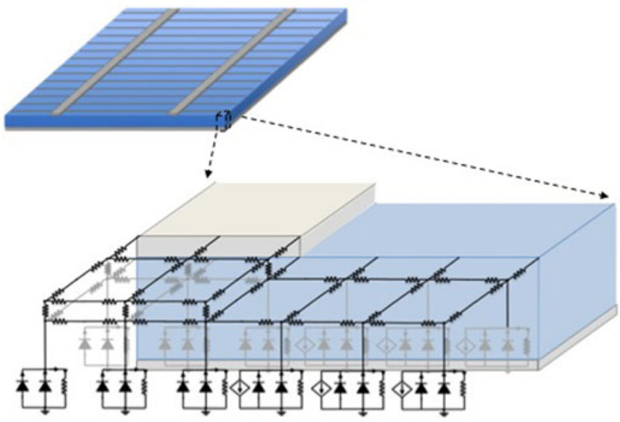

Figure 2.9 – Schematic representation of the distributed electrical network for modeling of solar cell with non uniform distribution of electrical and optical properties. Adapted from [5].

low irradiance level and during partial shading conditions [84], the two-diode model is employed only for specific studies.

Finally, models based on distributed electrical networks are developed for the analysis of lateral inhomogeneities in large area solar cells [85, 86, 87, 5], as shown in Fig. 2.9. These are particularly useful in multicrystalline silicon solar cells, in which the presence of defects causes a non uniform distribution of electrical and optical properties [5]. The solar cell is divided in several small units, described by the equivalent circuit in Fig. 2.7.c or Fig. 2.7.d without R_s, that are interconnected by a resistive network, i.e. distributed series resistance R_s.

2.3 Extended Generalized Lumped Devices approach

SPICE simulation of photogenerated carriers and photocurrents with compact models is quite challenging. Analytical models are very difficult to develop, as a 2D or 3D continuity equation has to be solved. Moreover, analytical solutions require several assumptions and simplifications that depends on the geometry of the device under study. This results in very specific models that are valid only for small sets of devices and technologies. Empirical compact models are often employed but require extensive fitting with experimental data.

To overcome these limits, a novel semi-compact approach for light-induced excess carriers in semiconductors is proposed in this thesis, based on the so-called Generalized Lumped Devices. The latter have been previously developed to model minority carrier parasitic currents in the substrate of HVMOSFET ICs in SPICE environment [6]. In this work, the Generalized Lumped Devices model is extended to include photogeneration of excess carriers in silicon. The modeling approach consists in the description of the semiconductor structure with an equivalent network of Generalized Devices. The structure is firstly meshed (with a much coarser mesh with respect to TCAD numerical simulation, providing very short computation time, around three order of magnitude lower than TCAD), then the equivalent network is obtained by interconnecting the mesh nodes with the proper Generalized Device. The Generalized Resistance models a piece of semiconductor with constant doping, the Generalized Homojunction models the doping discontinuities present at electrical contacts and the Generalized Diode models the pn junctions. In addition, a novel Generalized Device taking into account surface recombination effects has been developed. This equivalent network can predict excess carriers generation, recombination, transport by drift-diffusion and collection. The developed model is SPICE-compatible and physics based. It can simulate photocurrents without any empirical fitting parameter and with no predefined compact model, i.e. independently of the geometry and layout of the device.

2.3.1 Generalized Lumped Devices model including excess carriers generation rate

To model photogenerated excess carrier behavior in a semiconductor structure, for all injection levels, the drift-diffusion problem and the continuity equations should be solved in three dimensions, but an accurate and general closed form solution does not exist. This means that numerical methods have to be used, i.e. the well-known TCAD tools. However, the objective is to have fast simulations that can be run using standard SPICE-like circuit simulators. To obtain this result, the complete mathematical problem describing a semiconductor structure, comprising the Poisson equation and the continuity equations for electrons and holes (in this case with the drift-diffusion as transport equation), is simplified. The reduced set of equations is then discretized following the Finite Difference Method (FDM), which is based on a Cartesian meshing[3] of the domain. The FDM strategy can be applied to an IC layout by simplifying the different geometries [6]. An example of FDM mesh applied to IC substrate is shown in Fig. 2.10.

The first simplification is the assumption that the quasi-neutrality hypothesis always holds. As a consequence, it is not required to solve the continuity equation for electrons and for holes. Only one continuity equation is solved, for just one type of carriers. The second simplification consists in removing the Poisson equation from the system. For regions where the electric field changes rapidly in space, for example PN junction interfaces and MOSFET channel regions, the discretization of the Poisson

[3]The meshing is the division of the entire problem domain in smaller pieces: a mesh of geometrical points is created where the equations are solved

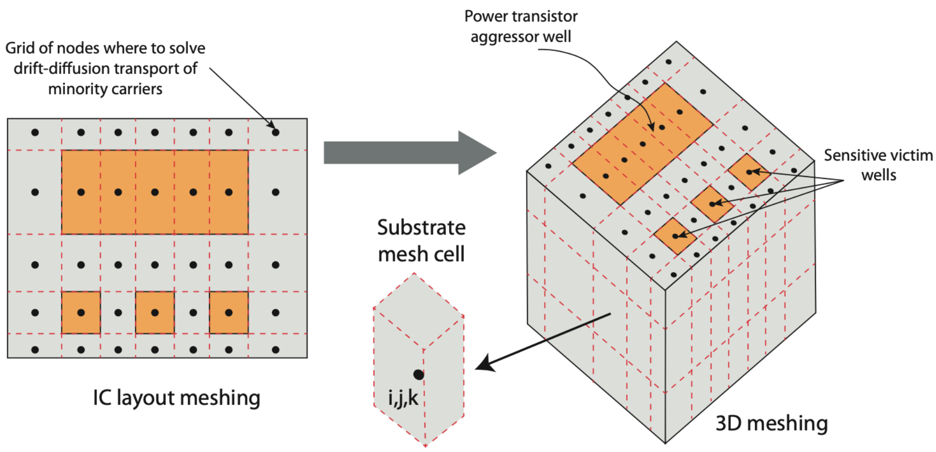

Figure 2.10 – Meshing of an IC substrate using the Finite Difference Method (FDM) (adapted from [6]).

equation would require a mesh size of the order of the Debye length (~ nm), so a very high number of mesh nodes and long computation times. These critical regions are removed from the FDM discretization and are described with compact models, obtaining a semi-compact modeling approach: junctions and transistors are modeled with compact models while the rest of the substrate is modeled with a distributed FDM [6]. In the discretized substrate, the electric field is assumed piece-wise constant (following the quasi-neutrality hypothesis), with a different value in each mesh cell, i.e. still changing over space.

As a result of these simplifications, the FDM is used for the discretization of one continuity equation:

$$\frac{\partial u}{\partial t} = \nabla \cdot \underbrace{(\alpha D \nabla u - \mu u \nabla V)}_{J} + \alpha(G - R) \tag{2.10}$$

where $u(x, y, z)$ is the generic carrier concentration (u is used as generic symbol to indicate equivalently electrons n or holes p), $\alpha = +1$ for electrons and $\alpha = -1$ for holes, D is the diffusion coefficient ($D_n = V_t \mu_n$ and $D_p = V_t \mu_p$, where V_t is the thermal voltage), μ is the mobility, V is the electrostatic potential, R is the recombination rate described with the Shockley-Read-Hall (SRH) model and G is the generation rate. The discretization perfomed in [6] (for HVMOSFET application) was applied to Eq. 2.10 without the generation term G. In this work, the discretization is perfomed again including also the generation rate G. In low injection, considering ambipolar transport, the mobility and lifetime takes the value of the minority carriers. For this reason, in low injection, Eq. 2.10 will refer to the minority carriers. When dealing with optoelectronics application, typically the photogenerated excess carriers concentration is lower than

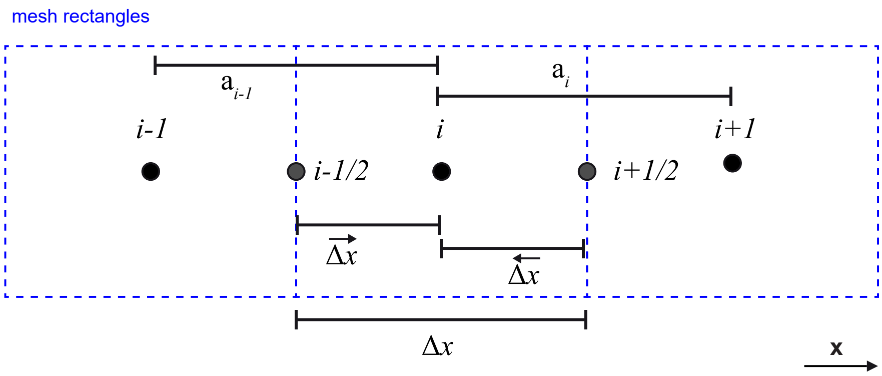

Figure 2.11 – Discretization scheme in 1D, along x-direction.

the doping, i.e low injection. Modeling of high injection condition will be addressed in the second part of this thesis, for high energy particles interaction. Eq. 2.10, in steady-state, can be written in the form:

$$\frac{\partial J_x}{\partial x} + \frac{\partial J_y}{\partial y} + \frac{\partial J_z}{\partial z} = q\alpha(R - G) \tag{2.11}$$

The equation can be split in the three current density components J_x, J_y, J_z in the three directions but the general solution of the problem is not a linear combination of three 1D solutions, as the recombination and generation terms $R(x, y, z)$ and $G(x, y, z)$ are functions of the entire volume. The discretization of Eq. 2.11 is now detailed. For simplicity, the steady-state case will be presented. The discretization is done according to the scheme in Fig. 2.11, where $i-1, i, i+1$ are the mesh nodes, Δx_i is the total mesh size, from $i+1/2$ to $i-1/2$, $\overrightarrow{\Delta x_i}$ and $\overleftarrow{\Delta x_i}$ are used for non uniform mesh elements (mesh node i not centered), and a_i is the distance between two adjacent mesh nodes i and $i+1$. The discretization scheme is shown only for the x-direction, but the same applies also for y and z directions. Eq. 2.10, in steady-state, is linearized as follows:

$$\frac{J_{x_{i+\frac{1}{2},j,k}} - J_{x_{i-\frac{1}{2},j,k}}}{\Delta x} + \frac{J_{y_{i,j+\frac{1}{2},k}} - J_{y_{i,j-\frac{1}{2},k}}}{\Delta y} + \frac{J_{z_{i,j,k+\frac{1}{2}}} - J_{z_{i,j,k-\frac{1}{2}}}}{\Delta z} = q\alpha(R_{i,j,k} - G_{i,j,k}) \tag{2.12}$$

The following linearized quantities are also obtained (for x-direction, the same applies for the other directions):

$$\left.\frac{d\hat{u}}{dx}\right|_{i+\frac{1}{2}} = \frac{\hat{u}_{i+1} - \hat{u}_i}{a_i} \tag{2.13}$$

$$\hat{u}_{i+\frac{1}{2}} = \frac{\hat{u}_i R_g + \hat{u}_{i+1}}{1 + R_g} \tag{2.14}$$

$$R_g = \frac{\overleftarrow{\Delta x_i}}{\overrightarrow{\Delta x_{i+1}}} \tag{2.15}$$

$$E_{i+\frac{1}{2}} = -\frac{V_{i+1} - V_i}{a_i} \tag{2.16}$$

and thus expressions for the linearized current densities J_x, J_y, J_z can be derived. For $J_{x_{i+\frac{1}{2},j,k}}$:

$$J_{x_{i+\frac{1}{2},j,k}} = q\mu_{i+\frac{1}{2},j,k}\hat{u}_{i+\frac{1}{2},j,k}\frac{V_{i,j,k} - V_{i+1,j,k}}{a_i} + \alpha q D_{i+\frac{1}{2},j,k}\frac{\hat{u}_{i+1,j,k} - \hat{u}_{i,j,k}}{a_i} \tag{2.17}$$

Similar expressions are obtained for $J_{x_{i-\frac{1}{2},j,k}}$ and for all the other directions. Substituting the expressions for the linearized current density in Eq. 2.12, the following is obtained:

$$\begin{aligned}
&\left(qD_{i+\frac{1}{2},j,k}\frac{\hat{u}_{i+1,j,k} - \hat{u}_{i,j,k}}{a_i} - qD_{i-\frac{1}{2},j,k}\frac{\hat{u}_{i,j,k} - \hat{u}_{i-1,j,k}}{a_{i-1}}\right)\Delta y\Delta z + \\
&\alpha\left(q\mu_{i+\frac{1}{2},j,k}\hat{u}_{i+\frac{1}{2},j,k}E_{x_{i+\frac{1}{2},j,k}} - q\mu_{i-\frac{1}{2},j,k}\hat{u}_{i-\frac{1}{2},j,k}E_{x_{i-\frac{1}{2},j,k}}\right)\Delta y\Delta z + \\
&\left(qD_{i,j+\frac{1}{2},k}\frac{\hat{u}_{i,j+1,k} - \hat{u}_{i,j,k}}{b_j} - qD_{i,j-\frac{1}{2},k}\frac{\hat{u}_{i,j,k} - \hat{u}_{i,j-1,k}}{b_{j-1}}\right)\Delta x\Delta z + \\
&\alpha\left(q\mu_{i,j+\frac{1}{2},k}\hat{u}_{i,j+\frac{1}{2},k}E_{x_{i,j+\frac{1}{2},k}} - q\mu_{i,j-\frac{1}{2},k}\hat{u}_{i,j-\frac{1}{2},k}E_{x_{i,j-\frac{1}{2},k}}\right)\Delta x\Delta z + \\
&\left(qD_{i,j,k+\frac{1}{2}}\frac{\hat{u}_{i,j,k+1} - \hat{u}_{i,j,k}}{c_k} - qD_{i,j,k-\frac{1}{2}}\frac{\hat{u}_{i,j,k} - \hat{u}_{i,j,k-1}}{c_{k-1}}\right)\Delta x\Delta y + \\
&\alpha\left(q\mu_{i,j,k+\frac{1}{2}}\hat{u}_{i,j,k+\frac{1}{2}}E_{x_{i,j,k+\frac{1}{2}}} - q\mu_{i,j-\frac{1}{2},k}\hat{u}_{i,j,k-\frac{1}{2}}E_{x_{i,j,k-\frac{1}{2}}}\right)\Delta x\Delta y = \\
&\qquad q(R_{i,j,k} - G_{i,j,k})\Delta x\Delta y\Delta z
\end{aligned} \tag{2.18}$$

As state above, Eq. 2.18 is composed of an expression repeated for the three directions x,y,z plus the volumic terms of generation and recombination. A schematic representation of this equation is reported in Fig. 2.12, where the three current density components in the three directions J_x, J_y, J_z and generation and recombination terms are shown for a mesh element. The dimensional parameter $d_m = 3$ is introduced for the discretization of generation and recombination in the three directions. Eq. 2.18 in

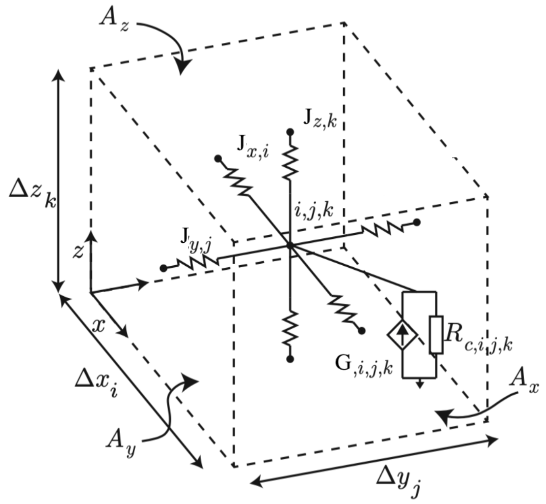

Figure 2.12 – Schematic representation of Eq. 2.18: the three current densities component in the three directions J_x, J_y, J_z and two volumic terms, i.e. generation and recombination

x-direction is:

$$\begin{aligned} qD_{i+\frac{1}{2},j,k}\frac{\hat{u}_{i+1,j,k}-\hat{u}_{i,j,k}}{a_i} - qD_{i-\frac{1}{2},j,k}\frac{\hat{u}_{i,j,k}-\hat{u}_{i-1,j,k}}{a_{i-1}} + \\ \alpha q\mu_{i+\frac{1}{2},j,k}\hat{u}_{i+\frac{1}{2},j,k}E_{x_{i+\frac{1}{2},j,k}} - \alpha q\mu_{i-\frac{1}{2},j,k}\hat{u}_{i-\frac{1}{2},j,k}E_{x_{i-\frac{1}{2},j,k}} = \\ q(R_{i,j,k}-G_{i,j,k})\frac{\Delta x}{d_m} \end{aligned} \tag{2.19}$$

Eq. 2.19 is an algebraic equation that can be solved by SPICE simulators using Kirchhoff laws[4] if all the quantities are expressed as electrical quantities, i.e. voltages and currents. To this purpose, the definitions of equivalent voltages and equivalent currents are introduced. The equivalent voltage is proportional to the excess minority carrier concentration and the equivalent current is proportional to excess minority carrier gradient (the proportionality constant is the elementary charge q, which is added for scaling purposes):

$$V_{eq} = q\hat{u} \tag{2.20}$$

$$I_{eq} = q\frac{d\hat{u}}{dx} \tag{2.21}$$

Eq. 2.19 can be mapped on equivalent voltages and currents. Considering one half of

[4]This is possible because the continuity equation is a conservation law and can be mapped using voltages and currents [6].

the mesh element, the following is obtained:

$$A_x D_{i+\frac{1}{2}} \frac{V_{eq_{i+1}} - V_{eq_i}}{a_i} + A_x \alpha \mu_{i+\frac{1}{2}} \frac{V_{eq_i} R_g + V_{eq_{i+1}}}{1+R_g} E_{x_{i+\frac{1}{2}}} - A_x q R_i \frac{\Delta x}{2d_m} + A_x q G_i \frac{\Delta x}{2d_m} = 0 \tag{2.22}$$

and expressing the recombination term as $R = \hat{u}/\tau$, where τ is the minority carrier lifetime, the expression is:

$$A_x D_{i+\frac{1}{2}} \frac{V_{eq_{i+1}} - V_{eq_i}}{a_i} + A_x \alpha \mu_{i+\frac{1}{2}} \frac{V_{eq_i} R_g + V_{eq_{i+1}}}{1+R_g} E_{x_{i+\frac{1}{2}}} - A_x \frac{V_{eq_i}}{\tau} \frac{\Delta x}{2d_m} + A_x q G_i \frac{\Delta x}{2d_m} = 0 \tag{2.23}$$

An equivalent circuit that describes Eq. 2.23 can be obtained considering Eq. 2.23 a Kirchhoff current law, i.e. there are four current contributions for one node that sum up to zero, and considering that a linear relationship between currents and voltages can be modeled as a resistance. By doing so, the equivalent circuit in Fig. 2.13, that connects the mesh node i to the mesh node $i+1$ (see Fig. 2.11), is derived. This equivalent circuit is the Minority Carrier Circuit (MCC), resulting from the discretization of the continuity equation for the minority carriers. It can simulate generation, recombination, drift and diffusion of excess minority carriers. Since neutrality hypothesis holds, information on both minority and majority excess carriers concentrations and gradients are obtained. The circuit in Fig. 2.13 also reports two capacitances, which are derived from the discretization of the non-stationary equations. These are diffusion capacitances that model the transient phenomena.

The values of the circuital parameters are the following:

$$G_c = \frac{A_x \Delta x}{\tau 2d_m} \tag{2.24}$$

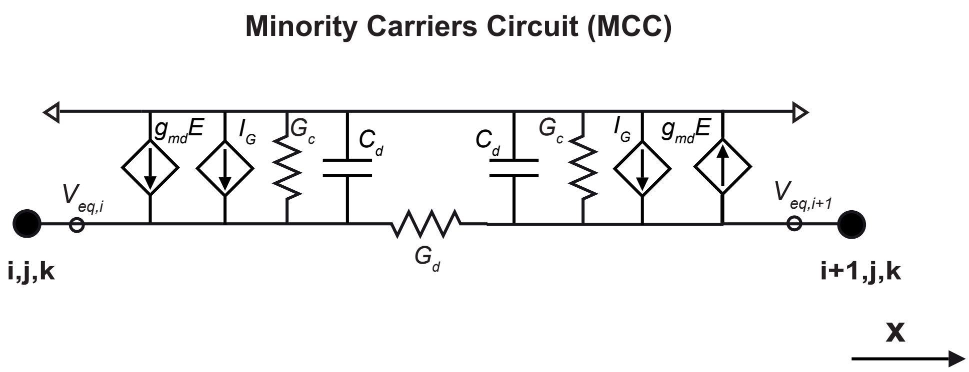

Figure 2.13 – Minority Carrier Circuit (MCC): circuital equivalent of the discretized continuity equation (Eq. 2.10) for the stationary case.

$$G_d = \frac{A_x D_{i+\frac{1}{2}}}{a_i} \tag{2.25}$$

$$g_{md}E = A_x \alpha \mu_{i+\frac{1}{2}} \frac{V_{eq_i} R_g + V_{eq_{i+1}}}{1 + R_g} E_{x_{i+\frac{1}{2}}} \tag{2.26}$$

$$I_G = A_x q G_i \frac{\Delta x}{2 d_m} \tag{2.27}$$

$$C_d = \frac{A_x \Delta x}{d_m} \tag{2.28}$$

Regarding optical generation G_i, the Lamber-Beer law, presented in section 2.1, is used to derive the value of the generation rate, from impinging light intensity, as a function of the depth d in the semiconductor structure:

$$G = \frac{\alpha \lambda}{hc} I_0 e^{-\alpha d} \tag{2.29}$$

The additional term I_G in the MCC is obtained in this work, that was not present in [6].

With the circuit in Fig. 2.13, only minority carrier information, in the form of equivalent voltages and currents, is available. An additional circuit is required for the simulation of *real* voltages and currents in the semiconductor, that depend on majority and minority carriers. The drift-diffusion model is considered for the generic carrier $u(x, y, z)$:

$$J_{i+\frac{1}{2}} = q \left[\mu_M \left(N + \hat{u}_{i+\frac{1}{2}} \right) + \mu_m \left(u_0 + \hat{u}_{i+\frac{1}{2}} \right) \right] E_{i+\frac{1}{2}} + q \left(D_n - D_p \right) \left. \frac{d\hat{u}}{dx} \right|_{i+\frac{1}{2}} \tag{2.30}$$

where μ_M is the majority carrier mobility, μ_m is the minority carrier mobility, N is the doping concentration, u_0 is the thermal equilibrium minority carrier concentration, D_n is the diffusion coefficient for electrons and D_p is the diffusion coefficient for holes. Eq. 2.30 takes into account the bulk conductivity modulation given by both minority and majority carriers and also the correction term taking into account the difference between majority and minority diffusion currents (I_{bulk}) [6]. This expression is thus valid also for high injection. The equivalent circuit describing Eq. 2.30 is the Total Current Circuit (TCC), that models the *real* currents and voltage, and it is reported in Fig. 2.14. The TCC includes a constant resistance G_0, that is the doping-dependent resistance, a varying resistance G_{min} to model the conductivity modulation by excess

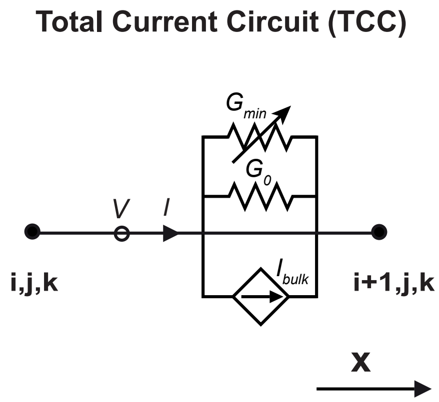

Figure 2.14 – Total Current Circuit (MCC): circuital equivalent of the drift-diffusion equation (Eq. 2.30).

carriers and the correction term I_{bulk}:

$$G_0 + G_{min} = \frac{A_x}{a_i}\left[\mu_M\left(N + \hat{u}_{i+\frac{1}{2}}\right) + \mu_m\left(u_0 + \hat{u}_{i+\frac{1}{2}}\right)\right] \tag{2.31}$$

$$I_{bulk} = A_x q\left(D_n - D_p\right)\left.\frac{d\hat{u}}{dx}\right|_{i+\frac{1}{2}} \tag{2.32}$$

The substrate distributed model is obtained by interconnecting each mesh node (i.e. point i, j, k in the 3D mesh element in Fig. 2.12) and the neighbor mesh nodes in all directions with a *Generalized Device* that represents the discretized equations in one direction. Structures with 2D or 1D dimensionalities, i.e. quantities constant in one or two directions, can be described with a simplified network in 2D or 1D. For the 2D case, for example, nodes in the third dimension are not considered and the total length of the third dimension is included in the area of the Generalized Devices. Moreover, the dimensional parameter is changed to correctly model generation and recombination: $d_m = 2$ for 2D case and $d_m = 1$ for 1D case.

Fig. 2.15 describes how these Generalized Devices are obtained. The TCC and MCC along the x-axis for two mesh elements are reported inside the blue rectangles. These represent the complete model including transient effects. The mesh node i, j, k and the neighbor node $i+1, j, k$ are shown with a black dot. The Generalized Device interconnects the two mesh nodes. Its equivalent circuit, reported inside the red rectangle, consist of *half* of the TCC and MCC of the mesh rectangle i, j, k and *half* of the TCC and MCC of the mesh rectangle $i+1, j, k$. By summing the resistances in series and merging the current sources contributions, the equivalent circuit of the Generalized Resistance is obtained (Fig. 2.16).

The Generalized Resistance, whose equivalent circuit is reported in Fig. 2.16, models pieces of substrate with constant doping (i.e., there is no junction between the two mesh nodes). To recapitulate, The TCC includes a constant resistance (G_0) which represents the resistance of the substrate (doping dependent), a variable resistance (G_{min}) that takes into account the modulation of the conductivity due to the excess carriers, and a current source (I_{bulk}) which is a correction term for the difference between majority and minority diffusion currents. The MCC includes a conductance (G_d) depending on the diffusivity that regulates the diffusion current, a current source ($g_{md}E$) that accounts for the drift current, a conductance (G_c) depending on the electron-hole pairs lifetime (Shockley Read Hall model) that regulates the carriers recombination in the discretized volume, a current source (I_G) that simulates the photogeneration of excess carriers, and diffusion capacitances (C_d).

The values of these circuital elements, presented above, only depend on geometrical and technological parameters of the semiconductor structure, i.e. the model does not need any empirical or fitting parameters. The TCC and MCC subcircuits are coupled together so that any variations in equivalent voltages and currents affect real voltages and real currents, and vice-versa, as shown in Fig. 2.17 (this bi-directional coupling is a key feature of the model).

As stated above, junctions are modeled with compact models. If between two mesh nodes there is a pn junction, the Generalized Diode is used. The equivalent circuit of the Generalized Diode, reported in Fig. 2.18, is obtained by interconnecting the circuit describing the n-type neutral part of the substrate and the circuit describing the p-type neutral part of the substrate (Generalized Resistance models) through current and voltage sources representing the compact model of the space-charge region of

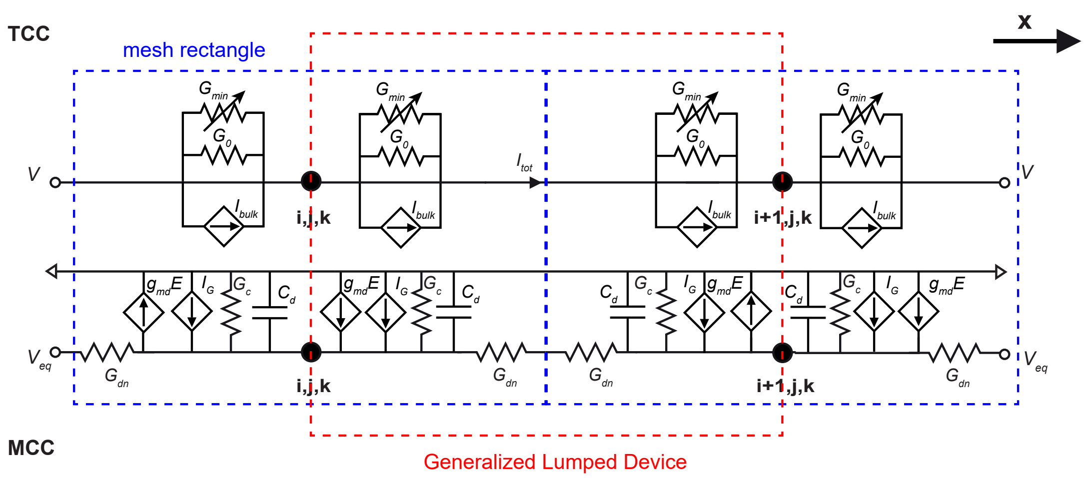

Figure 2.15 – Schematic representation of TCC and MCC in x-direction. The Generalized Device interconnects two adjacent mesh nodes.

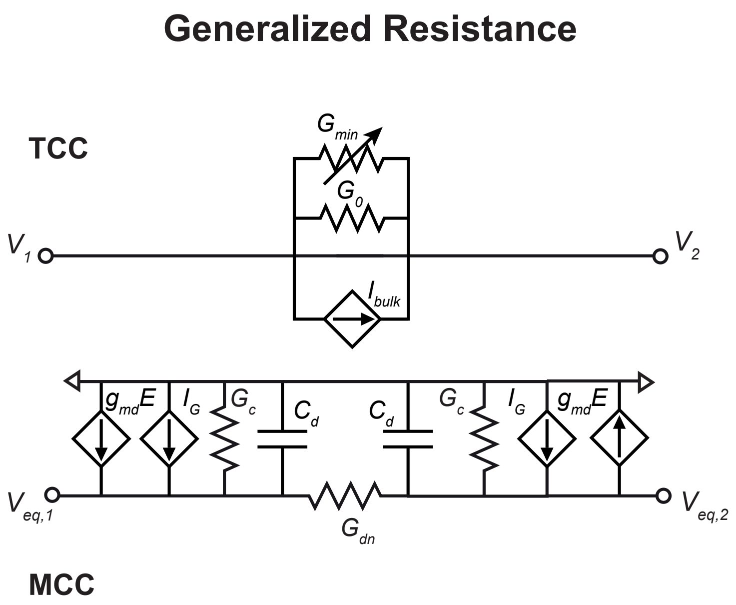

Figure 2.16 – Generalized Resistor equivalent circuit.

the pn junction:

$$V_n = qn_{p_0}\left(e^{\frac{V_j}{V_t}} - 1\right) \qquad V_p = qp_{n_0}\left(e^{\frac{V_j}{V_t}} - 1\right) \tag{2.33}$$

$$I_{tot} = (V_{eq,1} - V_n)G_{dn} + (V_{eq,2} - V_p)G_{dp} + I_{rec} \tag{2.34}$$

where I_{rec} is the current contribution coming from generation-recombination processes in the depletion region, given by the Sah-Noyce-Shockley (SNS) term [6], n_{p_0} is

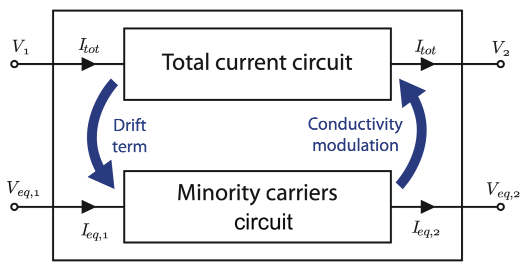

Figure 2.17 – The TCC and MCC are coupled together: variations in equivalent voltages and currents (i.e., excess carriers concentrations and gradients) affect the real voltages and currents, and vice-versa. Adapted from [6].

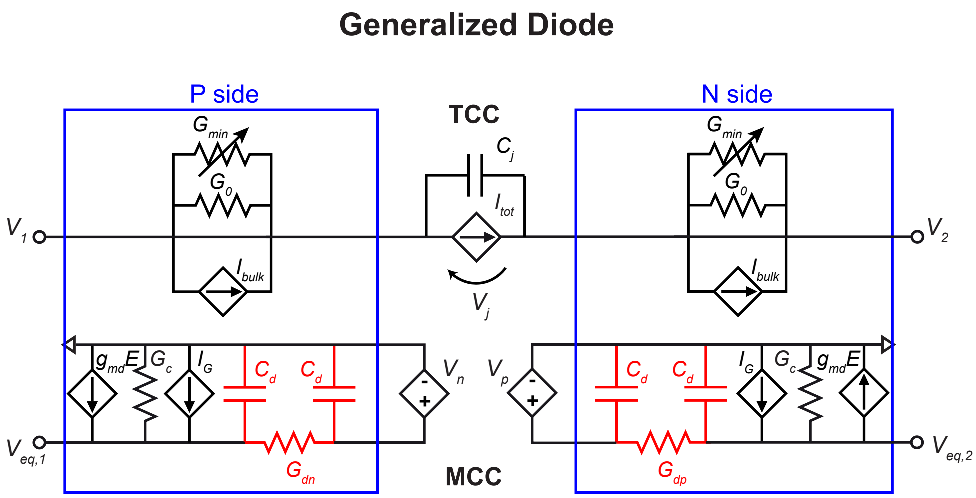

Figure 2.18 – Generalized Diode equivalent circuit.

the electron concentration at thermal equilibrium in the p-side and p_{n_0} is the hole concentration at thermal equilibrium in the n-side. The Π circuit in red is further discretized, obtaining a distributed RC network as shown in Fig. 2.19, to linearize the carriers distribution that rapidly changes at the boundary with the depletion region.

The dimension of the space-charge region x_d and the depletion region widths in the p-type part x_{dp} and in the n-type part x_{dn} are calculated as a function of the applied

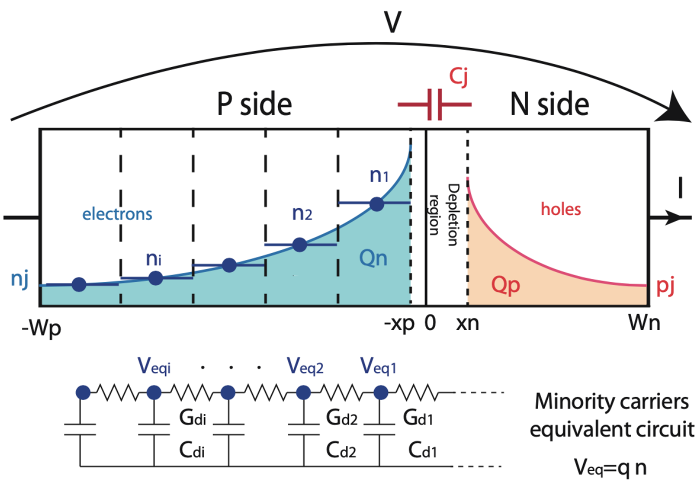

Figure 2.19 – The red part of the Generalized Diode equivalent circuit in Fig. 2.18 is a distributed RC network. This allows for the discretization of the carriers concentration and gradient that vary rapidly near the depletion region. Adapted from [6].

voltage [3]:

$$x_{dn} = \sqrt{\frac{2\epsilon_s}{q} \frac{N_A}{N_D} \frac{1}{N_A + N_D} \left(V_{bi} - V_j\right)} \tag{2.35}$$

$$x_{dp} = \sqrt{\frac{2\epsilon_s}{q} \frac{N_D}{N_A} \frac{1}{N_A + N_D} \left(V_{bi} - V_j\right)} \tag{2.36}$$

where V_{bi} is the built-in potential, N_A and N_D are, respectively, the doping concentrations of the p-type and n-type semiconductors, and ϵ_s is the electric permittivity of silicon. x_{dp} and x_{dn} are then subtracted from the width of the neutral resistive part in the model of the Generalized Diode. This feature of the model, included during this work, will be particularly useful to model the Early effects in phototransistors, that will be presented in the next chapter.

The Generalized Homojunction is used to model the doping discontinuities present at electrical contacts. The equivalent circuit is shown in Fig. 2.20. As for the Generalized Diode, the two neutral regions are modeled using the distributed network (Generalized Resistance equivalent circuit) while the space-charge region of the homojunction is modeled with a compact model.

The substrate model is thus composed of a network of the three Generalized Lumped Devices (GLD) in Fig. 2.21. Since excess carrier concentrations and gradients are represented with electrical quantities (equivalent voltages and currents in the MCC), the network of GLD can be simulated using standard SPICE-like simulators. The circuital equivalences of the models of the Generalized Devices have been coded in Verilog-A, in order to be directly available for simulation with SPICE tools.

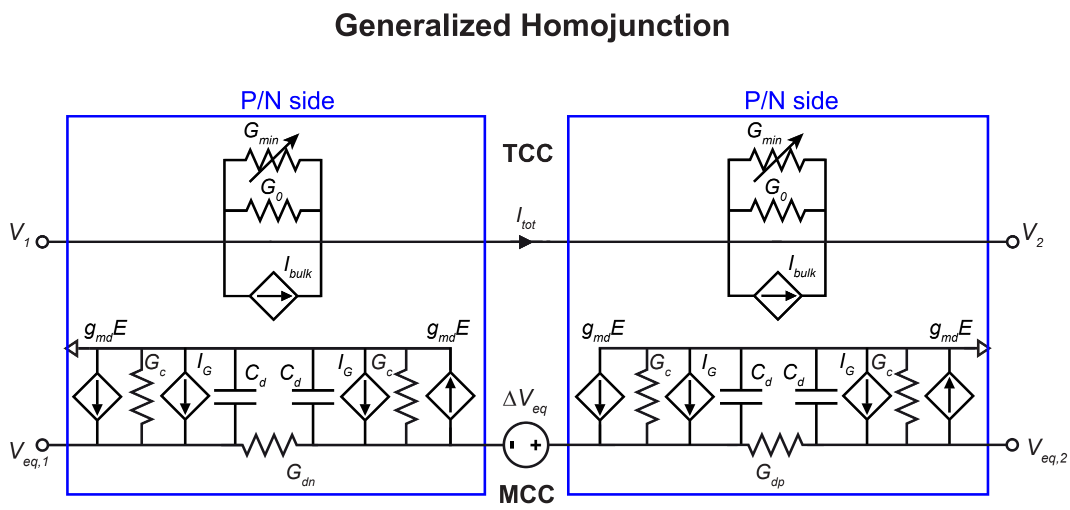

Figure 2.20 – Generalized Homojunction equivalent circuit.

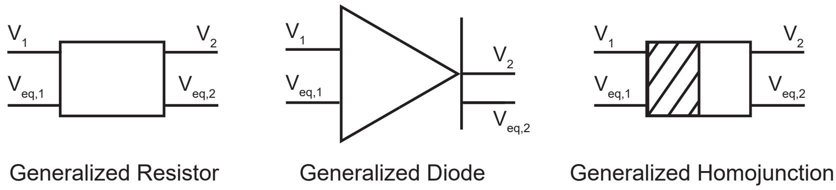

Figure 2.21 – The three Generalized Lumped Devices developed to model minority carrier parasitic currents in HVMOSFET's integrated circuits.

The number of the GLD in the network depends on the mesh of the semiconductor structure, as they interconnect adjacent mesh nodes. Details on the meshing strategy will be provided in section 2.3.3.

2.3.2 Surface recombination effect

For a comprehensive study of optoelectronic devices, surface effects should be taken into account. In fact, since light absorption and photogeneration of free carriers have the peak value at the semiconductor surface, surface recombination can significantly degrade the devices performances [88, 89]. Recombination at the surface is caused by defects or impurities located at the surface of the semiconductor. At the surface, the periodicity of the crystal lattice is interrupted, causing dangling bonds. These are usually reduced by passivating the surface with a layer grown on top of the semiconductor surface. Regarding silicon, passivation is usually done with silicon oxide, that provides the best surface properties, minimizing the defects. Recombination at the surface decreases the concentration of excess carriers, causing a diffusion of the latter toward the surface. A parameter called *surface recombination velocity* is typically used to express the surface recombination and it is specified in cm/s. If the recombination at the surface is zero, the surface recombination velocity is zero, i.e. there is no diffusion of excess carriers toward the surface. Conversely, for an infinitely fast recombination, the diffusion of carriers towards the surface is limited by their maximum possible velocity (about 10^7 cm/s for most semiconductors).

In this thesis, a new Generalized Lumped Device, called Surface Recombination Element, has been developed to include the surface recombination effects (results have been published in [90]). Differently from the Generalized Devices presented in section 2.3.1, the new element consists only in the MCC subcircuit and has a single pin, as shown in Fig 2.22. A single pin is used because carriers that recombine at the surface are lost and do not *propagate* the current further, in contrast to the Ohmic contact for instance.

Surface Recombination Elements are connected to the row of mesh nodes closest

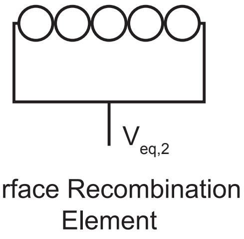

Figure 2.22 – Surface Recombination Element.

to the surface. An example of network of GLD including the Surface Recombination Elements is presented in Fig. 2.23. The generation rate and Shockley-Read-Hall bulk recombination are not included in the model of the Surface Recombination Element, as these are already accounted by the Generalized Devices that interconnects the nodes of the mesh rectangles adjacent to the surface.

The continuity equation to be solved is in the form:

$$\frac{\partial^2 u}{\partial x^2} = 0 \tag{2.37}$$

The electric field is neglected. This assumption is reasonable in this context because out of the semiconductor the electric field is equal to zero, and so also at the surface it is zero, due to the continuity of the electric field. Between the surface and the first mesh node, the electric field is thus negligible. Eq. 2.37 implies that u is linear, and therefore the linearization of the differential equations as required for the Generalized Devices is already satisfied.

In presence of surface recombination, the boundary condition at the surface of the

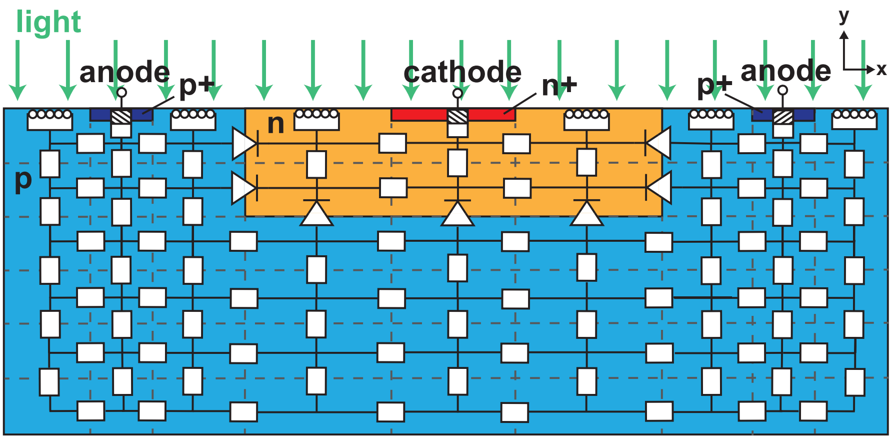

Figure 2.23 – Example of the equivalent network of Generalized Lumped Devices including the Surface Recombination Elements.

semiconductor is given by [3]:

$$qD\frac{\partial u}{\partial x}\bigg|_{x_s} = qS[u(x_s) - u_0] \tag{2.38}$$

where D is the diffusion coefficient, u is the generic carrier concentration (p/n), x_s is the coordinate of the semiconductor surface and S is the surface recombination velocity. Typical values for a bare silicon wafer are in the range of $10^3 - 10^5$ cm/s, depending on the fabrication process, doping type and concentration; values in the range $10^6 - 10^7$ cm/s are the maximum values for surface recombination velocity [91, 92]. Equation (2.38) is one of the two boundary conditions for the continuity equation. The second boundary condition is given by the excess carrier concentration ($\hat{u}_j$) at the j^{th} mesh node connecting the surface recombination element, that is computed by the equivalent network of GLD as the equivalent voltage $V_{eq,j} = q\hat{u}_j$. By solving the continuity equation, a relationship between the equivalent voltage at the j^{th} node and the equivalent current at the j^{th} node is obtained:

$$I_{eq,j} = \underbrace{\frac{ASV_t\mu_m}{LS + V_t\mu_m}}_{G_s} V_{eq,j} \tag{2.39}$$

where V_t is the thermal voltage and μ_m is the mobility of the minority carriers, L is the length of the surface recombination element and represents the distance between the surface and the j^{th} mesh node, and A is the area of the element. The equivalent circuit, reported in Fig. 2.24, is thus a conductance, whose value is G_s, that connects the single pin to the ground. This is consistent since the surface recombination lowers the excess carrier density: part of the equivalent current will flow in G_s, and not in the internal resistances of the MCC of the Generalized Resistor. This will lower the equivalent voltage, i.e. the excess carrier concentration, in the resistor. Note that the model is consistent also for the two limiting cases: $S = 0$ and $S = \infty$. When $S = 0$, the conductance is zero and no current will be subtracted from the equivalent network (more carriers will be *available for collection*), while for $S = \infty$, G_s reaches its

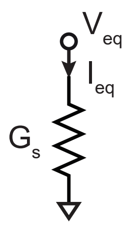

Figure 2.24 – Equivalent circuit of the Surface Recombination Element.

maximum value, i.e. minimum carrier concentration near the surface.

2.3.3 Mesh strategy

A proper meshing strategy is crucial to obtain accurate simulations with low computational time. The mesh dimensions have been optimized to obtain the most accurate results in the shortest time. A set of rules have thus been derived. However, according to the application, mesh size can always be increased to have faster simulation if a lower accuracy is acceptable.

Meshing of the semiconductor substrate to obtain the equivalent network of Generalized Lumped Devices is divided in three steps.

1. Mesh lines are placed at every junctions, pn junctions and homojunctions. A mesh element contains a piece of semiconductor with same doping concentration and type.

2. The mesh is refined so that the maximum size is one fifth of the diffusion length of the minority carriers.

3. In the illuminated region of the semiconductor structure the mesh is further refined. From the surface where the light is impinging down to a distance equal to four times the absorption length α^{-1}, the mesh size is set as one fifth of the absorption length α^{-1}. This value is used to ensure the linearization of the photogeneration profile. For depths higher than this value the photogeneration can be considered negligible, thus the mesh does not need to be refined.

Following these rules, accurate simulation results are obtained, that will be shown in the next chapter, with a computational time about three orders of magnitude lower with respect to TCAD simulations of the same structures.

2.4 Conclusion

A novel approach for SPICE simulation of photogenerated carriers in semiconductor, based on the so-called Generalized Lumped Devices, has been presented. This method is based on the description of the semiconductor structure with an equivalent network of Generalized Devices that can predict excess carriers optical generation, recombination (in the bulk and at the surface), propagation and collection.

The derivation of the Generalized Devices model has been detailed. The model is physics based and SPICE-compatible, i.e. the simulations can be performed using standard circuit simulators. Moreover, it does not need any fitting parameter nor predefined compact model that depends on specific device geometry.

3 Simulation of optoelectronic devices

In this chapter, the Generalized Lumped Devices (GLD) approach, presented in the previous chapter, is employed to simulate the interaction of light with silicon in different optoelectronic devices. The results of simulations performed using the GLD model in SPICE environment (in particular, Spectre circuit simulators) are compared with simulations of the same devices done with a TCAD numerical tool (Sentaurus TCAD). The same silicon intrinsic parameters are used for both TCAD numerical simulations and in the model of the Generalized Lumped Devices, including doping-dependent mobility and lifetime values, bandgap and intrinsic carriers concentration. Hence, no empirical or fitting parameters are introduced in the model.

The objective is to analyse the capability of the model and to understand to what extent it can be used to predict the behavior of optoelectronic devices. The GLD approach was initially developed for a quite different application, i.e. injection of parasitic substrate currents in high voltage MOSFET, but thanks to the extensions and improvements developed during this thesis, it is now an effective tool for the simulation of photogenerated carriers and currents in semiconductor devices. Thus, it is important to assess the accuracy of the model for different conditions and for different devices. However, the goal is not to have a very high accuracy, comparable to TCAD, but to obtain a tool that provides fast and reliable SPICE simulations, to be run in standard circuit simulators, independent on specific compact models and on the layout and applicable to a wide range of devices without extensive fitting.

The results are very interesting. In fact, the model can correctly simulate not only the static and dynamic behavior of a photodetector for a wide range of illumination intensities, but also the full IV characteristics of a solar cells, including the short-circuit current, the open-circuit voltage and the logarithmic dependency between the latter and the illumination intensity. Moreover, the model can predict the optically-triggered switching-on of a bipolar phototransistor and the subsequent current amplification. This particular feature is possible due to the propagation of minority carriers from one Generalized Devices to the other in the network, as analyzed in the previous chapter. Finally, since the model works in the SPICE environment, compact models of any device and transistor can be connected to the network of GLD. Hence, it is possible to co-simulate an optical sensor with the read out circuit within the same SPICE simulation. This crucial characteristics has been exploited to simulate a full CMOS APS image sensor pixel, including both the photodiode and the in-pixel transistors. The model allows also for the evaluation of a key feature of an image sensor, i.e. the electrical crosstalk among neighbor pixels, that is very challenging to obtain with conventional compact models. In conclusion, it is important to underline that the GLD approach can simulate fine details of the drift-diffusion process and can be used to study the physics of excess carriers transport in the semiconductor, as will be shown in the following sections.

This chapter is based on the published papers [93, 94, 90, 95, 96, 97], that present the work done during this thesis about optoelectronic devices simulation.

3.1 Photodiode

The first optoelectronic device studied is a simple photodetector based on a pn junction. Firstly, a 1D structure is analyzed, starting from a simple resistor and then adding the pn junction, to understand how the model simulates the different scenarios. Then, a 2D photodiode is presented. Both the bottom and lateral photocurrents (see Fig. 2.5 in chapter 2) are evaluated. Preliminary simulations to check the correctness of the GLD model for static operation have been performed but are not shown here. The results for transient operation will be directly presented. Static operation will be shown in section 3.2 for the solar cell, i.e. a photodiode with an external resistive load.

3.1.1 1D structures

First of all, a structure with 1D dimensionality, i.e. with all quantities constant in two directions, is studied. Generation, recombination and propagation of carriers upon a pulse of light are simulated in a p-doped ($N_A = 10^{16}$ cm^{-3}) silicon resistor of 20 μm length, 5 μm wide and 1 μm thick. Three different structures have been considered, each of which introduces a different Generalized Device:

- **S1:** Electrodes are in direct contact with the p-type silicon (Ohmic contact conditions are imposed).
- **S2:** Two highly-doped layers ($N_{A+} = 2 \cdot 10^{19}$ cm^{-3}, with a dimension of 0.1 μm) terminate the p-type resistor, constituting two homojunctions. Electrodes contact these highly-doped layers.
- **S3:** An n-type layer is introduced, creating a pn junction (note that two homojunctions are introduced as well, $N_{A+/D+} = 2 \cdot 10^{19}$ cm^{-3}).

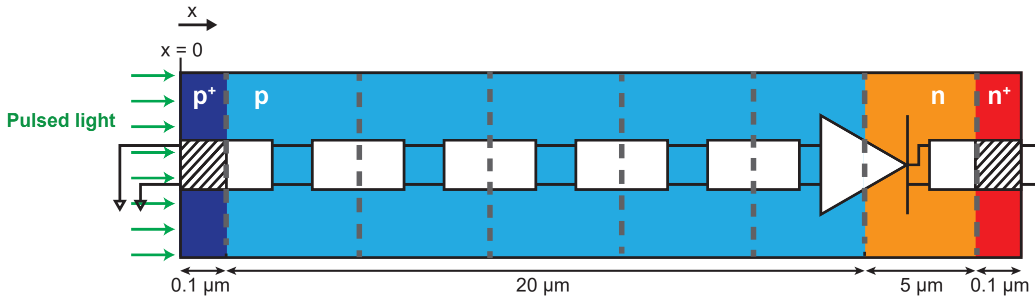

Figure 3.1 – Structure S3: layout, mesh (gray dashed lines) and equivalent network of Generalized Lumped Devices (Generalized Homojunctions, Resistors and Diodes). The structure is uniformly illuminated from the left side, justifying a 1D discretization scheme.

All devices are illuminated uniformly from one side with a 1 ns light pulse of 10^3 W/cm^2 at a wavelength of 600 nm. For silicon, the absorption coefficient at 600 nm is $\alpha = 4.14 \cdot 10^3$ cm^{-1}. A similar type of analysis was used to measure carriers mobility in semiconductors [98, 3] with structures such as S1. The geometry of structure S3 is shown in Fig. 3.1. The other structures are obtained by removing the n-type part and replacing it with a p-type homojunction (S2) or removing the n-type part and the homojunctions (S1). Fig. 3.1 also shows the mesh lines, in gray, and the equivalent network made of Generalized Lumped Devices that connect the mesh nodes. A similar mesh is adopted for S1 and S2. In order to minimize the number of components, still keeping the mismatch with numerical simulations below 2%, eight mesh nodes are placed along the *illuminated zone*, i.e. the region between the illuminated surface and a distance in the semiconductor from this surface of $4\alpha^{-1}$ as explained in section 2.3.3, namely at x = 0.5 μm, 1 μm, 2 μm, 3 μm, 4 μm, 5 μm, 6 μm and 8 μm. As soon as the generation of free carriers becomes negligible ($x > 4\alpha^{-1} \sim 8\mu$m), for this structure, a single Generalized Resistance would be sufficient to account for drift, diffusion and recombination mechanisms in the p-type part. However, in order to extract the excess carrier density with respect to space and time, additional lumped components are intentionally introduced.

The current that flows between the two electrodes is computed using the equivalent network of Generalized Devices, as well as the excess carriers density and gradient as a function of time at the mesh nodes. TCAD simulations are run for each structure, with the same semiconductor parameters used in the Generalized Devices, as explained above. Results of these simulations for the three structures are presented in the following paragraphs.

S1 - uniformly p-type doped resistor

The uniformly p-doped silicon layer is terminated with ideal contacts defined at x = 0 μm and x = 20 μm, i.e. full recombination of excess carriers is imposed at these interfaces. This resistor is biased with a DC voltage of 0.5 V applied on the illuminated side. The densities of electrons (minority carriers) at different coordinates obtained from SPICE using the equivalent network of GLD and TCAD simulations are plotted in Fig. 3.2. Continuous lines represent the results of the GLD model while symbols are for TCAD. The origin of time is set after the pulse of light, i.e., after 1 ns. Fig. 3.2

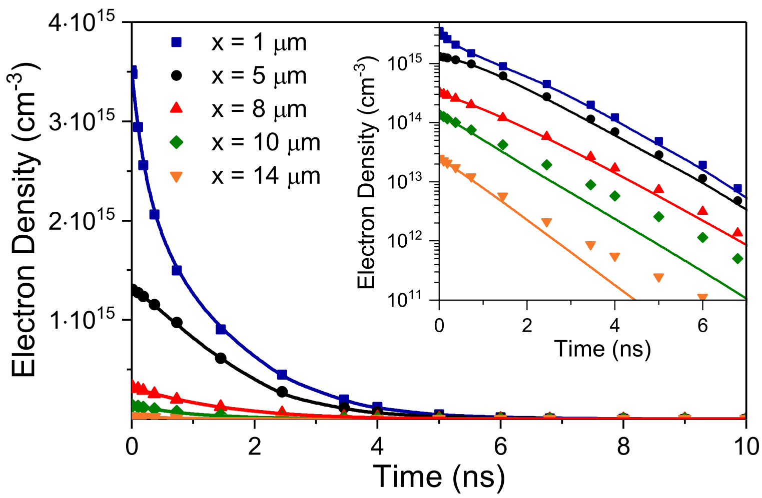

Figure 3.2 – Simulated electron density for the structure S1 (continuous line for GLD model, and symbols for TCAD). The inset shows the electron density in logarithmic scale.

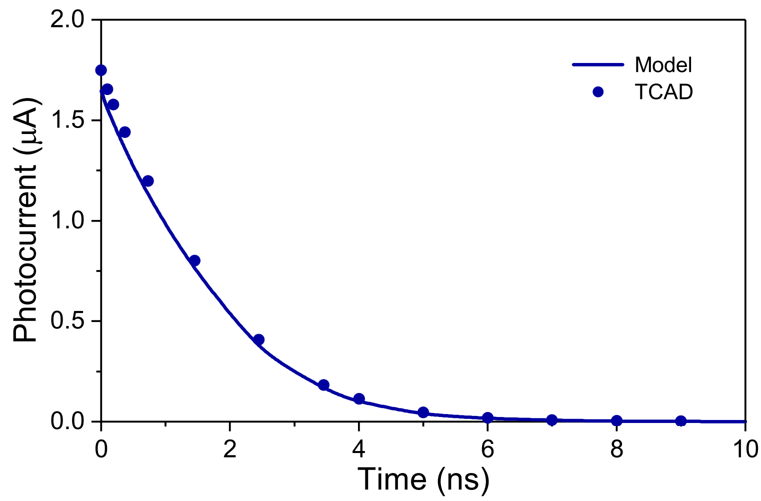

Figure 3.3 – Simulated photocurrent, i.e., total current minus dark current, for the structure S1 (continuous line for GLD model, and symbols for TCAD).

shows that the excess minority carrier concentrations decay about 6 ns after the light pulse, as electrons are accelerated by the electric field and collected rapidly. Beyond 8 μm, the electron density becomes negligible. The GLD model is in good agreement with TCAD numerical simulations. The approach proposed in this thesis can thus correctly predict the time dependence of the minority carrier concentration between the contacts. Concerning the photocurrent (difference between the total current and the dark current) at the output, SPICE simulations are also very accurate, as can be seen in Fig. 3.3. The free carrier density is about one order of magnitude lower than the doping, meaning that it is a low injection condition.

S2 - p-type doped resistor with highly doped homojunctions

In the structure S2, highly p-type doped regions are implemented at x = 0 μm and at x = 20 μm with a negligible extension of 0.1 μm (they are usually inserted to create Ohmic contacts in fabricated structures). The structure is still biased with a DC voltage of 0.5 V applied on the illuminated side. Fig. 3.4 plots the electron density versus time at different coordinates obtained with the Generalized Devices and with numerical TCAD simulations. Again, there is a good agreement between these two approaches. It is worth to note that whereas the pulse of light is the same for S2 and S1, the density of minority carriers is about one order of magnitude higher in S2 compared to S1, i.e., 10^{16} instead of 10^{15} cm^{-3}, and the time scale is in the μs range for S2 instead of some tens of ns, as for S1. Similarly, the transient current decays in the μs range (see Fig. 3.5), which indicates that the drift towards the electrical contact is no longer the dominant mechanism. In fact, the additional homojunction exerts a repelling

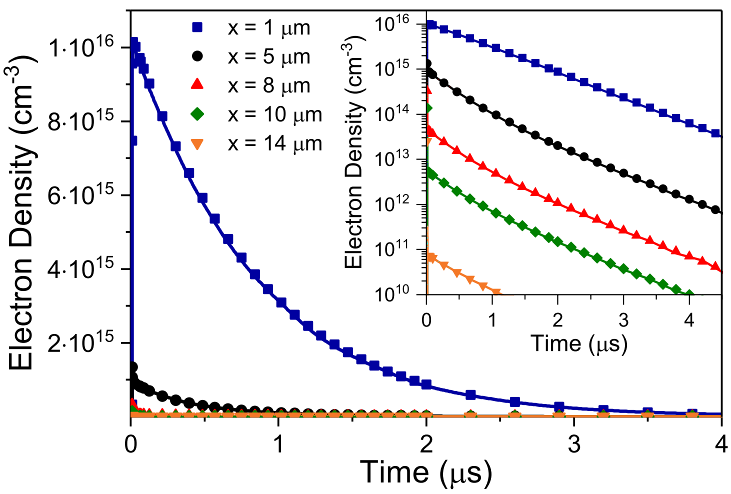

Figure 3.4 – Simulated electron density for the structure S2 (continuous line for GLD model, and symbols for TCAD). The inset shows the electron density in logarithmic scale.

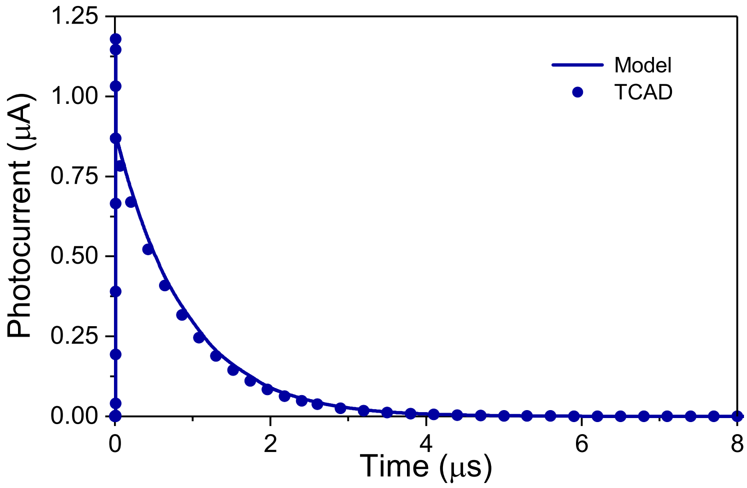

Figure 3.5 – Simulated photocurrent, i.e. total current minus dark current, for the structure S2 (continuous line for GLD model, and symbols for TCAD).

effect on the minority carriers due to the barrier created by the doping gradient. Thus, electrons cannot be collected effectively by the contact and they remain longer inside the silicon. Excess holes could be collected at the counter electrode as they face no barrier, but, since propagation of photogenerated e/h pairs is driven by ambipolar transport, holes move with electrons as a whole. Results of the simulations shows that these fine points are accurately depicted by the equivalent network of GLD, hence the proposed approach can be used also to study the excess carriers transport mechanism from a physics point of view.

S3 - reverse-biased pn junction

The last structure investigated (S3) consists of a diode ($N_{A/D} = 10^{16}$ cm^{-3}) in series with a uniformly p-doped silicon layer, as represented in Fig. 3.1. The p-type layer has a length of 20 μm and the n-type layer has a length of 5 μm. Highly doped p and n regions are also included for Ohmic contacts (both with a length of 0.1 μm). In this case a DC voltage of 0.5 V is applied to the n-doped (non-illuminated) side to set the diode in reverse mode. Again, the electron density at different coordinates is well predicted by the GLD approach, as reported in Fig. 3.6. The transient current is plotted in Fig. 3.7 and, as for the minority carrier concentrations, there is a good correspondence between numerical TCAD simulations and the predictions of SPICE simulations using the GLD model. The overall kinetic for S3 is mid-way between S1 and S2. Since the potential drops almost entirely across the pn junction, the dominant mechanism in this case is diffusion. This is supported by the fact that the photocurrent drops almost to zero after about 150 ns, i.e. the typical time needed for electrons to diffuse from the surface to the pn junction at x = 20 μm. The excess electron density simulated at coordinates where there is no light generation (x ≥ 8 μm) is initially negligible (t = 0), then it shows a maximum after some tens of ns (this value increases when moving further from the surface). This behavior is consistent with a diffusion process where the cloud of carriers photogenerated at the surface at time zero moves towards the pn junction with time. Again, the GLD modeling approach captures these processes accurately. It is interesting to increase the intensity of light from 10^3 W/cm^2 to 10^4 W/cm^2 to investigate high injection regime. Simulations confirm that for

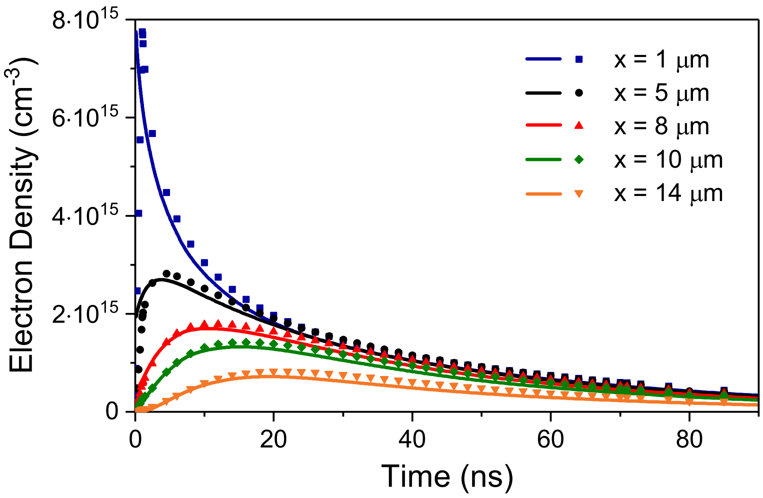

Figure 3.6 – Simulated electron density for the structure S3 (continuous line for GLD model, and symbols for TCAD).

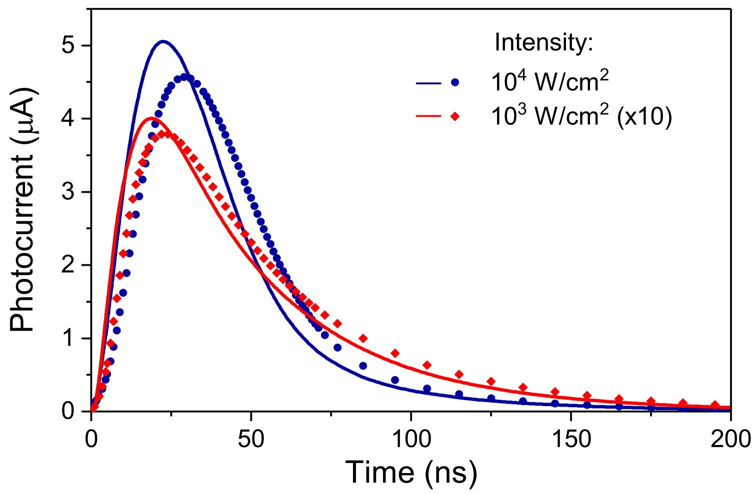

Figure 3.7 – Simulated photocurrent collected by the reverse-biased diode in S3 for two light pulse power densities (continuous line for model and symbols for TCAD). In the 10^3 W/cm^2 case, the photocurrent values have been multiplied by a factor of 10.

10^4 W/cm^2 the density of the photogenerated carriers is higher than the doping concentration (the electron density reaches $\sim 10^{17}$ cm^{-3} at the left homojunction interface).

Fig. 3.7 shows the photocurrent for low (10^3 W/cm^2) and high (10^4 W/cm^2) injection conditions for S3. The effect of high injection degrades slightly the matching with TCAD, but the agreement is still acceptable. The GLD model is also accurate in high injection for the structure S1, while for S2 it is less precise, as the relative error is about 15%. In fact, the model can cope with high injection for cases S1 and S3 because the excess carrier concentration goes back to steady state in quite a short time, while for case S2 the concentration remains larger than the doping concentration for a longer time, leading to bigger errors.

3.1.2 2D structures

The analysis carried out in 1D structures is now generalized to simulate photoelectric effects in a 2D photodiode, represented in Fig. 3.8, where the different doping regions are highlighted. Fig. 3.8 also reports a simplified sketch of the mesh and the equivalent Generalized Devices network derived from the mesh. The actual mesh follows the meshing strategy illustrated in section 2.3.3, hence the mesh is finer near the surface to correctly linearize the exponential photogeneration profile. In particular, the mesh size is set to 0.5 μm in the y direction where photogeneration takes place. The diode consists of an n-type region (40 μm wide and 10 μm thick; the third dimension, where all the quantities are constant, is 1 μm long) with a doping concentration of $2 \cdot 10^{16}$ cm^{-3} surrounded by a p-type region (100 μm wide, 20 μm thick, the third

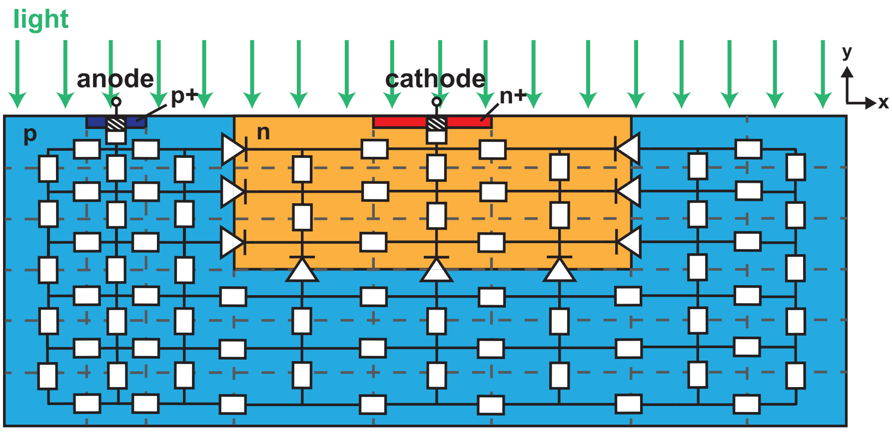

Figure 3.8 – Sketch of the layout of the diode structure used for 2D simulations. The gray dashed lines symbolize the mesh. The equivalent network of the Generalized Lumped Devices is superimposed. The structure is illuminated from the top and the light intensity is constant along the x-axis.

dimension as before) with a doping concentration of $4 \cdot 10^{16}$ cm^{-3}, both contacted with highly doped regions (doping of $2 \cdot 10^{19}$ cm^{-3}, 5 μm wide, 0.25 μm thick). The structure is illuminated from the top with a wavelength of 600 nm and the intensity is assumed constant along the x-axis. As already explained above, same geometrical, technological and physical parameters are used for TCAD simulations and GLD model.

1-pulse illumination

The structure reported in Fig. 3.8 is illuminated with a single pulse of light of 1 ns with an intensity of 10 W/cm^2. The photocurrent collected by the diode biased in reverse mode is plotted as a function of time in Fig. 3.9. As for the 1D case, the results obtained with the equivalent network (continuous line) fit well the data obtained with TCAD numerical simulation (symbols). The model correctly simulates both the quick rising of the photocurrent during the light pulse and the decreasing phase after the pulse, before vanishing around 200 ns. The time response of a photodiode can thus be predicted with standard circuit simulators, with much lower simulation times than with TCAD numerical tool.

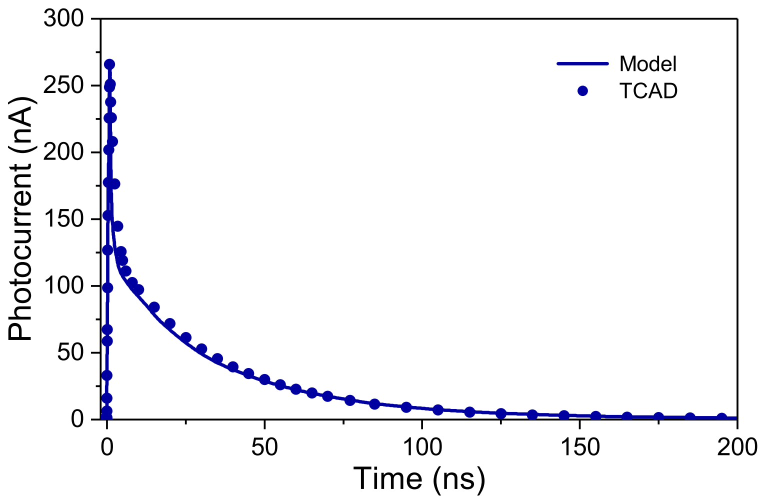

Figure 3.9 – Photocurrent collected by the 2D diode in reverse mode when illuminated with a single pulse of light (continuous line for model and symbols for TCAD).

Periodic excitation

The same structure sets in reverse bias is also illuminated with periodic pulses of 1 ns duration every 10 ns, with light intensity of 10 W/cm^2. The simulations performed using the GLD model and TCAD tool are reported in Fig. 3.10. Even for this mode of operation, the model predicts accurately the time dependence of the photocurrent. Both the transient waveform at early times as well as the successive stabilization are

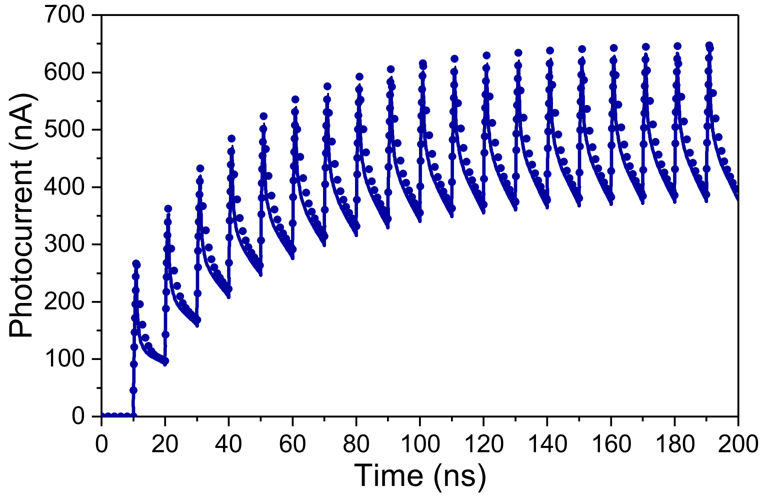

Figure 3.10 – Photocurrent collected by the 2D diode in reverse mode when illuminated with periodic pulses (continuous line for model and symbols for TCAD).

well tracked. In particular, the model simulates the evolution of the charge density and related current inside the structure without degrading the accuracy, i.e., without accumulating errors. For instance, the variation in photocurrent between each pulse is always well estimated (i.e., around 260 nA). Therefore, the sensitivity and the bandwidth of photodetectors can be computed relying on this equivalent network. The optimization of the layout to target some characteristics can be performed using circuit simulators without the need to build a compact model of the photoelectric element, a key feature to optimize the sensor and its control/sensing circuitry before any fine tuning.

3.2 Solar cell

By connecting an external resistive load to a photodiode, a simple solar cell is obtained. This section section will analyze to what extent the GLD model can be used to predict the I-V characteristics of a pn junction solar cell. The structure under test is a 2D structure and is shown in Fig. 3.11. It consists of a 3 μm deep n-well and in a 20 μm deep and 100 μm wide p-type substrate (the length of the third dimension, where all quantities are constant, is set to 1 μm). The 30 μm wide n-well is doped at 10^{16} cm^{-3}, as for the p-type substrate doping. The two zones are contacted with heavily doped regions (10^{19} cm^{-3}). Fig. 3.11 also illustrates an explicative scheme of the mesh rectangles (gray dotted lines) and of the equivalent Generalized Lumped Devices network. The mesh strategy is the same as for the photodiode in section 3.1.2. In this case, the illumination is constant (DC operation), with a wavelength of 600 nm. The value of the external resistance R_L is ramped gradually to rebuild the complete I-V

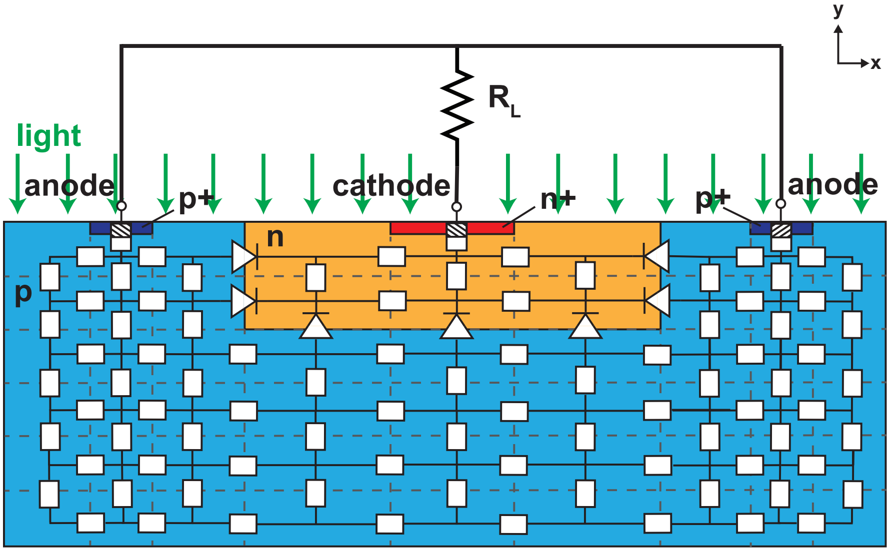

Figure 3.11 – Sketch of the layout of the solar cell structure, with the external load between anode and cathode. The gray dashed lines symbolize the mesh. The equivalent network of the Generalized Lumped Devices is superimposed. The structure is illuminated from the top, and the light intensity is constant along the x-axis.

characteristic of a solar cell, from short-circuit current to open-circuit voltage.

Fig. 3.12 and Fig. 3.13 reports the results obtained with the Generalized Devices equivalent network and TCAD simulations, for different light intensities. A power density of 0.1 W/cm^2 corresponds to the typical value of the sun intensity at sea level at zenith. This intensity is usually employed to characterize solar cells performances.

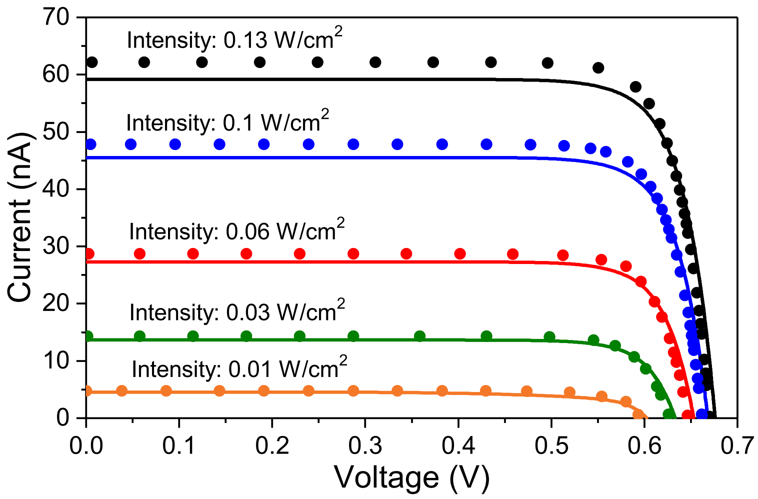

Figure 3.12 – I-V characteristics of the solar cell in Fig. 3.11 for different light intensities (continuous line for GLD model, and symbols for TCAD).

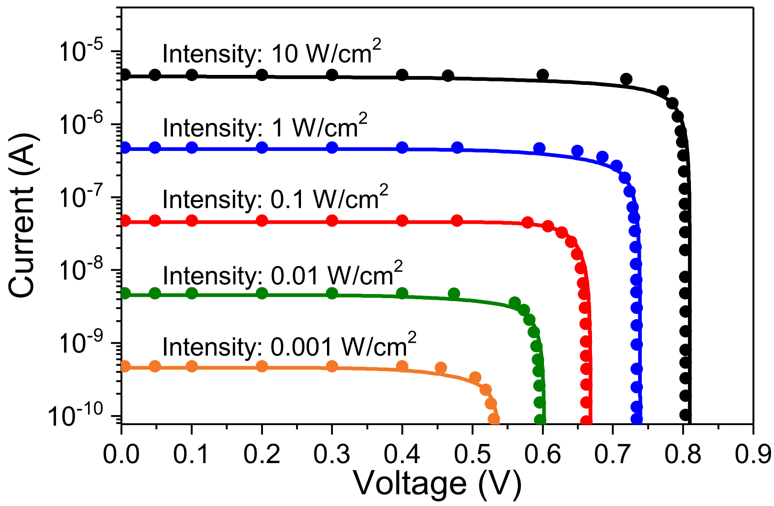

Figure 3.13 – I-V characteristics of the solar cell in Fig. 3.11 for different light intensities. The intensity is ranged over several orders of magnitude (continuous line for GLD model, and symbols for TCAD).

The simulations done with the GLD network (continuous line) are in good agreement with TCAD simulations (symbols) for all intensities of light. It is important to note that the whole characteristic, including the open-circuit voltage and the short-circuit current, is well estimated. The open-circuit voltage is predicted with less than 1% error with respect to TCAD, while the error in predicting the short-circuit current is a bit larger, but still less than 5% (~ 4.8%). Those values are quite accurate given that no fitting parameter is introduced.

The GLD model can also predicts the logarithmic dependency between the open-circuit voltage and the incoming light intensity. The latter is not a trivial result and it was not expected to be predicted so accurately, as the model was developed with a focus on the photocurrent. This feature of the model arises from the intimate coupling between the TCC and MCC subcircuits in Generalized Lumped Devices. Going back to the model of the Generalized Diode, it is possible to understand why the open-circuit voltage is so well estimated. The total current flowing in the diode is set by the current source I_{tot} in the TCC, as explained in section 2.3.1:

$$I_{tot} = (V_{eq,1} - V_n)G_{dn} + (V_{eq,2} - V_p)G_{dp} + I_{rec} \tag{3.1}$$

where V_n and V_p represents the boundary condition at the space-charge region:

$$V_n = q n_{p0} \left(e^{\dfrac{V_j}{V_t}} - 1 \right) \tag{3.2}$$

$$V_p = q p_{n0} \left(e^{\frac{V_j}{V_t}} - 1 \right) \tag{3.3}$$

These three dependent sources couple the MCC and the TCC: the voltage drop across the diode V_j, the excess carrier concentrations and gradients are all interrelated, thanks to Eq. 3.2, Eq. 3.3 and Eq. 3.1. If there is no generation and a voltage is applied externally to the diode, V_n and V_p are imposed by Eq. 3.2 and Eq. 3.3 while the current is given by Eq. 3.1 in terms of V_n and V_p and the resistances of the equivalent network that set $V_{eq,1}$ and $V_{eq,2}$ (the diode is connected to generalized resistors in the network). When the diode is illuminated, the values of $V_{eq,1}$ and $V_{eq,2}$ result from the steady-state condition involving generation and recombination of excess carriers (which depend on the whole network of Generalized Devices, that simulates excess carriers thanks to the MCC). The open-circuit voltage of a solar cell roots in the equivalent voltages $V_{eq,1}$ and $V_{eq,2}$. More precisely, in open-circuit condition, the total current I_{tot} is zero and, according to Eq. 3.1, neglecting I_{rec}, also the currents flowing in the resistances G_{dn} and G_{dp} are equal to zero, since these diffusion currents must have the same sign. It implies that V_n and V_p are necessarily equal to $V_{eq,1}$ and $V_{eq,2}$. Thus, Eq. 3.2 and Eq. 3.3 link directly $V_{eq,1}$ and $V_{eq,2}$ with the voltage drop on the diode, V_j (the simulator will search for the solution that satisfies all the relations). As expected, a logarithmic relationship between the open-circuit voltage (V_j in this case) and the excess carrier density (proportional to $V_{eq,1}$ and $V_{eq,2}$) is found. Conversely, in short-circuit conditions, the applied voltage is zero and thus V_n and V_p reach their minimal values. Since $V_{eq,1}$ and $V_{eq,2}$ are fixed by the rest of the circuit, I_{tot} is maximum, as confirmed in Fig. 3.12 and Fig. 3.13. In between, the equivalent network of Generalized Devices can model the intermediate regime quite precisely.

Hence, the Generalized Devices approach can depict the physics of a solar cell accurately and can be used to study this type of optoelectronic devices also at physics level. Moreover, since the full I-V characteristic of a solar cell can be simulated, the maximum output power can be estimated only from the device geometry and illumination intensity and without the need of an analytical model for the photocurrent in the specific device.

3.2.1 Study of surface recombination effects

The effect of surface recombination can also be included in the model, thanks to the novel Generalized Devices, i.e. the Surface Recombination Element, presented in section 2.3.2. The solar cell performance degradation due to surface recombination are now studied with the Generalized Devices approach and the results are validated

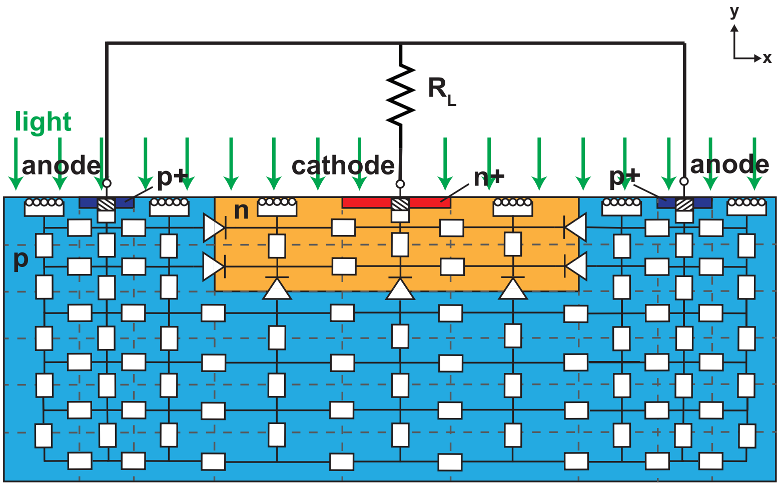

Figure 3.14 – Generalized Lumped Devices equivalent network for the solar cell including Surface Recombination Elements.

with TCAD simulations. Typical values of the surface recombination velocities for a bare silicon wafer are in the range of $10^3 - 10^5$ cm/s, depending on the fabrication process, doping type and concentration, whereas values in the range $10^6 - 10^7$ cm/s are the maximum values for surface recombination velocity [91, 92]. The new equivalent circuit for the solar cell in Fig. 3.11 including the new Generalized Device is reported in Fig. 3.14.

The structure is illuminated from the top at a wavelength of 600 nm (red) with uniform intensity along x of 0.1 W/cm^2 at the surface and constant in time. The surface recombination is assumed to be effective at the illuminated (top) surface only. IV characteristics of the diode under illumination, with a variable resistive load interconnecting the anode with the cathode to simulate the solar cell behavior, are presented in Fig. 3.15 for different surface recombination velocities. The results obtained with the GLD model (lines) are in good agreement with TCAD simulations (symbols). Also in this case no fitting parameter is used in the model and the same surface recombination velocity values are employed for both Generalized Devices and TCAD simulations. Again, the open-circuit voltage (V_{OC}) is better estimated with respect to the short-circuit current (I_{SC}): the error on the value of the open-circuit voltage calculated with the model with respect to the one simulated with TCAD is about 1% when the surface recombination is negligible, and is close to 2% for higher surface recombination velocities. Regarding the short-circuit current, the error is ~ 6% for zero surface recombination velocity and ~ 9% otherwise. For surface recombination velocities higher than 10^6 cm/s no further variation in the IV characteristics is evidenced (not shown here). A surface recombination velocity of 10^3 cm/s provides the same photocurrent as a *zero* surface recombination velocity (i.e.

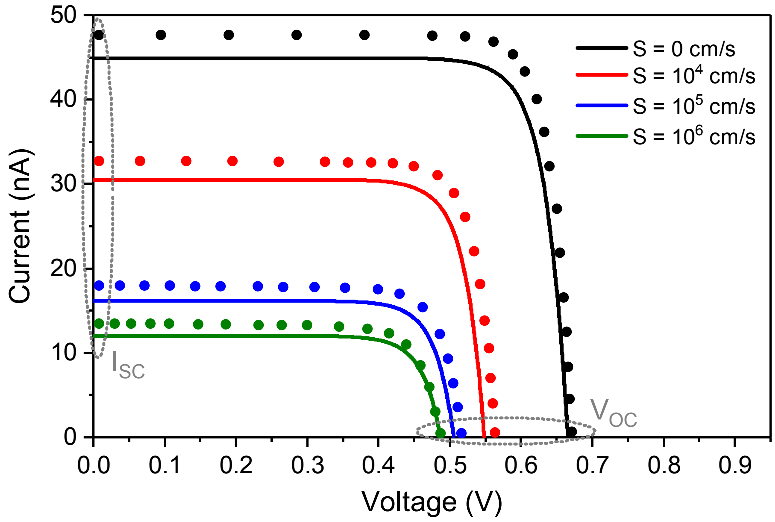

Figure 3.15 – IV characteristics of the structure in Fig. 3.14 for different surface recombination velocity values. Results obtained with the GLD equivalent network are plotted in lines and TCAD results are plotted with symbols.

ideal surface with no recombination).

Fig 3.16 shows how the presence of a surface recombination velocity is not equivalent to a mere lowering of the light intensity. Light intensity is intentionally tuned (i.e. 0.029 W/cm^2) so that the short-circuit current without surface recombination is almost equal to the current with surface recombination of 10^6 cm/s at 0.1 W/cm^2. It happens that recombination taking place at the surface cannot be modeled as a

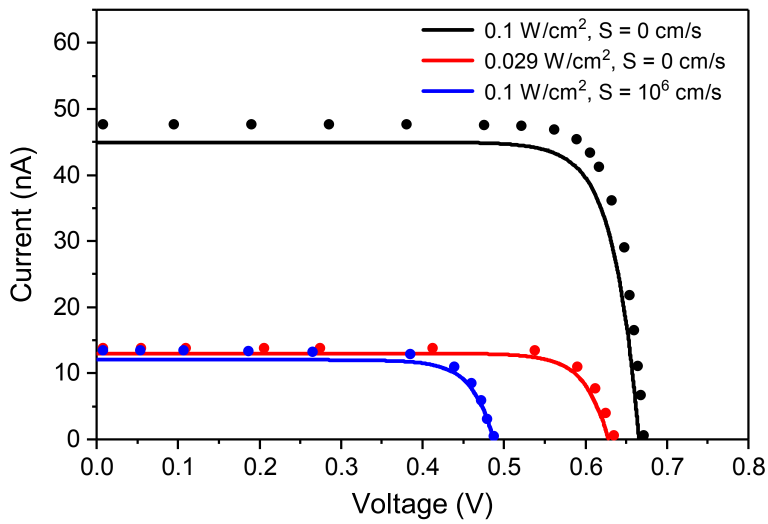

Figure 3.16 – IV characteristics of the structure in Fig. 3.14 for different light intensities and surface recombination values. Results obtained with the GLD equivalent network are plotted in lines and TCAD results are plotted with symbols.

global reduction of photogenerated carriers. In fact, when the structure without surface recombination is illuminated with a lower intensity, the short-circuit current is affected the most, while the open-circuit voltage is only slightly changed. The effect of the surface recombination, instead, is a significant decrease of both the short-circuit current and open-circuit voltage. The model tracks also these effects quite accurately.

So far, simulations have been carried out using a bulk lifetime of 30 μs for electrons and 10 μs for holes. However, there is a kind of *competition* between recombination taking place at the surface and in the volume of the semiconductor. An analysis of the surface recombination effects in structures with different bulk lifetimes is needed. The short-circuit photocurrent is plotted in Fig. 3.17 versus the surface recombination velocity, for different electron and hole lifetimes. Again, the results obtained with the GLD model are in good agreement with the TCAD numerical simulations. For the highest bulk lifetime (30 μs for electrons and 10 μs for holes), the surface recombination is the main contribution to the recombination (the diffusion length is about 300 μm for the electrons and about 100 μm for the holes) and thus the decrease in the photocurrent with surface recombination velocity is pronounced. For lower values of lifetimes, recombination in the substrate is dominant, meaning that the variation of the photocurrent with the surface recombination velocity is weaker. Finally, for very short bulk lifetimes, i.e. 3 ns for electrons and 1 ns for holes, an almost flat characteristic is evidenced.

The quantum efficiency, defined as the ratio between the number of charge carriers collected by the diode and the number of absorbed photons, is now extracted as a

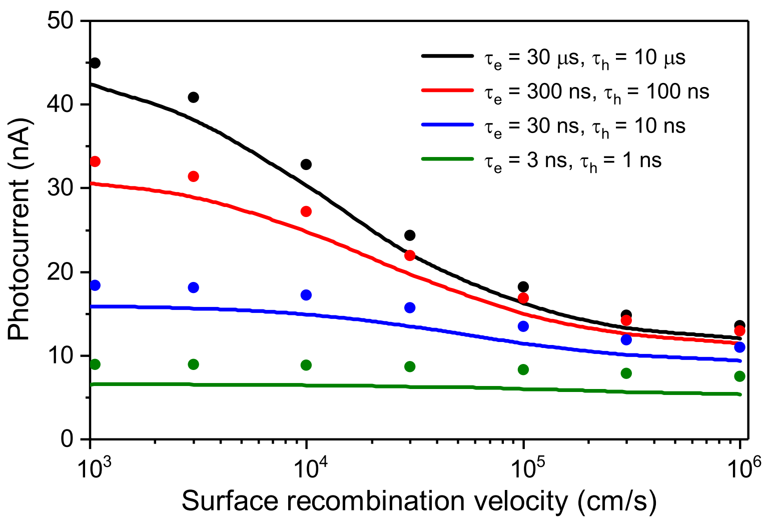

Figure 3.17 – Short-circuit photocurrent as a function of the surface recombination velocity for different electron (τ_e) and hole (τ_h) bulk lifetime. Results obtained with the GLD equivalent network are plotted in lines and TCAD results are plotted with symbols.

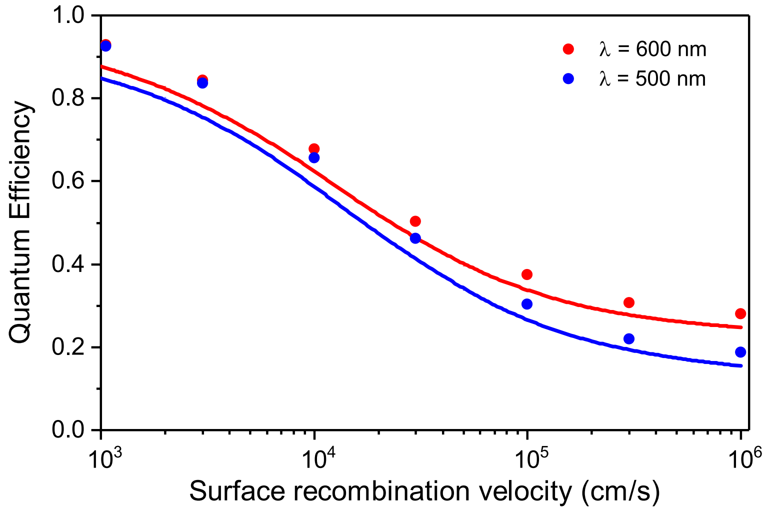

Figure 3.18 – Quantum efficiency as a function of the surface recombination velocity for blue (500 nm) and red (600 nm) light. Results obtained with the GLD equivalent network are plotted in lines and TCAD results are plotted with symbols.

function of the surface recombination velocity. Two wavelengths are studied, 500 nm (blue) and 600 nm (red). As expected, the model predicts that the quantum efficiency decreases for increasing surface recombination velocity. In addition, while for a very low surface recombination velocity the quantum efficiency for the blue and red light are almost equal, the quantum efficiency decreases faster for the 500 nm wavelength (blue) with respect to the 600 nm wavelength (red) when increasing the surface recombination. In fact, since the blue light is absorbed very close to the surface, the photogenerated excess carriers are more subject to recombination taking place at the surface. Note that TCAD simulations are still in agreement with the Generalized Devices network results.

3.3 Phototransistor

The original Generalized Devices model for substrate parasitic currents in HVMOSFET was able to simulate the activation of a bipolar transistor, modeled by back-to-back or front-to-front Generalized Diodes, thanks to the propagation of minority carriers through the MCC from one Generalized Device to another. Following this result, it is interesting to understand whether the novel Generalized Devices can simulate the switching on of a bipolar phototransistor, triggered by light.

The phototransistor is a photodetector that can be built in a standard CMOS process, whose main feature is the internal current amplification. While the photodiode has no inherent amplification and its maximum quantum efficiency, defined as the number of electron–hole pairs which contribute to the photocurrent divided by the number of the incident photons [99], is below unity, the phototransistor can reach *apparent* quantum efficiencies higher than unity. Such an amplification is desirable and important for certain applications involving weak optical signals detection [100]. A phototransistor is a conventional bipolar transistor operated with a floating base contact [3]. Phototransistors have large base-collector junctions, as they are the light-collecting elements. In a pnp phototransistor[1], photogenerated electrons, in the base/collector depletion region and within a distance of the diffusion length, flow to the energy maximum and are trapped into the base. This accumulation of electrons or negative charges increases the base energy (lowers the potential) and allows a large flow of holes from the emitter to the collector. The result is a much larger hole current caused by a small electron current, which is the dominant gain mechanism that is common for both the bipolar transistor and the phototransistor, provided that the hole transit time through the base is much shorter than the minority-carrier lifetime [3]. The major benefit of the phototransistors is the low operating voltages, the low sensitivity to technology and the low dark current when the device operates with a floating base (two-terminal configuration) [101]. The biggest drawback is related to the limited bandwidth, as the inherent larger area (i.e. high capacitances) of phototransistors degrades the high-frequency performances. Moreover, the diffusion of minority carriers in the base limits the switching speed. Nevertheless, bipolar phototransistors find applications at low frequencies or when other solutions cannot be integrated [99], as in opto-isolator applications because they offers a high current-transfer ratio of the order of 50% or more, compared to 0.2% for typical photodiodes [3].

The structure under test is shown in Fig. 3.19 and consists in a pnp bipolar transistor with a floating base contact. The doping concentrations are set to 10^{15} cm^{-3} p-type for the substrate (collector), 10^{16} cm^{-3} n-type for the n-well (base), 10^{17} cm^{-3} p-type for the inner p-well (emitter), and 10^{18} cm^{-3} for the highly-doped regions (p+ and n+ wells) near the contacts. The base n-well has a depth of 2 μm and a width of 6 μm, the emitter p-well depth is 0.5 μm and the width is 2.5 μm, and the highly doped regions have a depth of 0.1 μm and a width of 1 μm. The structure is 2D and has a lateral extension of 1 μm. A sketch of the equivalent network of Generalized Devices is superimposed to the layout of the structure in Fig. 3.19. The actual mesh is finer near the surface and follows the mesh strategy presented in section 2.3.3.

Fig. 3.20 and Fig. 3.21 report the results of simulations for the phototransistor illuminated with a red light (wavelenght of 600 nm), using different light intensities. The results obtained with the Generalized Devices are plotted with solid lines whereas TCAD numerical simulations of the same structure are reported with dots. It can be seen how the optically-triggered, current-amplification effect in the phototransistor is simulated by the GLD model. The error on the photocurrent estimation of the GLD

[1] A negative bias is applied to the collector with respect to the emitter.

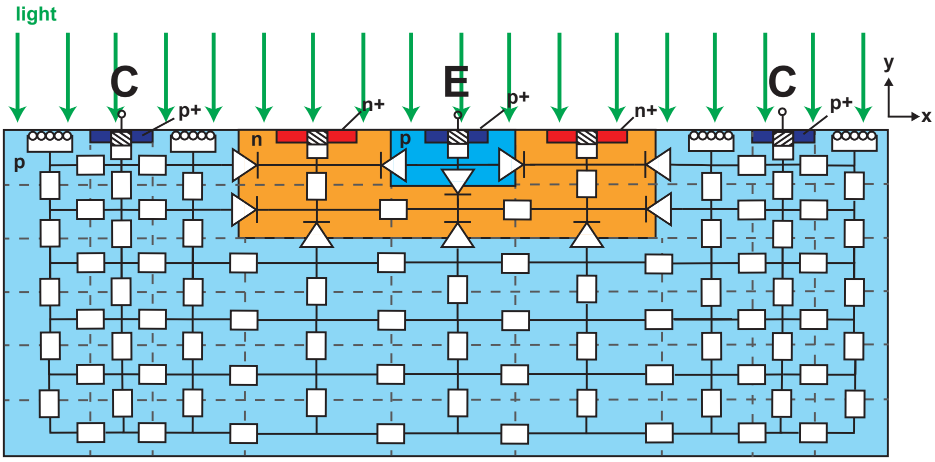

Figure 3.19 – Scheme of the structure of the simulated pnp phototransistor and sketch of its equivalent network of Generalized Devices.

model with respect to TCAD is around 15%. So, the model can predict the switching on and the overall behavior of the phototransistor quite consistently, even though the error is higher with respect to the photodiode and solar cell cases. The results obtained with the Generalized Devices network are convincing and even with an error of around 15%, the model is still very useful to give a first guess of the key phototransistor figures

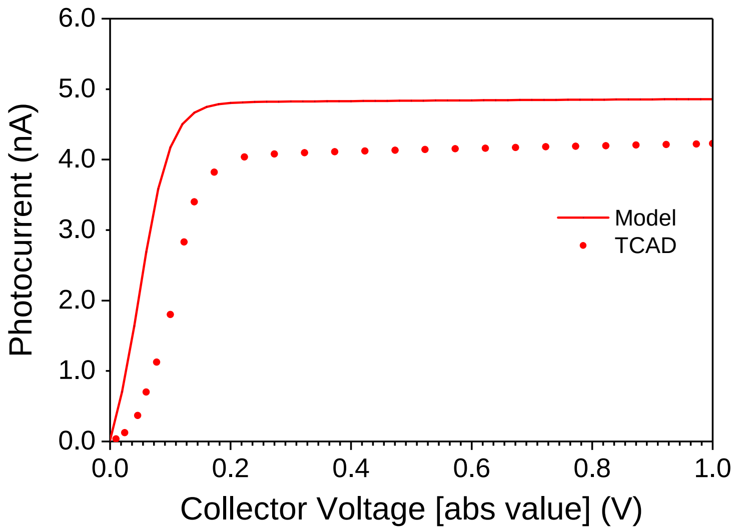

Figure 3.20 – Photocurrent flowing between the emitter and the collector as a function of the collector voltage for an illumination of 10^{-3} W/cm^2 (absolute value in the graph. A negative collector voltage was used in the simulations as the phototransistor is a pnp type). Results obtained with the Generalized Devices approach are shown with solid lines, and TCAD numerical simulations results are reported with dots.

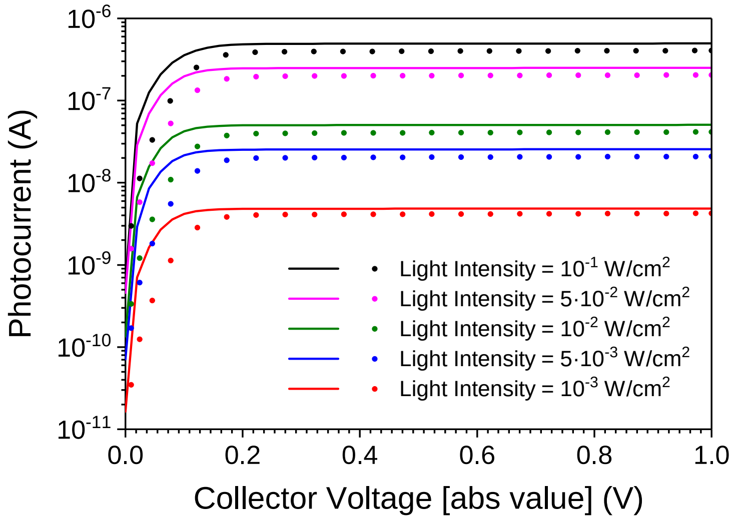

Figure 3.21 – Photocurrent flowing between the emitter and the collector as a function of the collector voltage in log scale for different illumination levels (absolute value in the graph). Results obtained with the Generalized Devices approach are shown with solid lines, and TCAD numerical simulations results are reported with dots.

of merit within short simulation times, much shorter than TCAD simulations.

The Internal Quantum Efficiency [99], i.e. the ratio between the number of charge carriers collected at the contacts over the number of absorbed photons, is about 21. The Responsivity [99], which measures the electrical output per optical input and is defined as the ratio of the photocurrent and the incident optical power, is about 10 A/W, irrespective of the light intensity, as shown in Table 3.1.

Table 3.1 – Responsivity and Internal Quantum Efficiency for the structure in Fig. 3.19

Light Intensity (W/cm^2)	Photocurrent (nA)	Responsivity (A/W)	Internal Quantum Efficiency
0.001	4.23	10.56	21.89
0.005	20.81	10.4	21.55
0.01	41.34	10.33	21.41
0.05	204.27	10.21	21.16
0.1	405.92	10.12	20.97

Fig. 3.22 compares the photocurrent collected by the phototransistor in Fig. 3.19 for an illumination of 10^{-3} W/cm^2 (wavelenght of 600 nm) to the photocurrent collected for the same illumination by the photodiode obtained by removing the emitter p-well

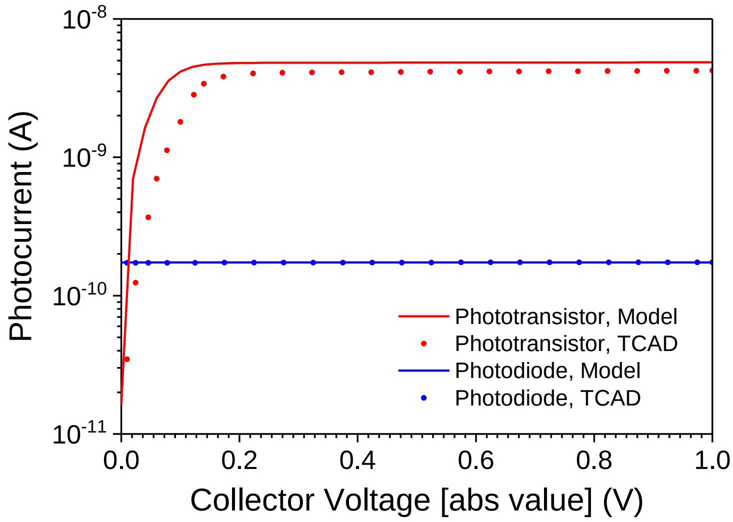

Figure 3.22 – Photocurrent as a function of collector voltage (absolute value) for an illumination of 10^{-3} W/cm^2 in the phototransistor structure of Fig. 3.19, in red, and in the photodiode structure obtained by removing the emitter p-well in the structure in Fig. 3.19. Results obtained with the Generalized Devices approach are shown with solid lines, and TCAD numerical simulations results are reported with dots.

in the structure in Fig. 3.19. The plot clearly confirms the amplification taking place when the emitter well is present.

The Early effect [3] is also taken into account since the model of the Generalized Diode calculates the voltage-dependent, depletion-region widths, as presented in section 2.3.1. The Early effect is negligible for the structure simulated until now because the doping concentration in the base is quite high, and so the depletion width is small with respect to the dimensions of the well. The Early effect starts to be important for a base doping of 10^{15} cm^{-3}, as shown in Fig. 3.23. A lower base doping provides also a higher amplification factor. Thus, the base doping concentration has to be carefully designed in order to meet a trade-off between large amplification (lower doping) and reduced Early effect (high doping). Such an optimization can be carried out directly in SPICE simulation tools using the Generalized Devices modeling approach.

Since Generalized Devices only use geometrical, technological and physical parameters of the semiconductor, it is possible to study the impact of these parameters on the output characteristics. Fig. 3.24 reports the photocurrent for different electron and hole bulk lifetimes collected by the phototransistor of Fig. 3.19, with a doping of 10^{15} cm^{-3} p-type for the substrate (collector), 10^{16} cm^{-3} n-type for the n-well (base), 10^{17} cm^{-3} p-type for the inner p-well (emitter), and 10^{18} cm^{-3} for the homojunctions and considering an illumination of 10^{-3} W/cm^2 and wavelengh of 600 nm. In Fig. 3.25,

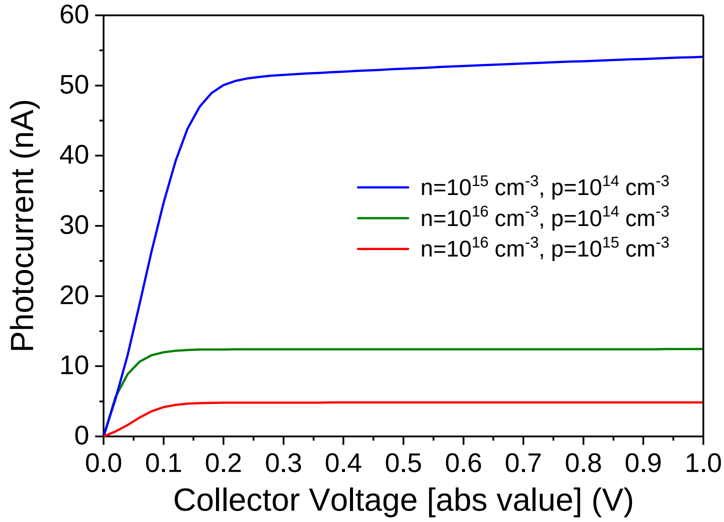

Figure 3.23 – Photocurrent as a function of collector voltage (absolute value) for an illumination of 10^{-3} W/cm^2 for different doping concentrations of the base (n-well) and collector (p-substrate). Results are obtained with the Generalized Devices approach.

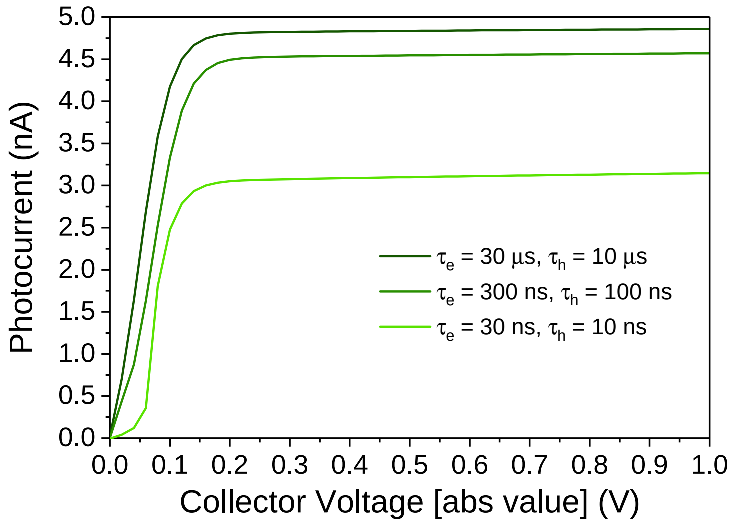

Figure 3.24 – Photocurrent as a function of the collector voltage (absolute value) for an illumination of 10^{-3}W/cm^2. Values of bulk electron (τ_e) and hole (τ_h) lifetime are varied. Results are obtained with the Generalized Devices approach.

the results for different surface recombination velocities are shown. As expected, the photocurrent decreases with increasing carrier recombination (lower bulk lifetimes) and higher surface recombination velocities. Finally, the Responsivity and the Internal Quantum Efficiency, considering a collector voltage of -1 V, as a function of bulk lifetime (holes lifetime on the x-axis) and surface recombination velocity are

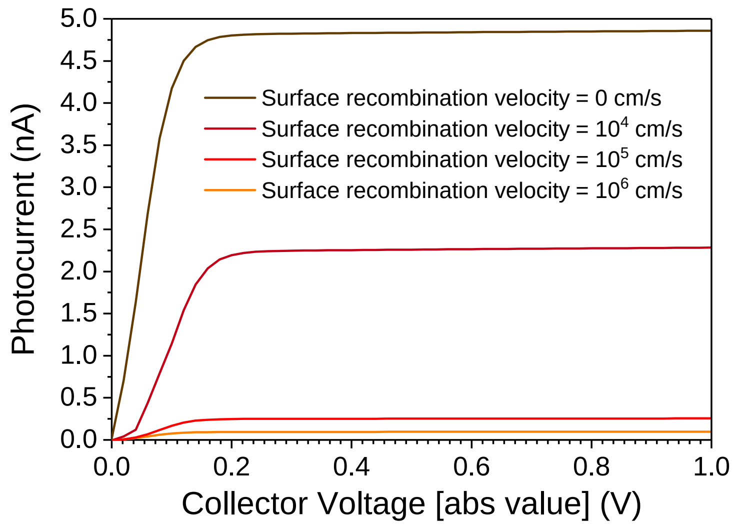

Figure 3.25 – Photocurrent as a function of the collector voltage (absolute value) for an illumination of 10^{-3} W/cm^2. Values of surface recombination velocity are varied. Results are obtained with the Generalized Devices approach.

calculated, from the results shown in Fig. 3.24 and Fig. 3.25, and are plotted in Fig. 3.26 and Fig. 3.27.

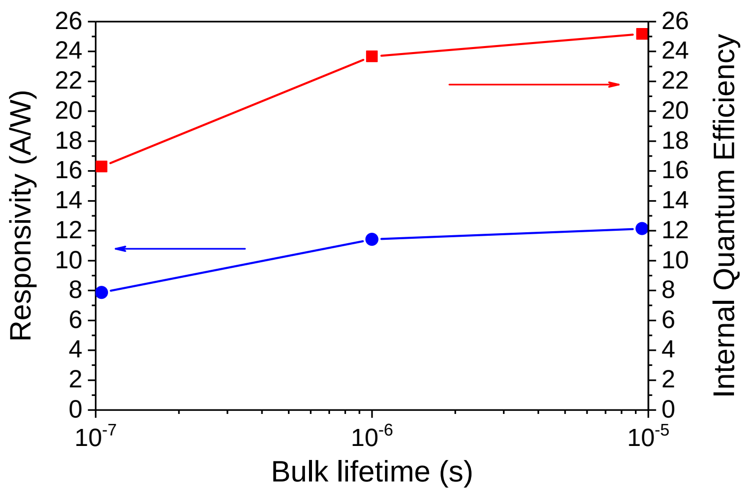

Figure 3.26 – Responsivity and Internal Quantum Efficiency plotted as a function of hole bulk lifetimes, for an illumination of 10^{-3} W/cm^2. Results are obtained with the Generalized Devices approach.

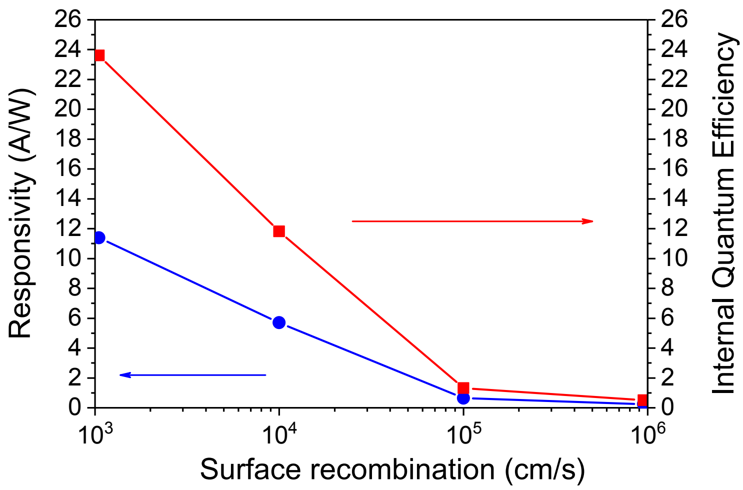

Figure 3.27 – Responsivity and Internal Quantum Efficiency plotted as a function of surface recombination velocity, for an illumination of 10^{-3} W/cm^2. Results are obtained with the Generalized Devices approach.

3.4 CMOS APS

The last optoelectronic device investigated is a pixel of an CMOS Active Pixel Sensor (APS) imager. A CMOS APS is an image sensor that is composed by an array of active pixels, i.e a specific architecture that includes a photodiode and a read-out in-pixel circuit to measure the intensity of light. Since the Generalized Devices model is SPICE compatible and its simulations are run in the SPICE environment with standard circuit simulators, it is possible to co-simulate the equivalent network of GLD that simulates the optoelectronic device with any external circuit, described with compact models. The GLD approach can be a powerful tool in this scenario as does not require a specific compact model for the photodiode, which is usually strictly linked to the geometry and technological parameters of the semiconductor structure. It can provide flexibility in the design of the APS, help in the optimization of the parameters of the photodetector at the layout level, and assess the impact of the semiconductor parameters on pixel performances directly during SPICE simulations, thus avoiding time-consuming and costly fabrication process modifications or long and complex numerical simulations. In the next sections, the feasibility of the GLD model in predicting the operation of APS pixels is studied. Also in this case, TCAD simulations will be run for the same structure to validate the model, using the same geometrical and technological parameters inserted in the network of GLD.

3.4.1 Architecture and principle of an APS pixel

A typical 3T-APS pixel architecture is shown in Fig. 3.28 [102, 103]: each APS pixel is composed of a photodiode and three MOSFETs. Prior to the measurement, the photodiode is reverse biased up to $V_{DD} - V_{TH}$ [104] by means of T1 during the reset time, which increases the depletion charge density of the junction capacitance. Next, during the integration time, T1 is switched off. The photogenerated electron-hole pairs that are separated by the electric field in the depletion region are drifted away, resulting in a discharge of the photodiode capacitance. This will decrease the potential on the gate of T2. Therefore, the discharge time will depend on the optically-generated excess carriers, i.e., will depend on the light intensity. The output signal of the pixel, provided by the source follower transistor T2, is sampled at the end of the integration time (i.e., readout time, see Fig. 3.28). The select transistor, which can be omitted in this case, is part of the row and column selection circuits to access specific pixels in an image sensor. In fact, in CMOS imagers, voltage signals are readout one row at a time in a manner similar to a random access memory [105].

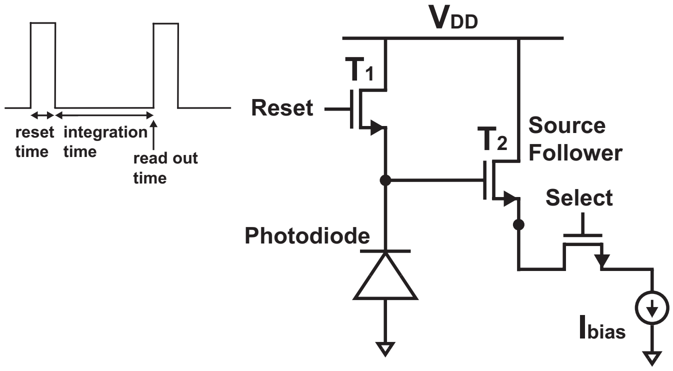

Figure 3.28 – Architecture of a 3T-APS pixel.

3.4.2 Simulation of a single pixel

The structure under test is presented in Fig. 3.29. The photodiode is modeled by the network of Generalized Resistors, Diodes, Homojunctions and Surface Recombination Elements and the usual meshing strategy presented in section 2.3.3 applies also in this case. The n-well of the photodiode has an area of 30 μm^2, it is 3 μm deep and doped at 10^{16} cm^{-3}. The p-substrate is doped at 10^{16} cm^{-3}, and highly doped regions (10^{19} cm^{-3}) are used for Ohmic contacts. The structure has a 2D dimensionality. A monochromatic light with a wavelength of 600 nm (red light) is used for illumination. Standard compact models are used for the transistors. In particular, the two transistors T1 and T2 are simulated using the BSIM3 compact model (a 0.18 μm CMOS technology is considered) and both have a channel length and width of 180 nm and 240 nm,

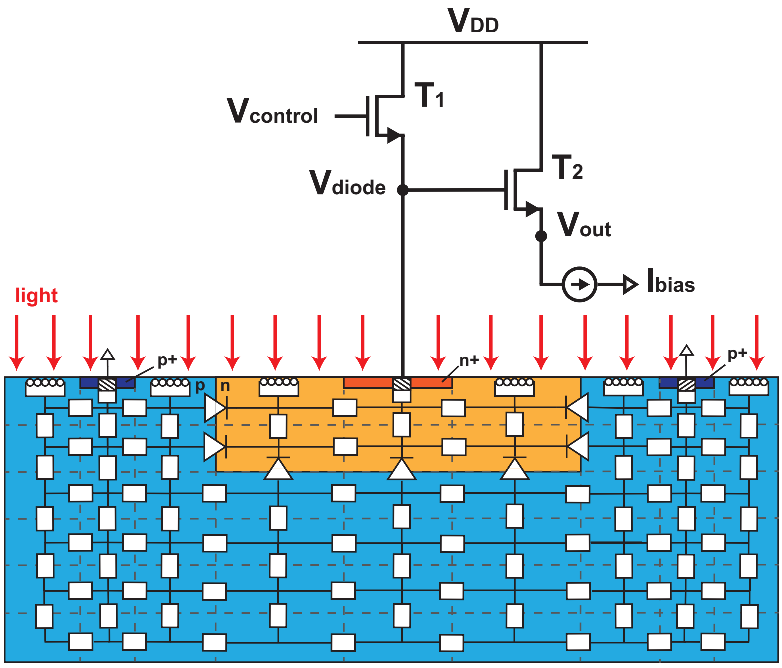

Figure 3.29 – Equivalent APS circuit with Generalized Devices.

respectively. The select transistor is neglected. The bias voltage (V_{DD}) and bias current (I_{bias}) are set to 3.3 V and 1 μA. Fig. 3.30 shows the voltage on the cathode of the photodiode (connected to the gate of T2) for different illumination intensities during reset and integration times. The GLD model (solid lines) is in good agreement with the numerical simulations (dots) performed with Sentaurus TCAD, using the same physical and technological parameters. As already stated in section 2.3.3, also in this case the computation time required for the SPICE simulation of the structure using the Generalized Devices approach is about three orders of magnitude lower with respect to the computation time required for the TCAD numerical simulation of the same structure using the same hardware. Nevertheless, SPICE simulations of GLD model predict accurately the transient discharge of the photodiode capacitance upon illumination, as well as the saturation of the signal for high light intensities. Indeed, for a given integration time, there is a particular value of the light intensity that fully discharges the capacitance (i.e., zero voltage at the cathode of the photodiode). For higher illumination densities, this zero voltage is reached before the end of the integration time, which would require shorter integration periods. Given that the photodiode and the circuit are co-simulated in SPICE, the output voltage of the APS circuit is obtained in the same simulation. The different curves in Fig. 3.31 represent the output voltages readout after different integration time. Again, the results obtained with the model match quite well TCAD simulations, including the slightly non-linear dependence. Decreasing the integration time, higher light intensities could also be

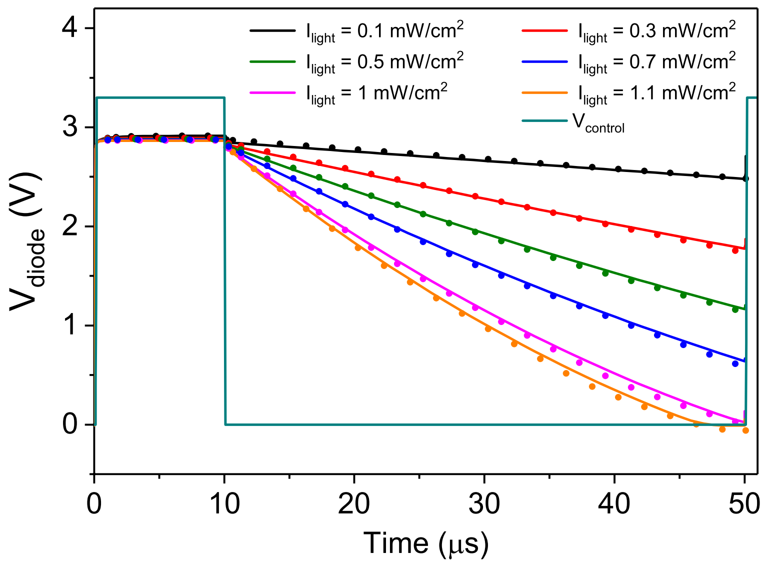

Figure 3.30 – Time dependence of the voltage at the cathode of the pn junction under illumination for different light intensities. Results obtained with the Generalized Devices model are plotted with solid lines while TCAD simulations results are plotted with symbols.

detected, but this will also degrade the resolution for lower intensities. Therefore, the integration time is critical and depends on the range of illumination foreseen. Using the GLD modeling approach, this kind of technological-versus-circuit optimization can be carried out during SPICE simulations.

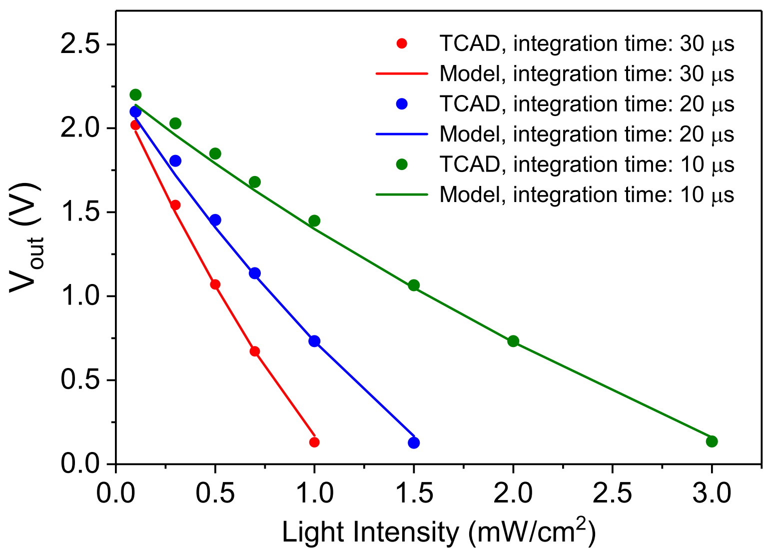

Figure 3.31 – APS output voltage at the source of T2 as a function of illumination intensity for different integration times.

Prediction of the impact of semiconductor parameters on pixel output

Since the Generalized Devices approach relies on geometrical and physical parameters only, it can also be used to study the how those parameters affect the output voltage, and so the overall APS performance.

Bulk lifetime The recombination lifetime plays an important role when dealing with optoelectronic devices since the collection efficiency of photogenerated carriers can drop dramatically when the carrier lifetime is small, i.e., in the ns range. The lifetime of electrons and holes in the semiconductor substrate was varied from 30 μs for electrons and 10 μs for holes, down to 3 ns for electrons and 1 ns for holes. As can be noticed in Fig. 3.32, the mismatch increases for shorter lifetimes. This is because the diffusion length decreases with decreasing lifetime, thus requiring a finer mesh for an accurate linearization, as explained in section 2.3.3. The simulations reported in Fig. 3.32 predict a limited range of the output voltage variation when decreasing the carrier lifetimes. To overcome this issue, the integration time should be increased in order to obtain a steeper slope for the dependence of the output voltage on the light intensity.

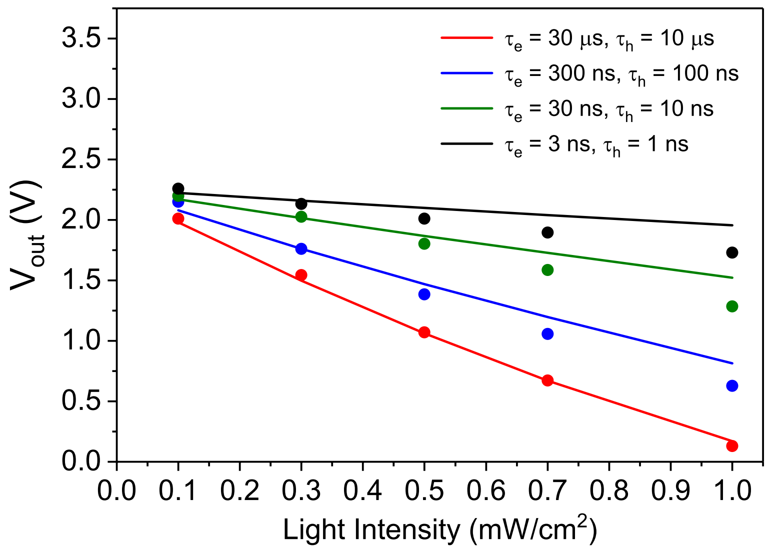

Figure 3.32 – Impact of electron lifetime (τ_e) and hole lifetime (τ_h) on the APS output voltage for an integration time of 30 μs (solid lines for GLD model results and symbols for TCAD simulations).

Surface recombination As seen above, another important semiconductor parameter that must be taken into account when dealing with optoelectronics is the surface recombination velocity. In fact, surface recombination can significantly degrade the photodiode performances, as light absorption peaks at the semiconductor surface.

Simulations including surface recombination velocities based on the Generalized Devices and TCAD simulations presented in Fig. 3.33 confirm that this feature can also be tracked during SPICE simulations.

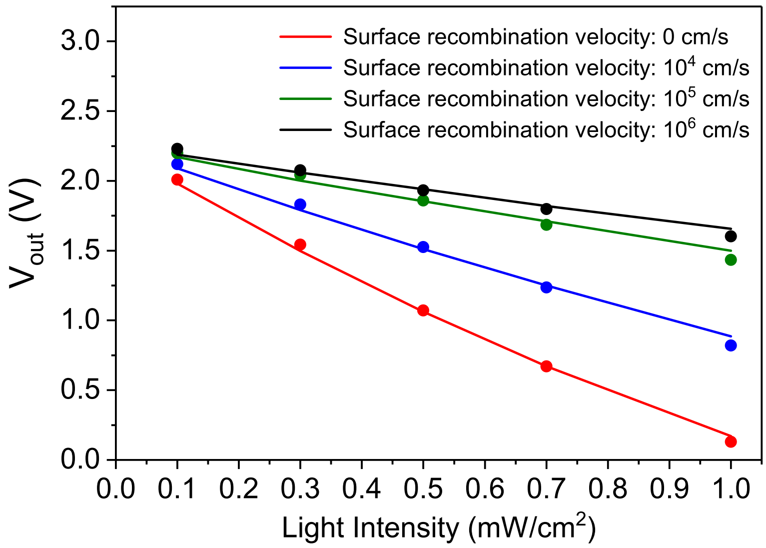

Figure 3.33 – Impact of the surface recombination velocity on the APS output voltage for an integration time of 30 μs (solid lines for GLD model results and symbols for TCAD simulations).

Doping concentration The output voltage of the APS is analyzed for different doping levels of the p-type substrate and n-well. The doping affects the depletion region, and so the capacitance of the photodiode which translates light into an electrical quantity. As such, it has a key role in the operation of the pixel sensor, in addition to modifying the built-in voltage. Fig. 3.34 shows the results obtained with the Generalized Devices model and TCAD simulations. For lower doping densities, the depletion region increases and the photodiode capacitance decreases. Therefore, keeping the same reverse bias voltage during reset mode, it makes the stored charge lower. Since for a given light intensity the electron-hole pairs generation will not change, the charge in the junction capacitance and the resulting voltage on the cathode of the photodiode will decay faster, resulting in a lower output voltage of the APS sensor at the end of the integration time, 10 μs in this case. Note that for the intensity of light used in this work, longer integration times would totally discharge the capacitance of the photodiode when the doping densities are set to 10^{15} cm^{-3} (same for n and p type), meaning that the output signal would saturate.

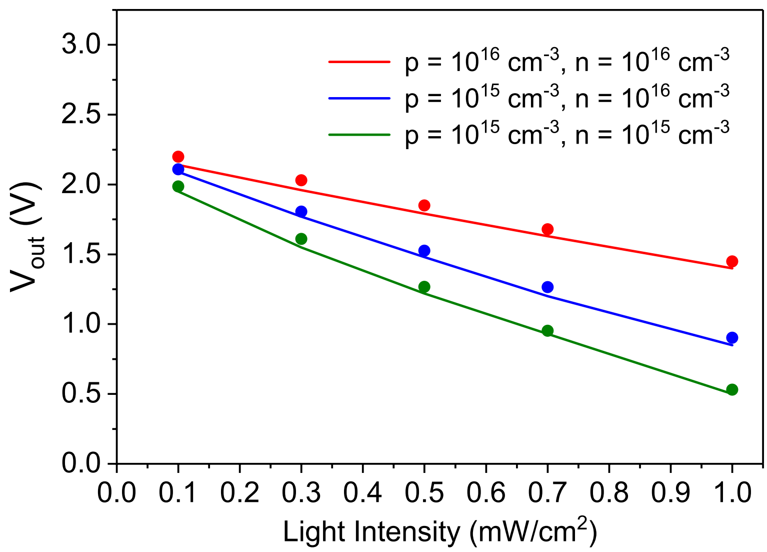

Figure 3.34 – Impact of the p-substrate and n-well doping densities on the APS output voltage for an integration time of 10 μs (solid lines for GLD model results and symbols for TCAD simulations).

3.4.3 Crosstalk between adjacent pixels

In addition to the pixel sensitivity, the GLD modeling approach permits the prediction of crosstalk between pixels, another key parameter to describe the performance of an image sensor. The crosstalk in APS originates when a pixel at dark behaves as if it were impinged by light. While the optical crosstalk could originate if photons reach a dark pixel due to light beam scattering in the optical microlenses, the electrical crosstalk happens when carriers photogenerated in the illuminated pixel diffuse further towards neighbor pn junctions and produce a signal [50]. Such a crosstalk is becoming a critical factor in new technologies as it gets worse when pixels shrink, seriously damaging the sensor resolution [53]. Crosstalk modeling, especially electrical crosstalk, is thus mandatory to optimize pixel design. However, as presented in section 2.2, developing an analytical model is challenging and only few analytical and semianalytical models can be found in literature. Instead, the network of Generalized Devices can easily simulate crosstalk, as the modeling of the diffusion of excess carriers in the semiconductor substrate is one of the key feature of the approach.

Multiple definitions of crosstalk can be found in literature [70, 106]. Here, the following definition is used:

$$CKT(\%) = \frac{\Delta_D - \Delta_{ID}}{\Delta_L - \Delta_{ID}} \cdot 100 \tag{3.4}$$

where Δ_L and Δ_D are the differences in the output voltage taken at the beginning and

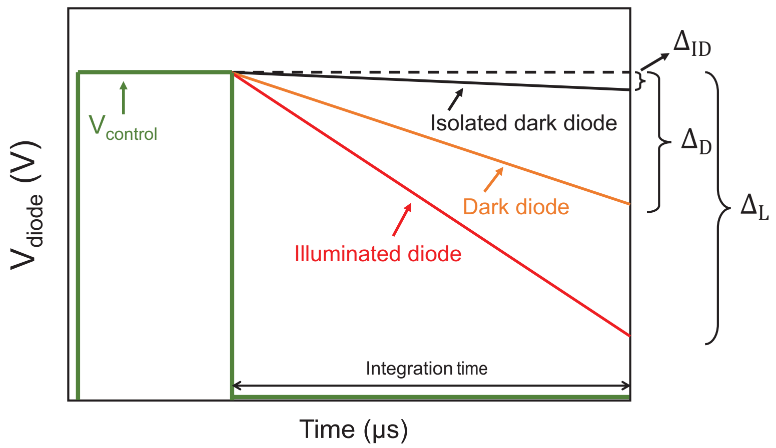

Figure 3.35 – Definitions of voltage drops (Δ_L, Δ_D and Δ_{ID}) on the cathode of the photodiodes in case of illuminated pixel, dark pixel and isolated dark pixel.

the end of the integration time for the illuminated pixel and dark pixel respectively (i.e., the non-illuminated pixel in the neighborhood of the illuminated pixel subjected to crosstalk), and Δ_{ID} is the difference in the output voltage between the beginning and the end of the integration time for an isolated dark pixel (i.e., the voltage drop is only due to the thermal current of the pn junction). The definitions of Δ_L, Δ_D and Δ_{ID} are graphically explained in Fig. 3.35. Adopting this definition, the crosstalk between two pixels is simulated using the Generalized Devices modeling approach and compared with TCAD simulations. The structure under test is reported in Fig. 3.36. The pixel on the right side (pixel 2) is illuminated while the pixel on the left side (pixel 1) receives no light at all. This configuration represents the worst case scenario when dealing with crosstalk since photodiodes are separated by the minimum distance as there is no in-pixel electronics between them [69]. Fig. 3.36 sketches the network of Generalized Devices used to model the semiconductor structure, which is connected to the compact models for the in-pixel circuit. It is important to note that the network of Generalized Devices interconnects the dark and illuminated pixels and can thus simulate the propagation of photogenerated carriers from one pixel to the other. This is the key feature enabling prediction of crosstalk between pixels. Moreover, as already stated above, there is no need of any fitting parameter, as the model is physics based and only uses geometrical and technological parameters.

Front-side illumination

Crosstalk is firstly simulated in case of a front side illumination of the pixel 2 (see Fig. 3.36). Each pixel has the same dimensions as the one simulated in section 3.4.2,

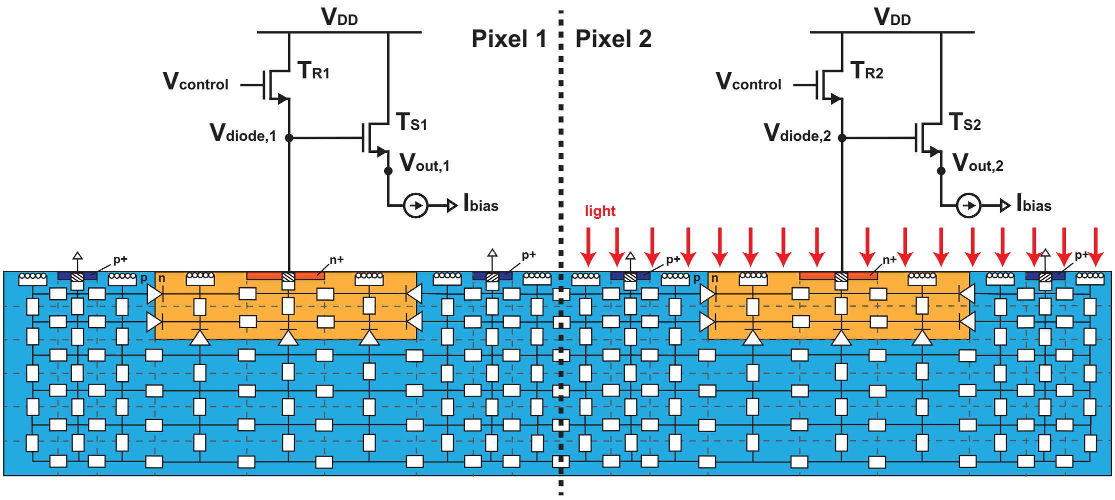

Figure 3.36 – Equivalent circuit with Generalized Devices for two adjacent pixels.

and the distance between the pn junctions is set to 30 μm. Fig. 3.37 shows the time evolution of the voltage on each photodiode during the integration time. The reset signal (V_{control}) for the integration time is the same for both pixels. Moreover, the time dependence of the voltage for an isolated photodiode at dark (isolated structure with no collection of photogenerated carriers from neighbor pixels, i.e., only subjected to thermal generation) is also plotted in Fig. 3.37. The GLD model (solid lines) is in good agreement with the TCAD simulations (symbols) performed on the same

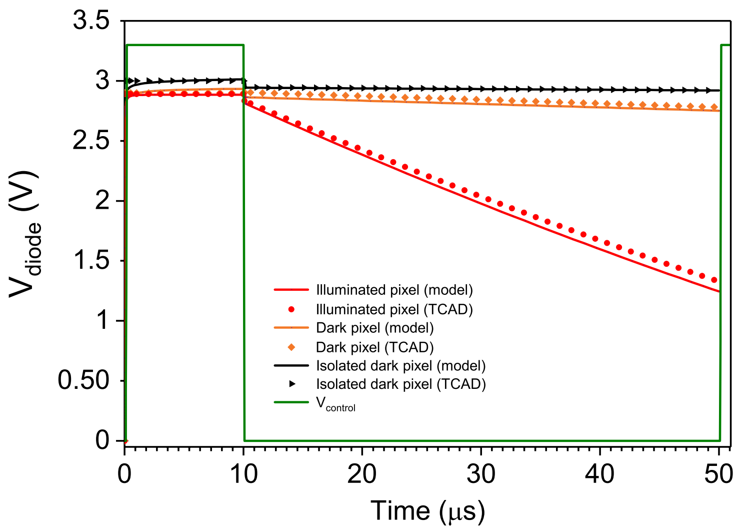

Figure 3.37 – Crosstalk study for front-side illumination: time dependence of the voltage at the cathode of the pn junctions for different illumination conditions. Results obtained with the Generalized Devices model are plotted with solid lines while TCAD simulations results are plotted with symbols.

structure. The crosstalk predicted with the model is about 11%, while for TCAD it is of 7.9%. This confirms that the network of Generalized Devices can simulate not only the photogeneration of carriers in the illuminated pixel, but also their propagation and collection towards each pn junction with enough accuracy for a fair evaluation of crosstalk simulated at the output node of the photodiodes.

Back-side illumination

In recent years, the demand for higher resolution cameras has led to dramatic pixel shrinkage. As a consequence, the percentage of pn junction area exposed to impinging light (not shadowed by metallic interconnections) decreased by a great amount. To solve this issue, state-of-the-art CMOS image sensors are using back-illuminated pixel technology. The back-side illumination requires the thinning of the active silicon layer (where photogeneration takes place) in order to avoid excessive crosstalk. In fact, as will be seen later, crosstalk strongly depends on the silicon layer thickness. Papers in recent literature report that for pixel sizes of 1 μm to 3 μm, the silicon thickness is about 3-4 μm [107, 108, 109, 110, 111, 112, 113]. Following this analysis, crosstalk is now studied considering back-illuminated pixels, with a size of 3 μm, a silicon thickness of 4 μm, a pn junction width and depth of 1.5 μm and a distance between two adjacent pn junctions of 1 μm.

In-pixel circuit using switches The 2-pixel structure is simulated first by substituting all the transistors in Fig. 3.36 with simple passive switches in order to avoid considering transistors compact models and focus on the substrate model only. Indeed, in this case the photodiode is much smaller than in the previous case-studies and the transistor capacitances cannot be neglected with respect to the capacitance of the photodiode. Thus, MOSFET capacitances can be responsible for non-idealities in the voltage characteristics. For a proper validation of the model, this must be identified separately. Fig. 3.38 reports the simulations for the model and TCAD with ideal switches. The pixel on the right side (see Fig. 3.36) is illuminated with a red light (wavelength of 600 nm) using an intensity of 1 mW/cm^2 while the left one is not illuminated. The bias voltage V_{DD} is set to 1.2 V and the integration time to 40 μs. To improve the accuracy of the simulation, the model of the Generalized Diode is slightly modified, to take into account corners of the pn junction. The pn junction is modeled using several Generalized Diodes in parallel. Up to now, the model used an equivalent length given by the sum of the bottom and lateral sides of the rectangle, thus ignoring 2D effects. Results were still accurate as the contributions to the depletion region of corners was negligible. As the size of the pn junction shrinks, its shape looks more as a square than an elongated rectangle. To take into account this, the overlap between the

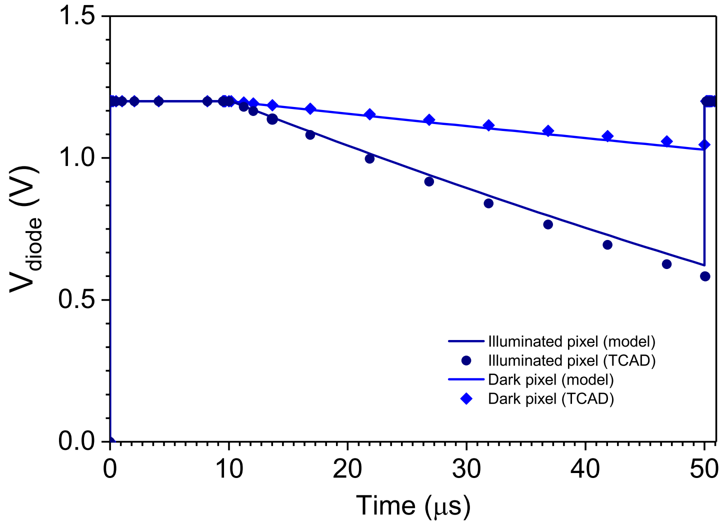

Figure 3.38 – Crosstalk study for back-side illumination (smaller pixels) with no in-pixel transistors, only switches: time dependence of the voltage at the cathode of the pn junctions for different illumination conditions. Results obtained with the Generalized Devices model are plotted with solid lines while TCAD simulations results are plotted with symbols.

depletion regions[2] at the corners is suppressed. This solution was adopted because deriving a depletion region in 2D for corners is not straightforward. In addition, this would make the model quite complex, while this simplified view gives acceptable results. Indeed, the model can accurately predict the voltage characteristics of each diode as shown in Fig. 3.38. The crosstalk obtained with the model is 27.4% compared to 24.8% for TCAD.

In-pixel circuit using transistors Since the intrinsic pixel operation, without transistors, has been validated, the complete pixel architecture including all the transistors is now assessed. Fig. 3.39 reports the time evolution of the voltage on the cathode of the two photodiodes (one in the illuminated pixel and one in the non-illuminated pixel) simulated with the GLD model and with TCAD. An external capacitance of 0.1 fF has been added between the gate and the source of the transistors in the model in order to precisely match the capacitances in the compact model of the transistor used in the TCAD tool. In fact, any minor difference in compact models (especially for capacitances) can lead to a significant mismatch for such small pixel dimensions since transistors capacitances are no longer negligible with respect to the capacitance of the photodiode. For instance, as can be noted in Fig. 3.39, the presence of transistors instead of switches is responsible for a jump in the transient characteristics, a feature that was not present in Fig. 3.38 (pixel with ideal switches). This jump is attributed to

[2]The depletion region width is still calculated under the full depletion approximation in one dimension.

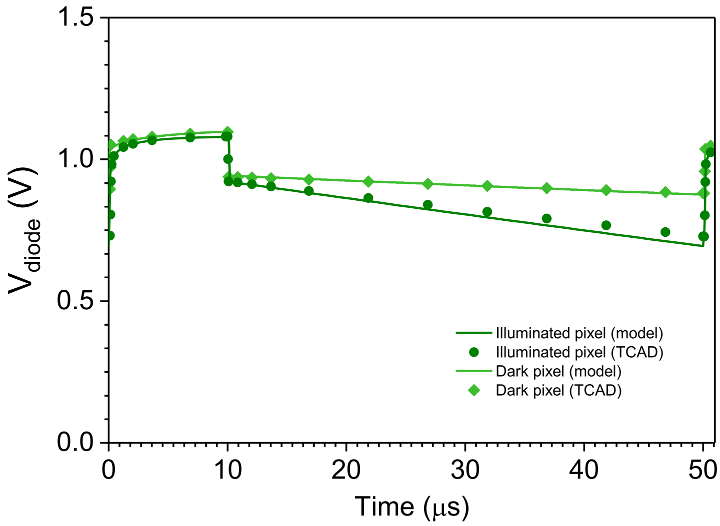

Figure 3.39 – Crosstalk study for back-side illumination (smaller pixels) with in-pixel transistors: time dependence of the voltage at the cathode of the pn junctions for different illumination conditions. Results obtained with the Generalized Devices model are plotted with solid lines while TCAD simulations results are plotted with symbols.

the charge injection from the MOSFETs when switching. In conclusion, the model can simulate the full architecture of the pixel including now the transistors as in regular APS, both for front and back side illumination and with state-of-the-art dimensions. Not only the output voltage, but also crosstalk figures of merit can be predicted within the same SPICE environment. In this last case, the crosstalk predicted with the model is 24.3%, very close to the value simulated with TCAD, i.e., 23%.

Impact of silicon layer thickness and wavelength on crosstalk As stated before, the thickness of the silicon layer is a key feature for the optimization of the sensitivity to light and crosstalk in back-illuminated APS. Fig. 3.40 reports the crosstalk as a function of the silicon thickness for different wavelength (corresponding to blue, green and red light). The crosstalk simulated with the GLD model (solid lines in Fig. 3.40) is in good agreement with TCAD results (symbols) for a wide range of silicon thicknesses and wavelengths. It is possible to note how large the crosstalk becomes for high thicknesses, reaching already 50% for about 5 μm. Based on these SPICE simulations, the acceptable values of silicon thickness are found to be in the range of 3–4 μm (the same found in literature for fabricated pixels), as thinner thicknesses would provide a signal on the illuminated pixel that is too low. This illustrates how physics-based design of pixel layout can be carried out using SPICE circuit simulators.

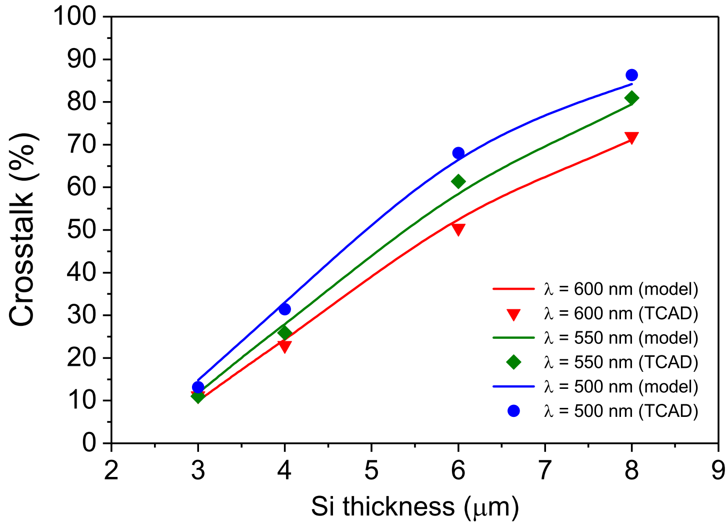

Figure 3.40 – Impact of silicon layer thickness in back-side illuminated pixels and wavelength on crosstalk (solid lines for model results and symbols for TCAD simulations).

3.5 Conclusion

The modeling approach based on the Generalized Lumped Devices for the simulation of photogenerated excess carriers in semiconductor structure, developed in this thesis, has been applied to several optoelectronic devices. It has been shown that it can correctly predict the static and dynamic behavior of a photodiode, as well as the full IV characteristics of a solar cell, from short-circuit to open-circuit condition. The model provides accurate results for a wide range of illumination intensities. Moreover, the optically-triggered switching-on of a bipolar phototransistor has been simulated with the network of Generalized Devices. Finally, the simulation of a CMOS APS image sensor pixel has been presented, including the estimation of the crosstalk between two adjacent pixels.

It has been proved that this modeling approach can be successfully used in a variety of scenarios and represents an effective tool for optoelectronics simulations.

Part II
Radiation interaction with ICs substrate

4 Modeling of ionizing radiation effects in ICs substrate

4.1 Basics of radiation-semiconductor interaction

Radiation can deeply affect the operation of semiconductor devices. Energetic particles impinging on a semiconductor mainly lose energy by the following mechanisms [19]:

- ionizing energy loss by inelastic collision of a charged impinging particle with the semiconductor target, resulting in electron-hole pair production (hard collisions) or atom excitation (soft collisions);
- non-ionizing energy loss caused by elastic collision, in which the impinging particle transfers momentum to the target atoms, resulting in phonon production and displacement of lattice atoms from their position in the crystal, thus causing defects in the structure. Elastic collisions usually happen at the end of radiation path in matter, when its energy is low;
- nuclear reactions, in which the collision between the nuclei produces one or more different nuclides than the initial ones.

Other processes, much rarer than atomic collision [114], can occur due to radiation interaction with matter, such as emission of Cherenkov radiation, i.e. an electromagnetic radiation produced when a charged particle travels in the target material faster than the speed of light in that material, and bremsstrahlung (braking radiation), i.e. the emission of electromagnetic radiation due to the deceleration of a charged particle deflected by an electron or nucleus in the target material (the energy lost by deceleration is converted to light).

4.1.1 Ionizing radiation

For charged particles, ionization is the main phenomenon that causes energy loss and so the slow down of the particle. The energy loss is the result of several collisions in

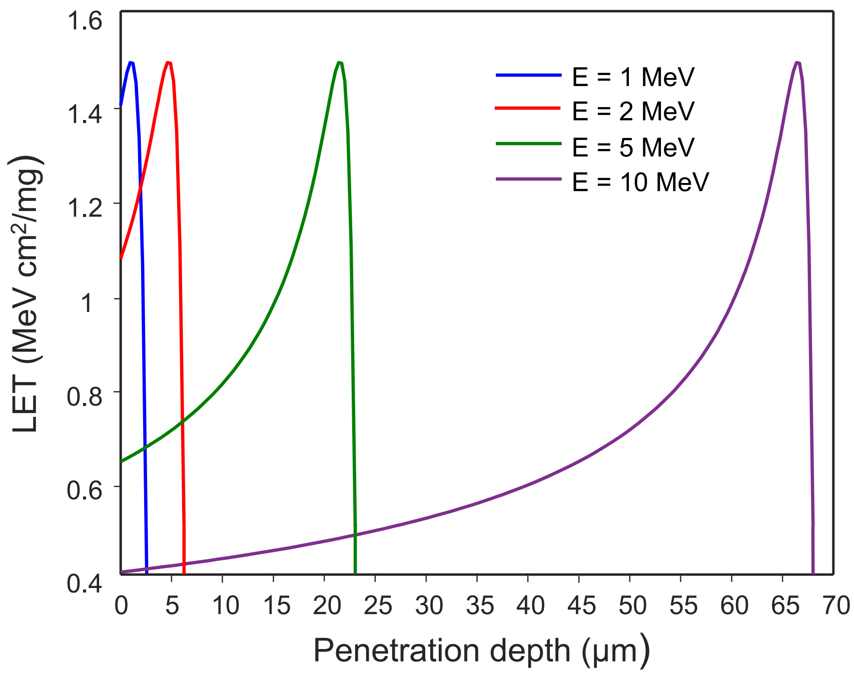

Figure 4.1 – LET as a function of penetration depth of alpha particles in silicon.

which the energy transfer is very small, thus the particle trajectory is not modified [2]. Two quantities are used to characterize the ionization process: the stopping power, that is the amount of energy loss per unit length, and the range, i.e. the distance traveled by the particle in the target material. The stopping power is divided in electronic stopping power, due to collisions with electrons of target material atoms and nuclear stopping power, due to collisions with nuclei of target atoms. The stopping power depends on the impinging particle, on its energy, and on the target material and is usually calculated using Monte Carlo simulations; the most common simulators is SRIM (Stopping and Range of Ions in Matter) [115]. The electronic stopping power is typically named Linear Energy Transfer (LET), which is defined as the rate of energy loss per unit length due to ionization. Its appropriate SI unit is N, however, the LET is usually expressed in MeV/cm or pC/μm. A *weighted* Linear Energy Transfer (LET) can be defined as the electronic stopping power divided by the target material density and expressed in MeV cm^2/mg [2]. An example of LET, plotted as a function of distance traveled in the semiconductor, is shown in Fig. 4.1 for alpha particles, with energy ranging from 1 MeV to 10 MeV, impinging on silicon. The LET increases with the distance traveled by the alpha particle in silicon until it reaches a maximum right before the range (distance at which LET is zero), then it decreases abruptly. This maximum is called Bragg peak and is the point in which the charge generation is the most effective.

4.1.2 Ionization by secondary particles

Ionization occurs when the incident particle is charged. Neutral particles can cause an indirect ionization, i.e. after a nuclear reaction, a charged recoil product is emitted, that can produce ionization [2, 116, 8]. This process is particularly important for neutrons interacting with semiconductors. In fact, indirect ionization caused by neutrons is one of the major cause of dysfunction in integrated circuits due to radiation at ground level [117]. Neutrons interacting with silicon can produce a wide range of recoil products, ranging from protons to ions with atomic number equal or lower than silicon [8]. Such neutrons originate from cosmic rays, which are responsible of radiation environment in the atmosphere. Because of the interaction with air nuclei, high-energy particles from cosmic rays generate large cascades of secondary particles, composed of protons, neutrons, electrons, pions, muons, etc., as shown in Fig. 4.2, with maximum density at the Pfotzen point, i.e. about 15 km of altitude, just above airplane altitudes [7]. It was noted that less than 1% of the primary galactic particles can create a cascade which arrives at sea level since most of the particles are absorbed: they either decay spontaneously or lose energy [7]. The most abundant particles that reach ground level are muons and neutrons, followed by protons and pions. Earth magnetic field can stop charged particles from cosmic rays under a certain value of magnetic rigidity (geomagnetic cut off, that varies with location), hence the flux of

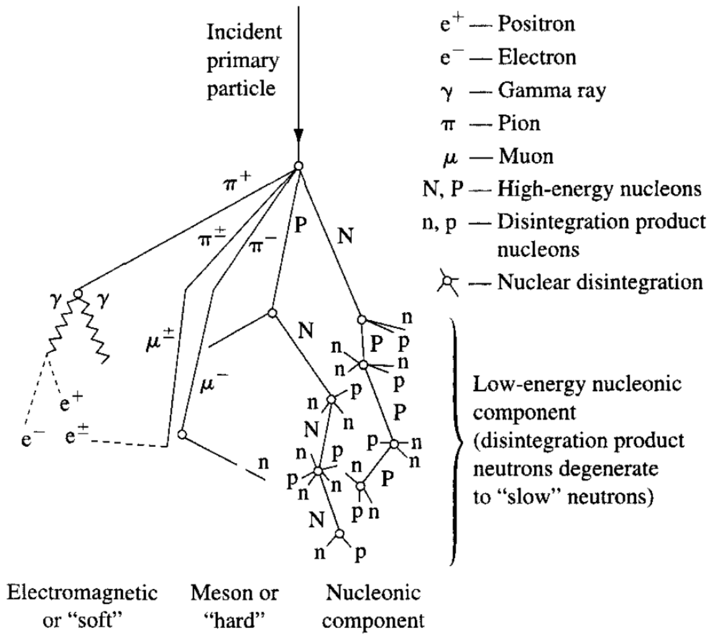

Figure 4.2 – Cascade of secondary particles generated in the atmosphere by a primary cosmic ray (Adapted from [7]).

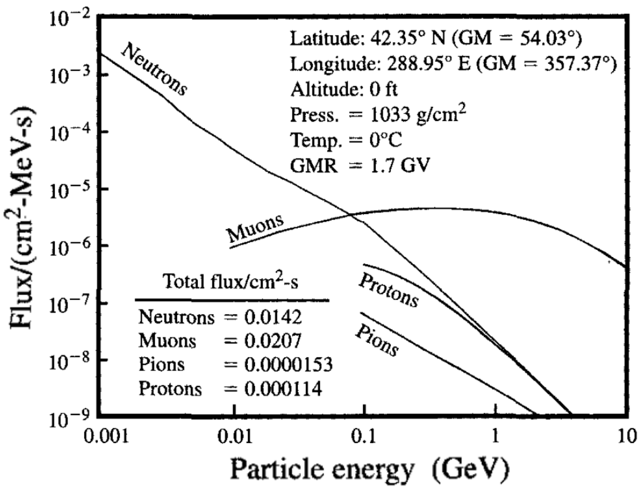

Figure 4.3 – Theoretical ground level secondary particle flux, generated by cosmic rays, in New York City (Adapted from [7]).

secondary particles at ground level depends on it. The secondary flux at ground level, calculated theoretically at the location of New York City, is reported in Fig. 4.3 while the experimental data for secondary particles flux at different sites on Earth can be found in [7].

Another source of neutrons able to produce indirect ionization is boron, that is extensively used in fabrication of integrated circuits as p-type dopant in silicon. The isotope ^{10}B (19.9% abundance) is unstable when exposed to neutrons and has an interaction cross section which is higher by three to seven orders of magnitude in comparison to most other isotopes present in semiconductor materials. Moreover, the reaction has a very high probability to generate two ionizing particles (alpha particle and Li ion) [2]. Boron is also present in borophosphosilicate glass (BPSG), but most modern semiconductor processes have eliminated the presence of ^{10}B in BPSG or they do not use BPSG, that is the primary reservoir of ^{10}B. The same is not possible for silicon doping, since the processes are not selective for isotope and use natural boron [2].

Predicting ionization in semiconductors given by impinging neutrons is thus a two-step process. Firstly, the probability associated to each of the recoil particles has to be assessed. This is usually done with specific simulators for particle-matter interaction that are based on the Monte Carlo method. An example of probability curves for recoil products of 1 GeV neutron impinging on silicon can be seen in Fig. 4.4. Then, the LET of such recoil particles has to be derived as a function of particle energy. As stated above, this can be done by using specific simulators, such as SRIM [115]. For interaction of neutrons with silicon, LET of all possible recoil products are reported in Fig. 4.5. The phosphorus ion, which has the highest LET, is also a potential product

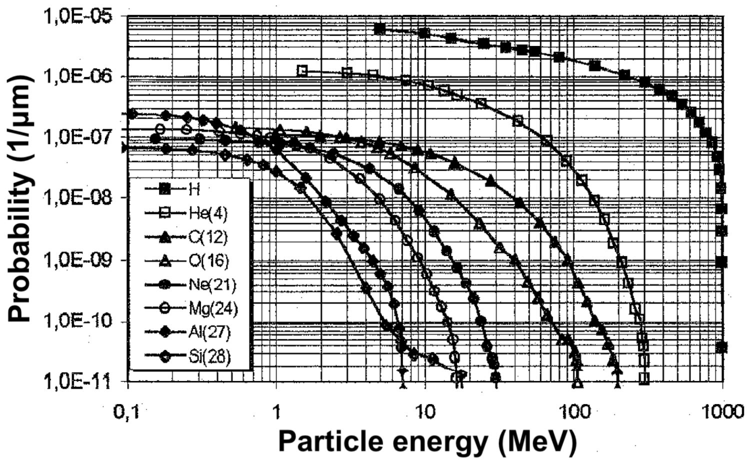

Figure 4.4 – Example of integral probability curves for recoil products considering 1 GeV neutron impinging on silicon (Adapted from [8]).

of this interaction, even though its atomic number is higher than that of silicon. The probability associated to this product is however very low, as the reaction, that corresponds to ^{30}Si capturing the incident neutron and decaying by beta emission, is very rare.

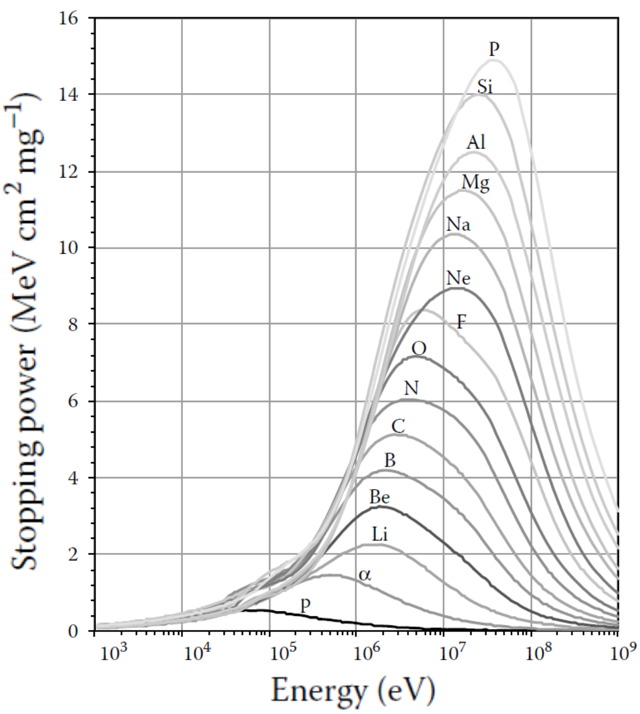

Figure 4.5 – Electronic stopping power as a function of particle energy for all the possible recoil products given by the interaction between neutrons and silicon (Adapted from [2]).

4.2 Radiation effects in ICs

Radiation impinging on an integrated circuit causes three different types of effects [118]:

- Displacement Damage (DD);
- Single Event Effects (SEEs);
- Total Ionizing Dose (TID).

Displacement Damages are caused by non-ionizing energy loss mechanism whereas Single Event Effects and Total Ionizing Dose derive from ionizing energy loss mechanism. The three radiation effects are schematically depicted in Fig. 4.6. Displacement Damage occurs when the incident particle transfers sufficient energy to a lattice atom to dislodge it from its normal location, causing the creation of vacancies and interstitials and introducing energy levels in the bandgap [119]. The displacement damages result in the reduction of recombination lifetime, enhanced thermal generation due to reduction of generation lifetime, reduction of carriers mobility, increase of temporary trapping of majority and minority carriers, and change of majority carrier concentration due to the introduction of centers that compensate the doping [119]. The primary effects are an increase in dark current for any device containing a depletion region, a decrease of charge collection efficiency for silicon detectors, and a decrease gain in bipolar transistors [119, 120]. It has been shown that the electronic property which is most sensitive to displacement damage in irradiated Si and Ge is the recombination lifetime [121, 122].

Single Event Effects occur when the incident particle creates electron-hole pairs in the semiconductor bulk and these charges are collected by an active device, causing

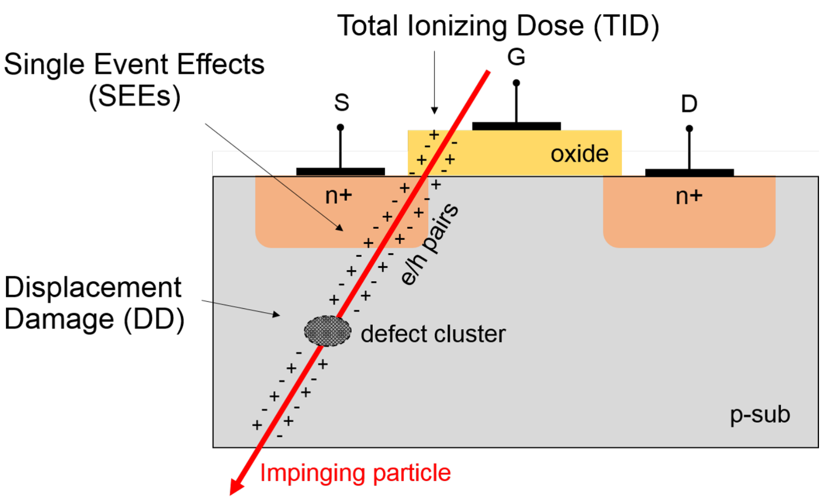

Figure 4.6 – Schematic representation of the three type of radiation effects in a MOSFET.

a dysfunction. The SEEs are divided in soft errors, i.e. faulty operation of a circuit, for example flip of a bit state in memory cells or glitches in logic gates, and hard errors, in which the circuit is permanently damaged, for example due to a latch up [14]. Total Ionizing Dose is another result of ionizing energy loss, in particular of the accumulation of charge in the oxide layers of electronic devices. TID causes a degradation in devices operational parameters, such as, for MOS transistors, a shift in threshold voltage and higher leakage currents [14].

This thesis will focus on SEEs, as they originate from electron-hole pairs generation in the semiconductor substrate. The GLD model will be further extended to simulate radiation-induced excess carriers behavior. Modeling of SEEs is becoming particularly crucial. In fact, recent drastic transistor downscaling, very low operating voltages, and higher complexity made circuits increasingly sensitive to SEEs failures, which became a major source of dysfunction not only in space and at aircraft altitudes but also at ground level [123].

4.3 State-of-the-art of Single Event Effects modeling

Modeling of ionizing radiation effects in semiconductor substrate, and so prediction of SEEs in ICs, involves simulation of the charge generation, transport and collection. Regarding the evaluation of the amount of generated charges in the semiconductor by the incoming particle, i.e. the LET, as explained in the previous section, specific tools based on Monte Carlo simulations are employed. In addition to SRIM, Geant4 [116, 124] MCNPX, MARS15, PHITS [2] are also used. Some tools for prediction of SEEs have been derived with a direct link with these Monte Carlo simulators, embedding them as internal simulators and adding a charge transport model [125]. In these tools, for computational cost reasons, the transport of the radiation-induced charges is often based on a simplified transport model. Refs. [125] and [126] presents a comprehensive review of these tools. One of the most interesting tool is presented in [127, 128, 126] and is called TIARA-G4. It is a full Geant4 application and uses Geant4 classes for the description of the circuit geometry. The incident particle interaction with the circuit and all the secondary particles generated in the entire volume are simulated by Geant4 [126]. Then, TIARA-G4 analyzes all the ionizing particles tracks generated and lists all the traversed sensitive volumes [129]. The parasitic transient currents are evaluated by the tool using an analytical diffusion-collection model. In this model, the energy lost by radiation in the semiconductor is described as a succession of quasi-point charges, whose transport is assumed to be governed by a pure 3D spherical diffusion law [129]. The tool is applied for prediction of SEEs in memory cell: the parasitic currents are evaluated for all sensitive nodes and the collected charge is compared to a critical charge that causes the cell upset [129].

The most common approaches to simulate radiation-induced charges transport and collection in semiconductor devices are numerical simulations with TCAD tools, SPICE simulations using compact models and mixed-mode approach. The full numerical approach with TCAD tools provides the most accurate results but simulation times are very long and only small circuits with few devices can be simulated in this way. Thus, TCAD is widely used for simulations at a single device level and several examples can be found in literature [130, 131, 132, 133, 134, 135, 136, 137, 138, 139]. Numerical simulations provide a complete picture of charge behavior in the device, depending on the device structure, geometry, and technological parameters and they are useful to understand the underlying physics and to carefully optimize the layout at device level. Mixed-mode approach is very popular for accurate simulation of radiation effects in circuits [140, 141, 142, 143, 144, 145]. Mixed-mode consists in simulating numerically, using TCAD tools, only the device struck by the radiation and to model all the others transistors and devices in the circuit using compact models. The parasitic signals resulting from interaction with radiation in the struck device are computed by TCAD and injected in the circuit that is simulated by SPICE software [2]. Simulation times for mixed-mode approach are still long, as a numerical simulation is embedded in the modeling flow, however, the biggest advantage is the enabling of circuit simulation, that is impossible by pure numerical TCAD simulations. The other drawbacks are that mixed-mode simulations are not feasible for very large and complex circuit and they are not accurate if there is a coupling effects involving a device modeled with a compact model [146, 2]. Short simulation times are obtained with SPICE simulations at circuit level, that use compact models and can be applied even to very large architectures. SEEs simulations with SPICE are obtained by modeling the radiation-induced parasitic current and injecting it in the circuit via a current source connected at the struck node [2]. A large number of works can be found in literature, among them [147, 148, 149, 150, 151, 152, 153, 154, 155, 156]. A commonly used expression for the radiation-induced current is the double exponential [140, 2]:

$$I(t) = \frac{Q}{\tau_f - \tau_r}\left(e^{-\frac{t}{\tau_f}} - e^{-\frac{t}{\tau_r}}\right) \tag{4.1}$$

where Q is the total charge deposited, τ_r is the current pulse rising time constant and τ_f is the falling time constant. Typically, rise times are much shorter, in the order of tens of picoseconds, than falling time, that are in the range of 200 to 300 ps [140, 2]. The parameters in Eq. 4.1 are extracted empirically, by fitting experimental data, or derived from numerical simulations. Another approach consists in deriving the collected carrier density n using a spherical diffusion model [157, 158]. However, this model is valid only when the transport of carriers is only by diffusion, i.e. charges are generated far from any junction. Finally, the simulation of charge transport based on parallelized random-walk drift-diffusion process is proposed in [127]. For each simulated ionizing particle impact, radiation-induced charge deposition is first modeled and computed as a succession of charge packets along the particle track, then the transport of each charge packet is computed, independently of the others. This transport is split into two components: the 3D spherical charge carrier diffusion, modeled using a random-walk algorithm, and the electric-field induced drift, due to reverse-biased drain junctions. The model has been dynamically coupled with a SPICE circuit simulator to take into account temporal variations of the electric fields in the charge collection process. Even though this method provides fast simulations at circuit level with higher accuracy with respect to analytical models, there are some limitations: the model is not self-consistent with electrostatics (electrostatic interactions between the charge packets are not taken into account), it is not precise for high injection operation (which is likely to occur for energetic particles), and considers the boundaries of the wells as absorbing boundaries (and so the charge packets are removed from the simulation, which might not be case for all the situations).

The main limitation of the SPICE approaches using compact models is that the precision of the results is strictly linked to the accuracy of the compact models and of the expression used for the parasitic current. The actual value of the latter is very challenging to model precisely (it depends on the type and energy of impinging radiation, device layout and hit location), and analytical equations can only give an approximate estimate [140]. However, SPICE simulations can be very useful when a high accuracy on current magnitude and time profile is not needed to study the circuit dysfunctions and the main requirements are response within short simulation times and avoidance of complex numerical simulation tools. When higher accuracy is needed, parasitic currents obtained by TCAD numerical simulations can be used as an input [140, 2]. Ref. [159], for example, presents a library of parasitic transient currents for the different particle strikes derived from 3D numerical simulation, which can be used for circuit-level soft error estimation.

4.4 Extended Generalized Lumped Devices approach

In this work, the Generalized Lumped Devices (GLD) approach is used to simulate excess carriers generated by ionizing radiation in ICs substrate. With the proposed model it is possible to obtain fast SPICE-compatible simulations with higher accuracy with respect to conventional approaches presented in the previous section. The parasitic current, in fact, will not be obtained analytically, empirically or by using approximated transport models, but it will be computed by the equivalent network of Generalized Devices that describes the semiconductor substrate hit by the radiation. The GLD model, as seen already in Part I, is a physics-based model that simulates excess carriers generation, recombination, propagation and collection in a semiconductor structure using a semi-compact approach, i.e. a lumped network of Generalized Lumped Devices. The model does not need any fitting parameters, as it only employs geometrical and technological parameters related to the semiconductor structure, and does not need any predefined compact model. Still, the objective is not to develop a new "TCAD" tool, but to have a model that can provide the designers with an estimation of the SEEs tolerance of the circuit under development and that can be easily embedded in the design flow in standard circuit simulators.

In Part I, the GLD model has been used for simulation of optically generated excess carriers. The model will now be extended to simulate radiation-induced charges. The generation profiles given by light and ionizing particles are very different, as the peak of generation for radiation is not at the surface and also the generation track goes deeper in the substrate. Because of this, together with the much higher density of radiation generated charges, the mesh strategy will be changed in order to correctly linearize the excess carriers concentrations and gradients. In addition, the generation rate values, as a function of the position in the semiconductor, will be extracted from the available data for ionizing radiation given by the particle-matter simulators, i.e. the LET. This map of generation rate will be used to insert the correct *generation parameter* in the model of each Generalized Devices in the equivalent network of the substrate.

The other main difference between light and radiation is related to the injection level. In fact, while for light, in most of the applications, the semiconductor is in low injection condition, for radiation there is almost always a high injection condition. The Generalized Devices model, presented in section 2.3.1, has already some features that take into account high injection. In particular, there are the correction terms of resistance value depending on the excess carriers concentration, as explained in section 2.3.1, the Boltzmann correction term and the Misawa's space-charge boundary conditions, already included in the original Generalized Devices developed for HVMOSFET [6]. In high injection, in fact, the quasi-Fermi level splitting ΔV_F of a pn junction is not equal to the applied voltage, as for low injection, but an additional correction term has to be considered, i.e. the Boltzmann voltage drop V_r. The following expression is present in the model of the Generalized Diode [6]:

$$V_r = V_t \ln\left(\frac{N_A + \hat{n}_p}{N_A + \hat{n}_1}\right) + V_t \ln\left(\frac{N_D + \hat{p}_n}{N_D + \hat{p}_2}\right) \tag{4.2}$$

where N_A and N_D are the doping concentrations of the p-type and n-type semiconductor, respectively, V_t is the thermal voltage, $\hat{n}_p$ and $\hat{p}_n$ are the excess carriers concentration at the boundaries of the depletion region, and $\hat{n}_1$ and $\hat{p}_2$ are the excess carriers concentration at the external pins of the Generalized Diode, i.e. the geometrical boundaries. Including the Boltzmann correction term in the law of mass action for non-equilibrium ($np = n_i^2 e^{\Delta V_F/V_t}$), new boundary conditions at the edges of depletion region are obtained, i.e. the Misawa's boundary conditions that are valid for all injection levels [160, 6]:

$$\hat{n} = \frac{N_A + n_{p_0}}{2}\left(\sqrt{1 + \frac{4n_i^2\left(e^{\frac{V_j}{V_t}} - 1\right)}{(N_A + n_{p_0})^2}} - 1\right) \tag{4.3}$$

$$\hat{p} = \frac{N_D + p_{n_0}}{2}\left(\sqrt{1 + \frac{4n_i^2\left(e^{\frac{V_j}{V_t}} - 1\right)}{(N_D + p_{n_0})^2}} - 1\right) \tag{4.4}$$

where n_{p_0} is the electron concentration at thermal equilibrium in the p-side, p_{n_0} is the hole concentration at thermal equilibrium in the n-side, and V_j is the voltage drop on the space-charge region. These expressions are substituted to the Shockley boundary conditions in the Generalized Diode model, presented in Eq. 2.33 (section 2.3.1).

In this thesis, other corrections for high injection will be included. The ambipolar transport will be considered and mobility and lifetime values will be changed to the ambipolar values. Finally, the phenomenon of funneling, that arise when excess carriers with density higher than doping are present in proximity of a pn junction, will be studied and inserted in the model of the Generalized Diode. The *plasma* given by high concentration of electron-hole pairs generated by the ion track in the semiconductor drastically distorts the space-charge region of the pn junction it crosses. The highly conductive *plasma* propagates the electric field along its track, inside previously field-free regions. The carriers in the track, accelerated by the electric field, will be collected by drift, a much faster process, rather than by diffusion. When the excess carrier concentration at the junction decreases below the doping, the original space-charge region rebuilds and the electric field turns back to its original value [8, 161].

4.4.1 Radiation-induced generation modeling

Simulation software for particle-matter interaction gives as an output the electronic stopping power, i.e. the LET. The LET of a specific ion, with certain energy, impinging on the target semiconductor is used to derive the generation rate. This is introduced in the MCC of the Generalized Lumped Devices (see section 2.3.1 for details on GLD model). In this work, the LET values, referred to ions impinging on silicon, are taken from a behavioral modeling of SRIM data, presented in [162]. The LET data, as a function of ion energy (E) for a given particle, simulated with SRIM are fitted using power polynomial functions [162]. The LET is modeled as:

$$\mathrm{LET}(E) = 10^{A(E)} \tag{4.5}$$

$$A(E) = \sum_{i=1}^{8} a_i \cdot \sin(b_i \cdot \log_{10}(E) + c_i) \tag{4.6}$$

where the parameters a_i, b_i and c_i, obtained from fitting SRIM simulation results, are tabulated in [162] for several ions (the possible secondary ions produced by the neutron-silicon interaction, i.e. from hydrogen to phosphorus). The same approach is used to obtain the range [162].

In this thesis, the LET as a function of distance traveled by the ion in silicon is derived from the LET as a function of energy in Eq. 4.5. The complete derivation is reported in Appendix A. Then, the generation rate is extracted. The LET is a *point-like* quantity, as it is expressed in pC/μm, but the generation rate (cm$^{-3}/s$) is a *volumic* quantity. Thus, the LET has to be *spread* in the corresponding mesh rectangles. The radiation track is divided in several segments, used to construct the mesh rectangles in that region of the substrate, and the local charge given by the LET is integrated in each segment, giving an equivalent charge density distribution, which is attributed to the mesh rectangles around the track. The generation rate is obtained dividing this charge density by the duration of the radiation pulse[1] Δt. This results in a single line of mesh rectangles with a given generation value, while the rest of the substrate has zero excess carriers generation. The generation rate for a mesh rectangle in the ion track is given by the following expression:

$$G = \mathrm{LET} \cdot \frac{l}{V} \frac{1}{\Delta t} \tag{4.7}$$

where l is the mesh element length and V is its volume.

[1] The generation rate in time is assumed to be a square wave with a single pulse of the duration of Δt in which the generation rate is non-zero

4.4.2 Lifetime and mobility in high injection

When the semiconductor is in high injection condition, i.e. the excess carrier density is higher than the doping, the ambipolar parameters, lifetime and mobility, cannot be approximated to the minority carrier values, as for low injection. The full expressions have to be used. Thus, when modeling radiation-induced excess carriers, whose concentration is almost always higher than the doping, the values used in section 2.3.1 are changed.

The ambipolar diffusion coefficient D_a and the ambipolar mobility μ_a are computed as [3]:

$$D_a = \frac{n+p}{n/D_p + p/D_n} \tag{4.8}$$

$$\mu_a = \frac{n+p}{n/\mu_p + p/\mu_n} \tag{4.9}$$

where D_n and μ_n are the diffusion coefficient and mobility for electrons, D_n and μ_n are the diffusion coefficient and mobility for holes, $n = n_0 + \hat{n}$ is the total electron concentration given by doping plus generated excess carriers $\hat{n}$, and $p = p_0 + \hat{p}$ is the total hole concentration given by doping plus generated excess carriers $\hat{p}$.

Regarding recombination rate R, the general expression, valid for low and high injection, is [3]:

$$R = r_{ec} pn \tag{4.10}$$

where r_{ec} is the recombination coefficient. For low injection, in an n-type semiconductor [3]:

$$R = r_{ec} pn = R_{ec} \hat{p} N_D \equiv \frac{\hat{p}}{\tau_p} \tag{4.11}$$

where the holes lifetime is defined as:

$$\tau_p = \frac{1}{r_{rec} N_D} \tag{4.12}$$

and, similarly for electrons in p-type semiconductor:

$$\tau_n = \frac{1}{r_{rec} N_A} \tag{4.13}$$

For high injection condition, in which $n \simeq \hat{n}$ and $p \simeq \hat{p}$ [3], the recombination rate is:

$$R = r_{ec} pn = r_{ec} \hat{n}^2 = r_{ec} \hat{p}^2 \tag{4.14}$$

and the ambipolar lifetime τ_a is defined as [3]:

$$\tau_a = \frac{1}{r_{rec}\hat{n}} = \frac{1}{r_{rec}\hat{p}} \tag{4.15}$$

However, when the recombination rate depends on $\sim \hat{n}^2$, the solution of the differential equation for diffusion $\frac{d\hat{n}}{dx} \propto \hat{n}^2$ is no more an exponential, as in low injection when $\frac{d\hat{n}}{dx} \propto N_A\hat{n}$ and the solution is $\hat{n} \propto \sim e^{t/\tau}$. Thus, the definition of lifetime in Eq. 4.15 provides an approximate solution for high injection. In Generalizes Lumped Devices approach, the solution of the differential equation is not needed. In fact, the continuity equation is linearized and is solved by the SPICE simulator. In section 2.3.1, the recombination rate has been inserted in the model in its approximate form valid in low injection:

$$R = \hat{u}/\tau \quad \rightarrow \quad R_i = \frac{V_{eq_i}}{\tau} \qquad \text{at the mesh node } i \tag{4.16}$$

For simulation of high injection, the general form is included in the GLD model (valid for both high and low injection), assuming that neutrality hypothesis $\hat{n} = \hat{p} = \hat{u}$ holds:

$$R = r_{ec}pn = r_{ec}(p_0 + \hat{u})(n_0 + \hat{u}) \rightarrow R_i = r_{ec}(p_0 + V_{eq_i})(n_0 + V_{eq_i}) \tag{4.17}$$

where n_0 and p_0 are electron and hole concentration at thermal equilibrium. Following this derivation, the equivalent circuital parameter in the MCC for recombination (G_c, see section 2.3.1 for details) is:

$$G_c = \frac{A_x \Delta x}{d_m} r_{ec}(N + V_{eq}) \tag{4.18}$$

where N is the doping. In MCC, the conductance G_c is multiplied by the equivalent voltage V_{eq} to obtain the equivalent *recombination* current, thus the proportionality to $\hat{u}^2 \propto V_{eq}^2$ is satisfied. The concentration at thermal equilibrium of minority carriers is assumed to be negligible with respect to $\hat{u}$.

4.4.3 Funneling effect

Funneling may occurs when a radiation track crosses a semiconductor pn junction [161, 163, 148, 164, 165, 166, 167]. If electron-hole pairs generated by the radiation in close proximity to the pn junction have a concentration higher than the doping, a plasma is created and the space-charge region around the junction collapses, fading out where generated e-h pairs exceed the doping, as sketched in Fig. 4.7. This plasma behaves like a *wire*, i.e. a highly-conducting region, that extends along the radiation

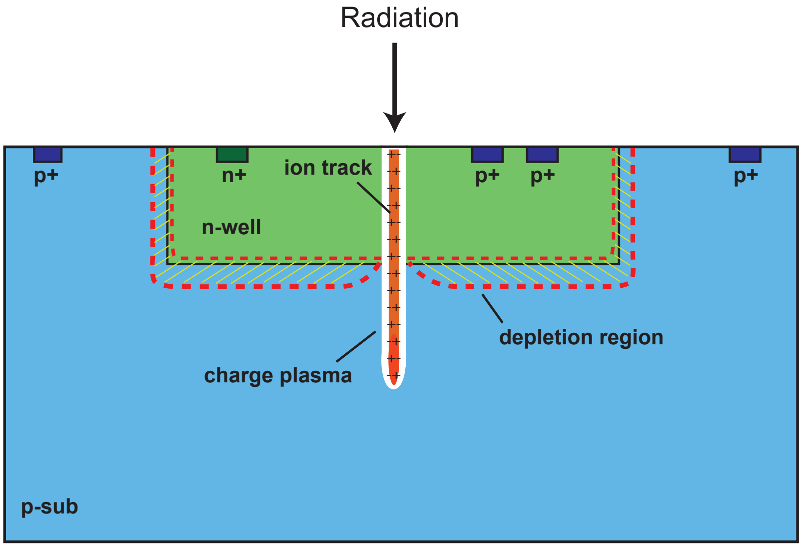

Figure 4.7 – Schematic illustration of the funneling mechanism. The space-charge region collapses as a plasma is generated along the ion track.

track inside the semiconductor. The plasma *wire* has a low resistance, so the potential along the wire is almost constant. Consequently, the electric field, that was initially restricted to the space-charge region, spreads out in semiconductor regions that were previously neutral.

Fig. 4.8 shows the 2D distribution of the potential from TCAD numerical simulation 0.1 ns after the particle event (same structure as in Fig. 4.7). The potential of the n-well now extends along the ion track in the p-substrate since the pn junction barrier disappeared around the track. This *plasma wire*, that shifts the potential of the substrate, acts as a *contact*: the potential decreases almost linearly along the path. Given this electric field generated by the funneling, excess carriers in the track will be *rapidly* collected by drift, until the e-h pairs density at the junction will be lower than the doping, usually after a few nanoseconds (depending on the charges generated, bias voltage and doping). After this delay, the original space-charge region starts to rebuild, as for the potential distribution which drops back into the depletion region. The remaining excess charges are then collected by diffusion.

Funneling drastically changes the collection of charge in the substrate of an IC [167]. Without funneling, the diffusion is the predominant transport mechanism. The excess charges travel slower but farther, which results in parasitic currents at various nodes of the circuit, with low but relatively long current waveforms. In presence of funneling, parasitic currents will be mainly collected by the struck node, resulting in shorter and higher current peaks. SEEs are usually caused by short and high currents, which is the reason why modeling whether or not funneling occurs is crucial for accurate simula-

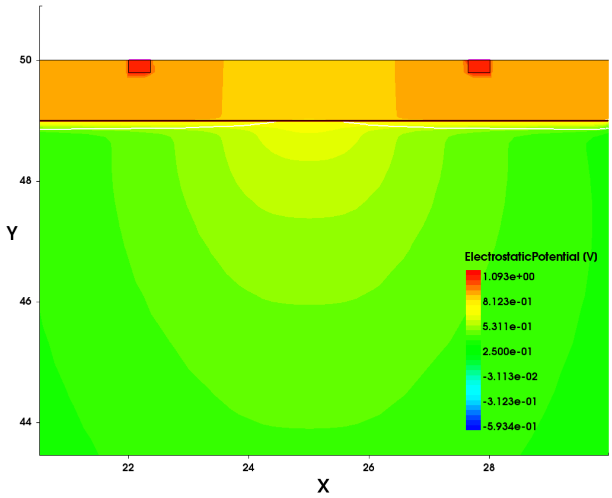

Figure 4.8 – Potential distribution in a 2D structure similar to the one in Fig. 4.7, 0.1 ns after the striking of an ionizing particle. The junction line is shown in brown: the upper part is the n-well and the lower part is the p-type substrate. The funneling effect, with the distortion of the potential in the structure, is evident.

tions. TCAD simulations include this phenomenon, whereas for SPICE simulations it depends on how the radiation induced parasitic current is modeled. Funneling can be taken into account by considering the proper parasitic currents (i.e., when the funneling is active) for the fitting of analytical models [159, 140, 156].

In this work, the funneling effect is included in the Generalized Lumped Devices. In order to simulate funneling as a *connecting wire*, a resistance (R_{funnel}) that connects the two neutral region of the diode is introduced in the TCC sub-circuit. The new model of the Generalized Diode, including the resistance R_{funnel}, is shown in Fig. 4.9. The resistance R_{funnel} has initially a high value ($\sim 10^8\ \Omega$, *open-circuit*), takes a low value ($\sim 10^{-6}\ \Omega$, *short-circuit*)[2] when the funneling is active, i.e. the excess carriers density is higher than the doping, and come back to the high value at the end of the funneling event, i.e. when the excess carriers density is lower than the doping. R_{funnel} is modeled analytically with an hyperbolic tangent function, as shown in Fig. 4.10. In this way, the p-side and the n-side of the diode are connected together and are set at the same potential during the funneling. The diode is also connected to the rest of the network of Generalized Devices, so the potential is also spread inside the substrate depending on the local resistances and currents. Moreover, since the junction barrier collapses, the exponential diode laws in the compact model (V_n, V_p, I_{tot}, C_j) are not valid anymore, and the excess carriers can move freely across the junction. This is obtained by interconnecting with a wire the p-side and n-side of the

[2]These two value have been chosen to obtain convergence in Spectre simulators

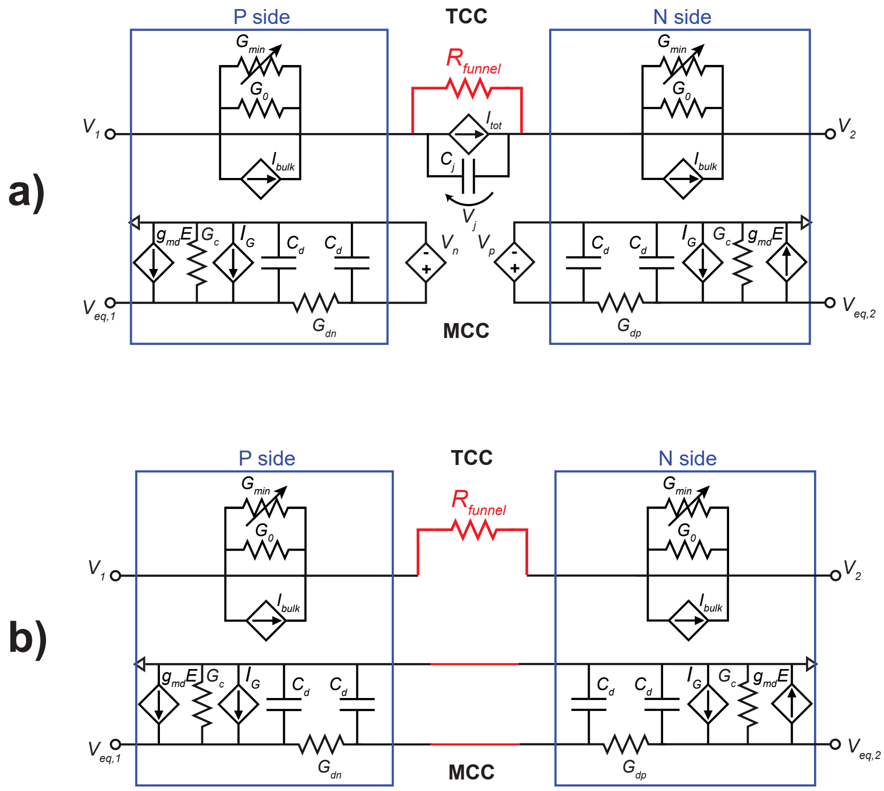

Figure 4.9 – a) Equivalent circuit describing the model of the Generalized Diode before and after the funneling effect. b) Equivalent circuit describing the model of the Generalized Diode during the funneling effect.

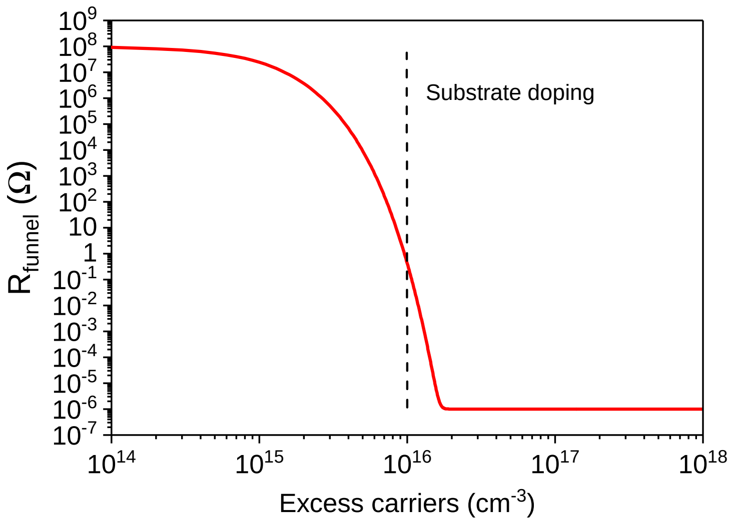

Figure 4.10 – Value of R_{funnel} as a function of excess carriers concentration.

diode (see Fig. 4.9.b) and disabling the sources V_n, V_p, I_{tot} and the capacitance C_j when funneling is active.

4.4.4 Mesh strategy

The mesh strategy presented in Part I, section 2.3.3, is modified to correctly linearize concentrations and gradients for radiation-induced excess carriers. The following steps will be used for meshing of the substrate hit by ionizing radiation, which will be simulated in the next chapter:

1. Mesh lines are placed at every junctions, pn junctions, and homojunctions. A mesh element contains a piece of semiconductor with same doping concentration and type.

2. The mesh is refined so that the maximum size is one fifth of the diffusion length of the minority carriers.

3. The mesh is further refined along the ion track. In the direction of the impinging particle, mesh elements are placed in order to linearize the LET profile. The width of the mesh elements in which generation takes place is 0.2 μm. As explained above, generation is non-zero only in one column of mesh element around the ion track, in which the point-like generated charge given by the LET is *spread* to obtain an equivalent volumic generation rate. In the radial direction, i.e. around the track, 5 mesh elements with a width of 0.2 μm are positioned on each side to linearize the gradient.

Simulations with GLD approach are about 500 times faster than TCAD simulation, for the same structure and using the same hardware. When funneling is active, there are some convergence difficulties with the software program used for SPICE simulations, i.e. Spectre, and as a consequence the simulations are slower, while TCAD simulation times are the same. In this case the SPICE simulations with GLD model are about 100 times faster than TCAD simulations.

4.5 Conclusion

The Generalized Lumped Devices approach has been extended to simulate excess carriers generated in the semiconductor by ionizing radiation. In particular, the model has been modified to support high injection condition. Furthermore, the funneling effect, which is a phenomenon happening when the concentration of excess carriers in proximity of a pn junction is higher than the doping concentration, has been included in the model of the Generalized Devices.

5 Simulation of radiation-induced currents in ICs substrate

The extended Generalized Lumped Devices (GLD) model is now applied to simulate effects of radiation strike on the substrate of ICs. The objective is to understand if this model can be employed to predict Single Event Effects using SPICE simulators, with a higher accuracy with respect to standard compact models for radiation-induced currents. Excess carriers generated by the impinging particle, according to the LET of the particle in the specific target material (silicon will be always considered), are simulated. Their generation, propagation and collection are taken into account by the Minority Carrier Circuit (MCC) of the Generalized Lumped Devices that, thanks to the coupling with the Total Circuit Currents (TCC), computes the resulting current at sensitive nodes. The main objective is to have a fast, but still accurate, tool that can be used by designers directly in standard circuit simulators to have an estimation of how the circuit behave when subjected to ionizing radiation and to predict if an error, such as memory bit flipping, can arise, according to the circuit layout. The simulation presented in this chapter are a preliminary step toward this result. TCAD Sentaurus simulations will be used to assess the validity of the model. The same geometrical and technological parameters of the semiconductor structure are used in TCAD and GLD simulations, so no fitting parameters are inserted in the model. The GLD network is simulated using Spectre circuit simulator.

The main source of Single Event Effects at the ground level are the secondary particles generated by the interaction of neutrons with silicon substrate. Alpha particles are one of the most probable secondary product of this interaction, as reported in Fig. 4.4. Moreover, alpha particles emitted by radioactive impurities (uranium and thorium) in materials of electronic devices packaging are known to be another important contribution to soft errors [2]. For these reasons, alpha particles will be used as radiation source.

5.1 Impact of radiation position and energy on parasitic current

The results presented in this section are based on the published paper [168]. The first structure under test is presented in Fig. 5.1 and represents a region of an IC substrate with n^+-type implants having a depth of 200 nm, a width of 0.36 μm (equal to twice the minimum feature size, considering a 180 nm CMOS technology) and doped at 10^{20} cm^{-3}, whereas the p-substrate has a doping of 10^{17} cm^{-3}, a depth of 100 μm and a width[1] of 50 μm. These implantations could represent the source and the drain of MOSFETs for instance. The structure is described with the network of Generalized Lumped Devices following the mesh strategy presented in section 4.4.4.

Fig. 5.3 reports the results of the simulation with the GLD model and of TCAD simulations, run to validate the model. The current is collected by the n^+ implants located at a given distance d (see Fig. 5.1) from the alpha particle track. The alpha particle, with an energy of 2 MeV, strikes the substrate at time $t = 10$ ns. The generation rate is extracted from the alpha particle LET profile as a function of penetration depth, computed according to the method presented in Appendix A and reported in Fig. 5.2. In the GLD model, the radiation-induced generation pulse width is equal to 1 ns (the generation profile is a square wave with a single pulse). In TCAD simulations, the

[1] It is a 2D structure with a lateral extension of 1 μm.

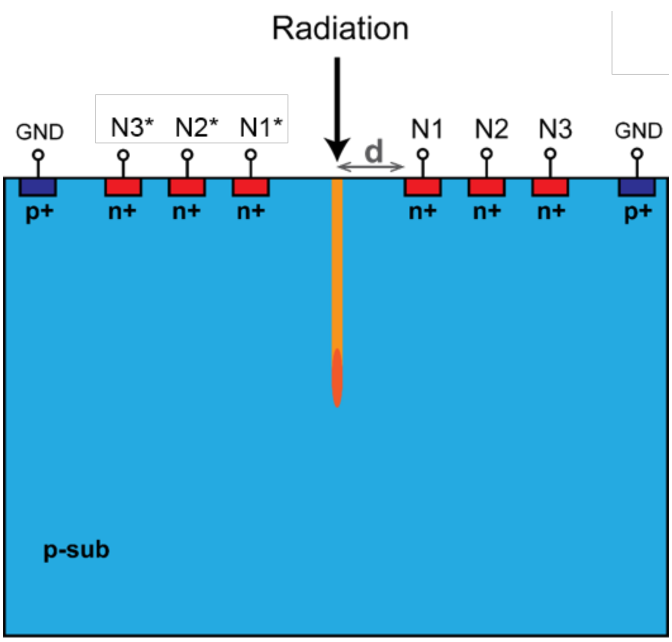

Figure 5.1 – Structure under test. In orange, the alpha particle track inside silicon (the Bragg peak is in dark orange).

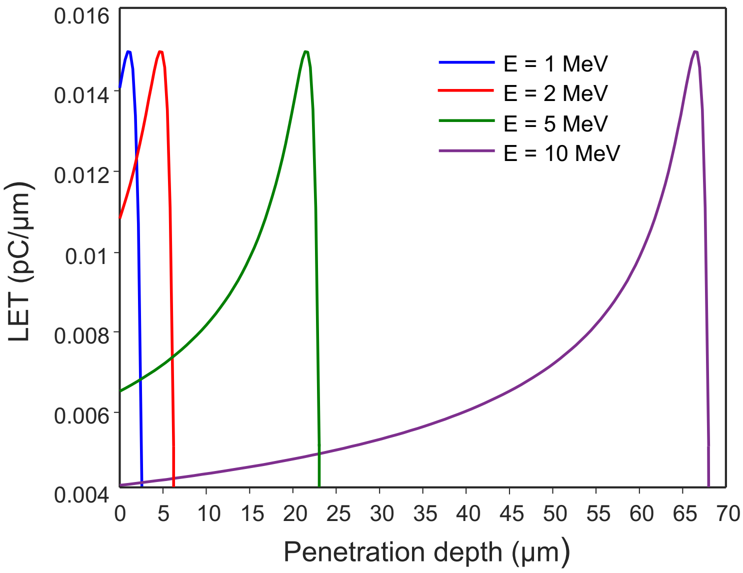

Figure 5.2 – LET as a function of penetration depth of alpha particles in silicon.

generation profile has a Gaussian shape with a standard deviation of $\sigma = 2$ ps. The currents predicted by the GLD model (solid lines) are in good agreement with TCAD simulations (dots).

Fig. 5.4, Fig. 5.5, Fig. 5.6 and 5.7 report parasitic currents induced by alpha particles

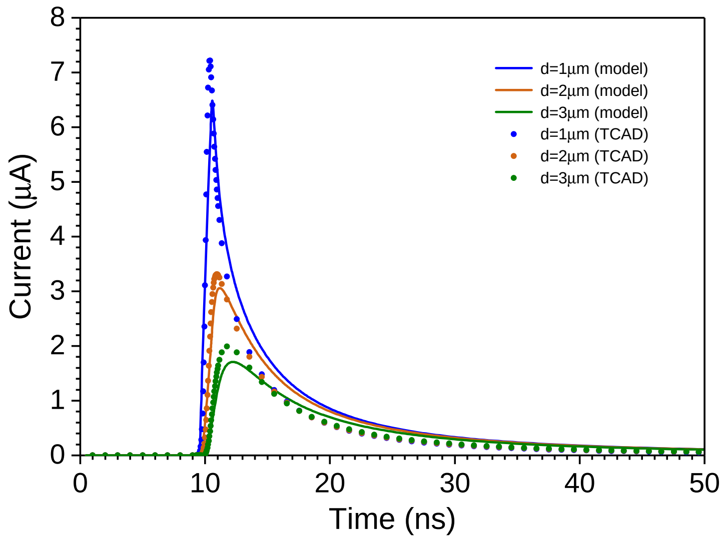

Figure 5.3 – Parasitic currents induced by a 2 MeV alpha particle in an n^+ well with distance d from the particle track. Results with GLD model are reported with solid lines whereas TCAD simulations with dots.

with energy of 1 MeV, 2 MeV, 5 MeV and 10 MeV, respectively, collected by the three n^+ wells N1, N2, N3 of the structure in Fig. 5.1. The distance between N1 and the alpha particle track is equal to 2 μm and each well has a distance of 5 μm from the

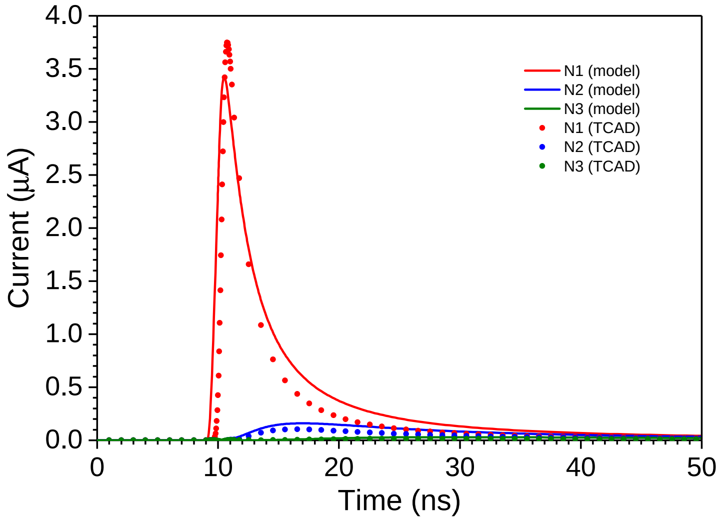

Figure 5.4 – Parasitic currents induced by an alpha particle with an energy of 1 MeV in the three n^+ wells (structure in Fig. 5.1, d = 2 μm, each well has a distance of 5 μm from the adjacent well). Results with GLD model are reported with solid lines whereas TCAD simulations with dots.

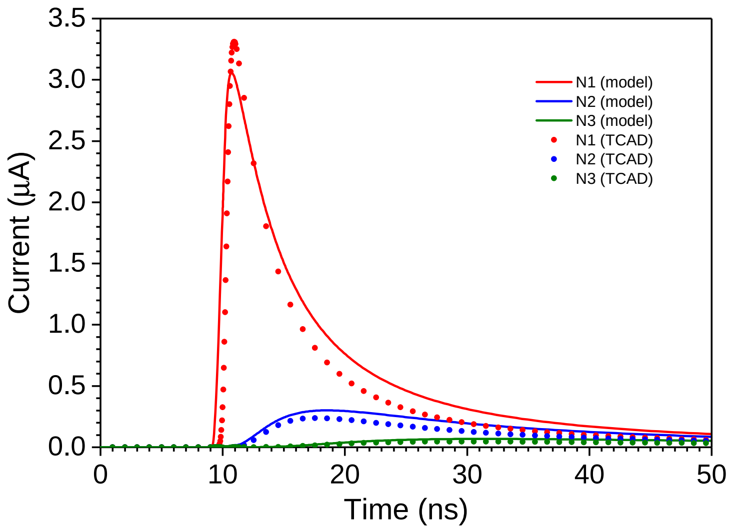

Figure 5.5 – Parasitic currents induced by an alpha particle with an energy of 2 MeV in the three n^+ wells (structure in Fig. 5.1, d = 2 μm, each well has a distance of 5 μm from the adjacent well). Results with GLD model are reported with solid lines whereas TCAD simulations with dots.

adjacent well. Plots refer only to the wells N1, N2 and N3 since the currents on the wells N1*, N2* and N3* are equal to those reported by reasons of symmetry. The results obtained with the GLD model, plotted with solid lines, are in good agreement with

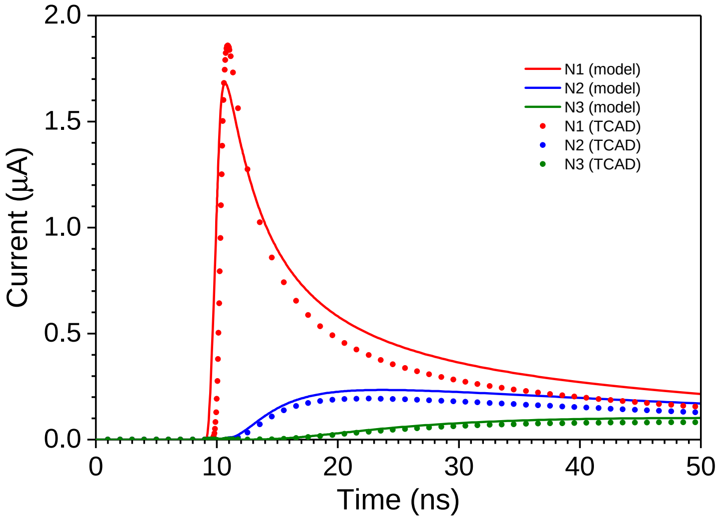

Figure 5.6 – Parasitic currents induced by an alpha particle with an energy of 5 MeV in the three n^+ wells (structure in Fig. 5.1, d = 2 μm, each well has a distance of 5 μm from the adjacent well). Results with GLD model are reported with solid lines whereas TCAD simulations with dots.

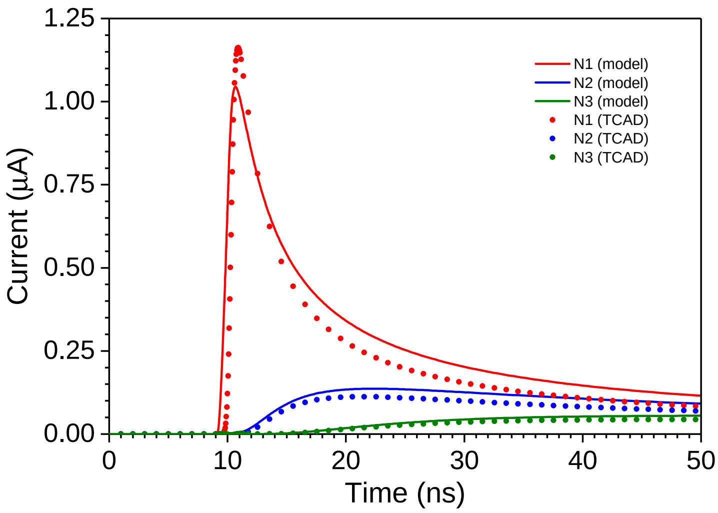

Figure 5.7 – Parasitic currents induced by an alpha particle with an energy of 10 MeV in the three n^+ wells (structure in Fig. 5.1, d = 2 μm, each well has a distance of 5 μm from the adjacent well). Results with GLD model are reported with solid lines whereas TCAD simulations with dots.

TCAD simulations results (dots). Increasing the particle impinging energy, the current peak decreases, even though the total generated charge in the silicon is increased: as can be seen in Fig. 5.2, the integral of the LET for the alpha particle energy of 10 MeV is the highest. The initial energy influences the position of the Bragg peak, where the highest energy is released. In fact, greater alpha particle energies correspond to a deeper Bragg peak, see Fig. 5.2, meaning that lower energy is released near the surface. This is reflected on the peak current decrease with increasing impinging energy since the n^+ wells are only 200 nm deep. In addition, charges generated deeper in the substrate have more time to diffuse further from the particle track, meaning that they can be collected by the wells that are more distant from the track. Conversely, charges generated near the surface are mainly collected by the closer well (N1). In fact, for the alpha particle at 5 MeV, the currents induced on N2 and N3 are higher (relatively to the signal on N1) than in the case of 1 MeV and 2 MeV energies. Moreover, for charges generated quite deep in the substrate (high alpha particles energy), the time required to diffuse to the implants is so high that many more e-h pairs will be recombined. The total current collected by all of the wells will thus be lower for high energy alpha particles, a counter intuitive picture. These fine points are well captured by the GLD model that is in agreement with TCAD simulations for all the range of alpha particle energy.

The substrate doping used in these simulation is quite high ($p = 10^{17}$ cm^{-3}). This value was selected to study a high injection scenario for which the excess carriers concentration is in the same order of magnitude of the doping concentration. In this

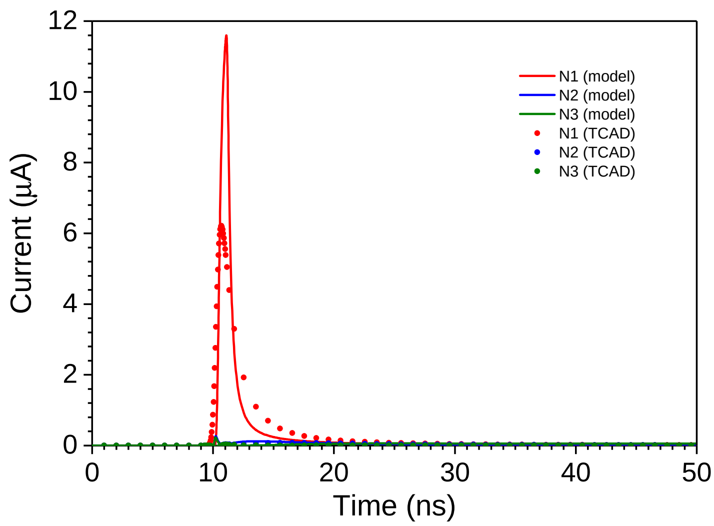

Figure 5.8 – Parasitic currents induced by an alpha particle with an energy of 1 MeV in the three n^+ wells in the structure in Fig. 5.1 with a substrate doping of $p = 10^{16}$ cm^{-3}. Results with GLD model are reported with solid lines whereas TCAD simulations with dots.

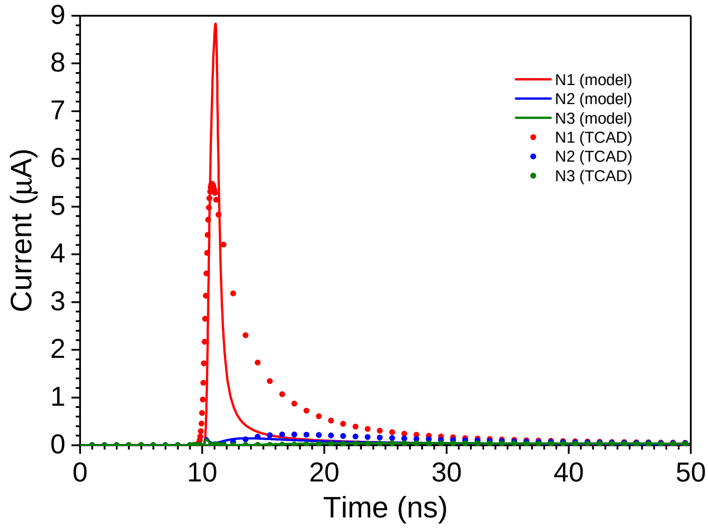

Figure 5.9 – Parasitic currents induced by an alpha particle with an energy of 2 MeV in the three n^+ wells in the structure in Fig. 5.1 with a substrate doping of $p = 10^{16}$ cm^{-3}. Results with GLD model are reported with solid lines whereas TCAD simulations with dots.

case, the model can correctly predict radiation-induced excess carriers generation, propagation and collection without using fitting parameters. Further, the model is assessed for *very* high injection level, i.e. excess electron-hole pairs density is one order of magnitude higher than doping concentration. The substrate doping of the

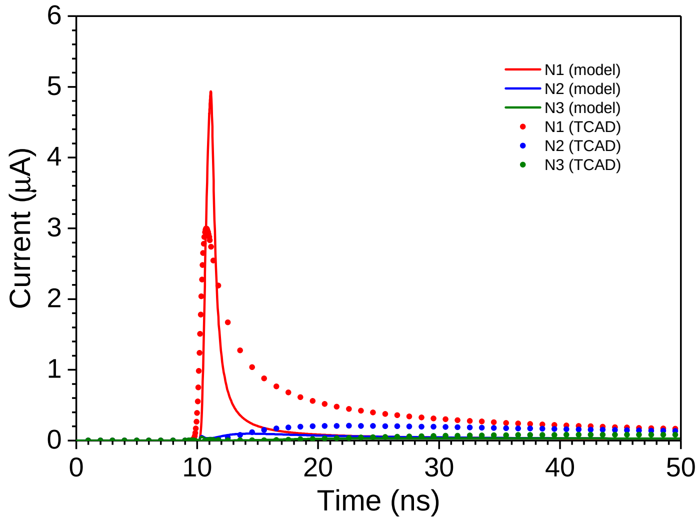

Figure 5.10 – Parasitic currents induced by an alpha particle with an energy of 5 MeV in the three n^+ wells in the structure in Fig. 5.1 with a substrate doping of $p = 10^{16}$ cm^{-3}. Results with GLD model are reported with solid lines whereas TCAD simulations with dots.

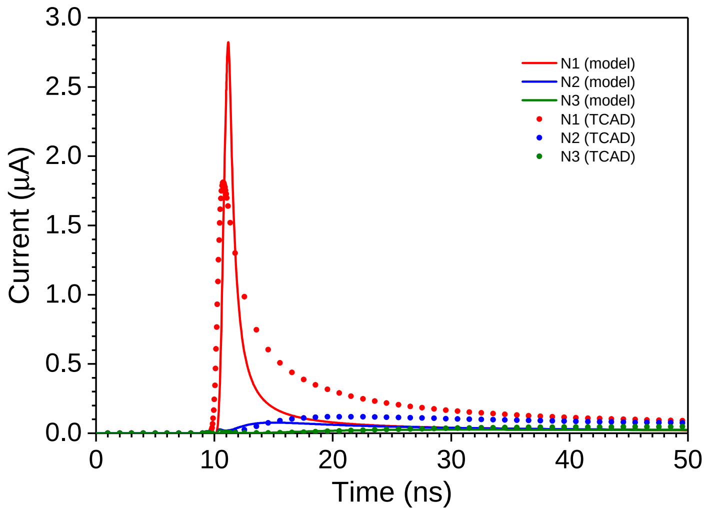

Figure 5.11 – Parasitic currents induced by an alpha particle with an energy of 10 MeV in the three n^+ wells in the structure in Fig. 5.1 with a substrate doping of $p = 10^{16}$ cm^{-3}. Results with GLD model are reported with solid lines whereas TCAD simulations with dots.

structure in Fig. 5.1 is set to $p = 10^{16}$ cm^{-3} and simulations are run again, considering the same alpha particles energies. Parasitic currents collected at the nodes, simulated with GLD model and TCAD simulations, are reported in Fig. 5.8, Fig. 5.9, Fig. 5.10 and Fig. 5.11. Results show that the accuracy of the model is degraded with such high levels of injection. The current peak is overestimated whereas the curve goes to zero too rapidly with respect to TCAD simulations. The GLD approach should be further improved for high injection modeling to obtain a better match. However, for prediction of circuit dysfunctions these results are still acceptable, as the information required to determine if an error occurs is mainly the order of magnitude of the parasitic current. For injection levels even higher, with $p = 10^{15}$ cm^{-3}, meaning that excess charge density is two orders of magnitude higher than the doping, the circuit simulator used for the network of GLD, i.e. Spectre circuit simulator, cannot find a solution due to convergence problems. Convergence issues are the main limitation of this approach for radiation-induced excess carriers modeling and need to be addressed in the future to obtain a complete and reliable tool.

5.2 Simulation of funneling effect

In this section, the funneling effect is studied using the GLD model. The simulated structure is reported in Fig. 5.12. The p-substrate has a doping of $p = 10^{16}$ cm^{-3}, the n-well has a doping of $n = 10^{17}$ cm^{-3}, the highly-doped implants for Ohmic contacts have a doping of $p^+/n^+ = 10^{20}$ cm^{-3}. The p-substrate is 100 μm thick, the n-well has a

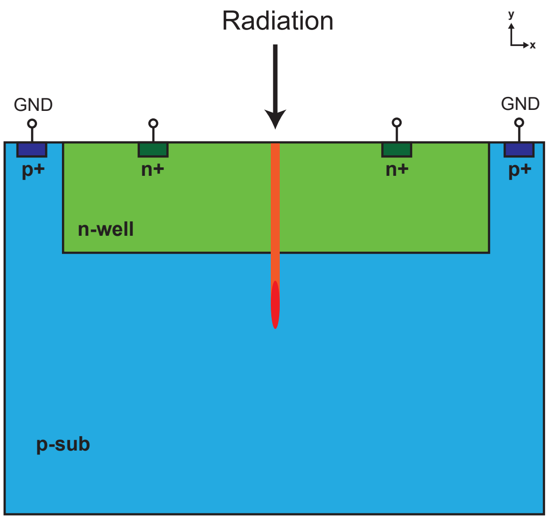

Figure 5.12 – Scheme of the simulated structure: PMOS substrate.

depth of 1 μm and a width of 10 μm, and the p^+/n^+ implants have a depth of 200 nm and a width of 0.36 μm. The lateral extension of these 2D cross sections is 1 μm (all quantities are constant along the third dimension and the cross section is the same).

The structure is hit by an alpha particle with an energy of 5 MeV: the ion track in silicon crosses the pn junction, as the particle travels for 25 μm inside silicon, see Fig. 5.2. Moreover, the excess carrier concentration generated by the alpha particle at the junction is higher than the doping: funneling is triggered. The structure in Fig. 5.12 is meshed and the network of GLD is obtained by connecting each mesh node with the proper Generalized Device. A sketch of the mesh and network of Generalized Devices is shown in Fig. 5.13. The mesh around the radiation track is much finer than in the rest of the structure in order to linearize the LET profile and excess carriers concentration and gradient, as explained in section 4.4.4 (GLD network in Fig. 5.13 is only representative).

The results obtained with the Generalized Devices approach are compared with TCAD numerical simulations to validate the model of the funneling, inserted in the Generalized Diode. The same geometrical and technological parameters have been used in the TCAD simulations and in the GLD network.

Fig. 5.14 reports the simulated current collected by the structure (the pn junction is in reverse-bias, radiation impinging at time t = 0). Simulations with the GLD network and TCAD are reported by solid lines and dots, respectively. The general trend of the current, especially the time scale in which the current goes back to the initial value, is well predicted by the GLD model. However, the model is not very accurate in the estimation of the current peak when the funneling is active. Still, this accuracy

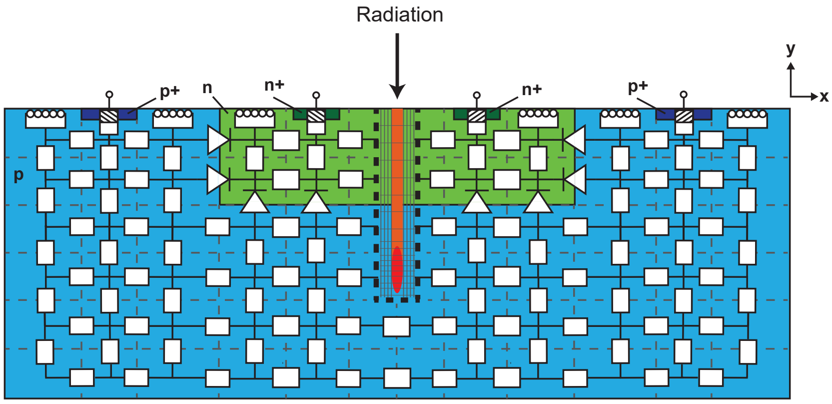

Figure 5.13 – Generalized Devices network obtained for the structure in Fig. 5.12. The mesh is drawn in gray dashed lines. The network is not shown around the radiation track, only the mesh is reported, which is more dense to linearize the generation profile and excess carrier gradients.

is acceptable for the purpose of simulating circuit disturbances, that is the main objective of this approach.

The current induced by the 5 MeV alpha particle, when funneling is active, reaches a higher peak with respect to the currents induced by the same particle when it does not cross a pn junction, i.e. as in the previous section. In fact, when the funneling is not present the current peak is around 2 - 3 μA (see Fig. 5.6 and Fig. 5.10), one order

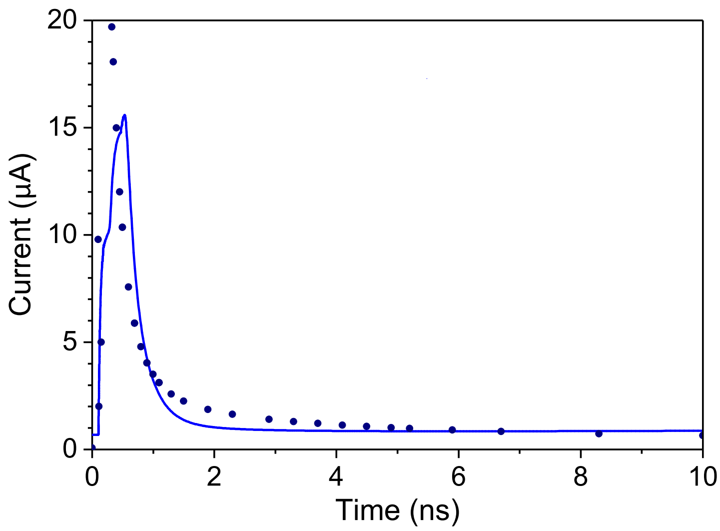

Figure 5.14 – Radiation induced current as a function of time (radiation impinging at t = 0): 5 MeV alpha particle impinging on the structure in Fig. 5.12. The funneling occurs. Results obtained with the GLD network are plotted in solid line. Dots are used for TCAD.

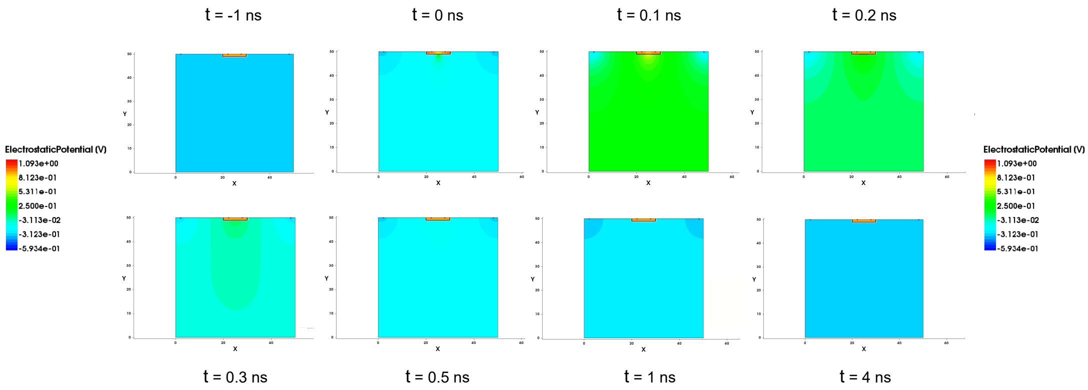

Figure 5.15 – 2D potential distribution in the structure of Fig. 5.12 after the strike of a 5 MeV alpha particle at t = 0 ns.

of magnitude lower than the current peak when the funneling is active (Fig. 5.14). Moreover, the *funneling current* decays much faster (less than 1 ns) than the *non-funneling current* (more than 30 ns). Funneling changes drastically the excess carriers transport and collection and modifies significantly the electric field in the structure, as explained in section 4.4.3. Fig. 5.15 shows the 2D potential distribution in the simulated structure (TCAD numerical simulations) at different points in time. After the radiation strike, funneling occurs, the space-charge region collapses, and the potential quickly spreads into the substrate. The electrostatics in the substrate is deeply affected during the first 0.2 ns. Then, the generated e-h pairs density becomes smaller than the doping and the potential distribution reverts to the initial value. The potential comes back to *pre-radiation* levels after about 4 ns, but the space-charge region is restored already after 0.5 ns.

The pn junction is located at a depth of 1 μm in the substrate. Thus, also 1 MeV and 2 MeV could have been used to simulate funneling effect, as their range is around 2 μm and 6 μm, respectively (see Fig. 5.2). In these cases, the Bragg peak, i.e. maximum of generation profile, is closer to the junction. Higher density of excess carriers are generated at the junction. Simulations, run with the GLD model in Spectre circuit simulator, for alpha particle energies of 1 MeV and 2 MeV do not reach convergence. Further simulations have shown that convergence is more difficult to obtain if electron-hole pairs generated in proximity to the junction have a density one order of magnitude higher than the p-substrate doping. As stated above, convergence issues in very high injection are the main limitation for the application of the proposed approach to high energy particle simulations and further improvements needs to be done in this direction.

5.3 Conclusion

The Generalized Devices modeling approach has been employed to simulate the effect of ionizing radiation in ICs substrate. Simulation of parasitic currents caused by alpha particles strike have been presented and the impact of the particles energy and hitting position has been studied using the Generalized Device model. Finally, the model was used to simulate the funneling effect, triggered by an alpha particle crossing the pn junction between an n-well and the p-substrate.

6 Conclusion

A novel SPICE-compatible approach for simulation of excess carriers was discussed in this thesis. The Generalized Lumped Devices model, previously developed for simulation of minority carrier parasitic substrate currents in HVMOSFET ICs, was here extended to simulate excess carriers generated in semiconductor structures. Excess carriers generated by light and radiation were considered and the model was adapted for these two different cases. The approach developed in this work provides fast and accurate simulations that can be performed using standard circuit simulators. The model is based on a semi-compact approach, in which the semiconductor structure is described with an equivalent network of Generalized Devices. The Generalized Resistance models a piece of semiconductor with constant doping, the Generalized Homojunction models the doping discontinuities present at electrical contacts, the Generalized Diode models the pn junctions, and the Surface Recombination Elements models recombination at surface. This equivalent network simulates excess carriers generation, recombination and transport by drift-diffusion with standard circuit simulators through the definition of equivalent voltages, proportional to the excess carrier concentrations, and equivalent currents, proportional to the excess carrier gradients. The Generalized Devices internal model was obtained by discretizing drift-diffusion and continuity equations. The model is physics-based and does not need any fitting parameters nor predefined compact models: it is independent of the device geometry and layout. The Generalized Lumped Devices models were coded in Verilog-A and simulations were performed using Spectre circuit simulators. Since the model is SPICE compatible, it can be directly interconnected with compact models describing circuital elements, such as transistors, resistors, capacitors, etc., to co-simulate the semiconductor substrate, in which generation takes place, and any external circuit. Thanks to these features, the Generalized Lumped Devices model allows to study the impact of layout, geometrical and technological parameters on the circuit output signals.

The long-term goal of this approach is to have a tool that can be easily used by circuit designers for rapid prototyping and optimization of optoelectronic devices and radiation-hard circuits. This thesis presents a first step towards this objective. The capability of the developed model to predict different scenarios was assessed.

Firstly, simulations of various optoelectronic devices were performed. In particular, the complete I-V characteristic of a solar cell, including the open-circuit voltage and short-circuit current, as well as the transient response of a photodiode were accurately predicted. Then, optically-triggered current amplification was simulated in bipolar phototransistors. Then, a full 3T-APS CMOS image sensor pixel was simulated, including both the photodiode and the in-pixel circuit in a single run. Crosstalk among adjacent pixels was also studied. TCAD simulations (Synopsys Sentaurus Device simulator) were used to validate the models, using the same geometrical and technological parameters, i.e. without introducing fitting parameters in the model. Results confirms that the Generalized Lumped Devices model is suitable to evaluate performances of optoelectronic devices both in DC and transient operation. The relative error with respect to TCAD is in the range of 1%-9% for photodiodes in low injection, whereas it is about 15% for phototransistors and photodiodes in high injection. Simulation times are three orders of magnitude faster than the corresponding TCAD simulations, using the same hardware. Accuracy in optoelectronics simulations is higher than what it was expected since ~ 20% accuracy was set as objective, which would have been enough for a fast pre-optimization to be run in standard circuit simulators. However, even faster simulations can be obtained by decreasing the mesh size, if a lower accuracy is acceptable. Moreover, the model can simulate fine aspects of excess carriers behavior in semiconductors and can thus be used to analyze optoelectronic devices at physics level.

Next, the Generalized Lumped Device approach was assessed for the simulation of radiation-induced excess carriers in ICs substrate. The parasitic current, induced by an alpha particle striking on a p-type substrate and collected by various n^+ wells (source/drain of NMOS transistors) was simulated. The impact of alpha particle energy and position on the parasitic current was studied. Again, TCAD simulations with the same geometrical and technological parameters were run for model validation. The Generalized Devices model could predict quite accurately the parasitic currents, even though with a higher relative error with respect to the previous cases of optoelectronic devices. However, the accuracy obtained is high enough to predict whether the circuit will have a dysfunction or not, which is the main scope of the approach. The main limitation comes from convergence difficulties in very high injection. In fact, simulating the Generalized Devices using Spectre circuit simulator, when the generated excess carriers have a concentration about two order of magnitude higher than the doping, does not reach convergence. Finally, funneling effect was simulated for an alpha particle track crossing the pn junction between an n-well and a p-substrate. The collapse of the space-charge region, the distortion of the electric field in the structure and the consequent parasitic current were predicted quite accurately by the model. Also in this case, convergence issues arose above a certain threshold of excess carriers concentration.

6.1 Future work

This thesis demonstrates that the approach based on the Generalized Lumped Devices can be employed for fast SPICE simulations of optoelectronic devices and for prediction of radiation-induced parasitic currents in ICs substrate using standard circuit simulators. Several further improvements could be implemented to obtain a comprehensive and ready-to-use tool:

- **Full 3D meshing tool:**
  Simulations in Chapter 3 and Chapter 5 were performed on 2D structure (all quantities were constant in the third direction). The model supports 3D simulations, as explained in section 2.3.1 and as demonstrated for HVMOSFET ICs in [6]. What is missing is a software program to generate the mesh of the structure in 3D, including the mesh refinement needed for linearization of light and radiation generation profiles, presented in section 2.3.3 and section 4.4.4. A program to generate the mesh was developed in this thesis, using MATLAB, only for 2D structures.

- **Convergence improvement:**
  For very high injection levels (excess carriers density about one-two orders of magnitude higher than the doping, depending on the application) Spectre circuit simulator (version 10.1.1) cannot simulate the network of Generalized Lumped Devices due to convergence problems. A different circuit simulator, or a different Spectre release, could be used to solve this issue. Alternatively, the Generalized Lumped Devices model could be modified to improve convergence.

- **Displacement Damage modeling:**
  Displacement Damage could be included in the model. The substrate region in which it occurs should be identified and properly meshed. Semiconductor parameters in those mesh elements should be changed, according to the Displacement Damage. Typically, recombination lifetime and carrier mobility will be lower, whereas thermal generation will be higher. Other effects could include temporary trapping of carriers and change of majority carrier concentration due to the introduction of centers that compensate the doping.

- **Different substrate materials:**
  In this work, only silicon was considered as substrate material. Other mate-

rials could be simulated by changing the semiconductor parameters in the Generalized Devices model.

- **Pinned Photodiode:**
  In Chapter 3, simulations of a CMOS image sensor pixel were presented. A 3T-APS was selected. Another widely used pixel architecture is the 4T-APS, which employs a pinned photodiode. The model could be extended to predict the behavior of the pinned photodiode in order to simulate a 4T-APS pixel.

A Appendix

Derivation of LET as a function of distance traveled by the particle in the semiconductor

The LET is usually obtained from particle-matter interaction software. They give as a result the electronic stopping power, i.e. the LET, as a function of impinging particle energy. In this thesis, The LET as a function of distance traveled by the particle in the semiconductor is needed, so to perform a mapping of the generation of excess carriers in every position of the semiconductor structure.

The LET is defined as:

$$\mathrm{LET}(E) = \frac{dE}{dx} \tag{A.1}$$

where E is the energy of the particle and x is the distance traveled by the particle in the semiconductor (x-axis is defined along the particle track, in the same direction). Thus:

$$dx = \frac{dE}{\mathrm{LET}(E)} \tag{A.2}$$

and by integrating dx:

$$x = \int_{x_i}^{x_f} dx = \int_{E_i}^{E_f} \frac{dE}{\mathrm{LET}(E)} \tag{A.3}$$

the distance traveled by the particle as a function of the energy lost $E_f - E_i$ is obtained. The range, which is the distance at which the particle has lost all its energy and it stops, can be computed by integrating between the initial energy with which the particle hits the surface of the semiconductor ($x_i = 0$) and the final energy at which it stops, i.e. $E_f = 0$. The integral is done numerically using MATLAB. Thus, the range as a function of the energy is found, and so it is possible to obtain the energy as a function of distance:

$$x = f(E) \rightarrow E = f^{-1}(x) \tag{A.4}$$

From Eq. A.1:

$$\text{LET} = \frac{dE(x)}{dx} = \text{LET}(x) \tag{A.5}$$

After performing the derivative, numerically with MATLAB, the LET as a function of distance is found.

An example of LET as a function of distance obtained by applying the above method to the LET as a function of energy extracted from the behavioral modeling of SRIM data presented in [162] is reported in Fig. A.1. Results for different impinging energy of Mg ions hitting on silicon are shown.

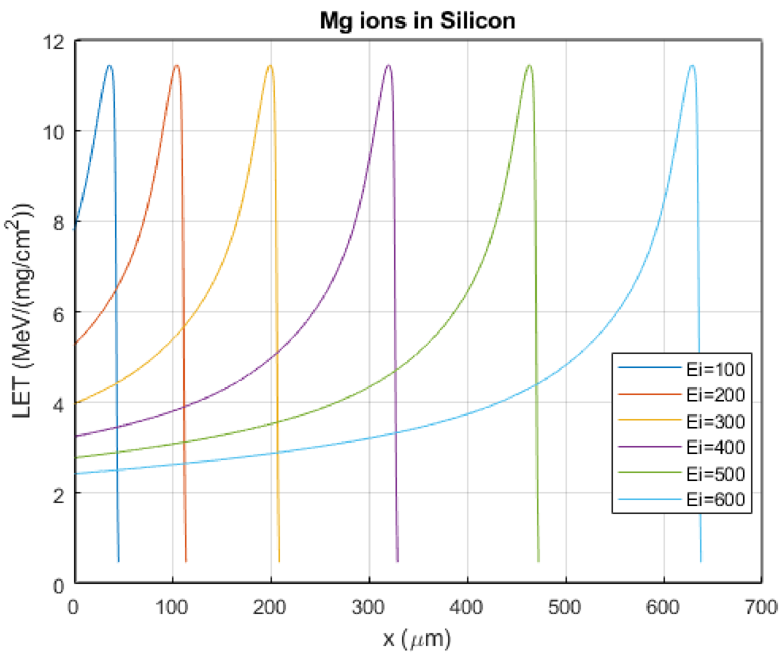

Figure A.1 – LET as a function of traveled distance for Mg ions with different initial energies impinging on silicon.

Bibliography

[1] L. Nagel, “The history of SPICE.,” in *IEEE SISPAD 2013 CEDA Workshop*.

[2] J.-L. Autran and D. Munteanu, *Soft Errors: From Particles to Circuits.* CRC Press, 2015.

[3] S. M. Sze, *Physics of Semiconductor Devices.* John Wiley & Sons, 3nd ed., 1981.

[4] T. Ma, H. Yang, and L. Lu, “Solar photovoltaic system modeling and performance prediction,” *Renewable and Sustainable Energy Reviews*, vol. 36, pp. 304–315, 2014.

[5] D. Giaffreda, P. Magnone, M. Meneghini, M. Barbato, G. Meneghesso, E. Zanoni, E. Sangiorgi, and C. Fiegna, “Local Shunting in Multicrystalline Silicon Solar Cells: Distributed Electrical Simulations and Experiments,” *IEEE Journal of Photovoltaics*, vol. 4, no. 1, pp. 40–47, 2014.

[6] C. Stefanucci, *Substrate modeling of parasitic couplings in Smart Power ICs with generalized lumped devices.* PhD thesis, École polytechnique fédérale de Lausanne (EPFL), 2016.

[7] J. F. Ziegler, “Terrestrial cosmic ray intensities,” *IBM Journal of Research and Development*, vol. 42, no. 1, pp. 117–140, 1998.

[8] C. Vial, J. M. Palau, J. Gasiot, M. C. Calvet, and S. Fourtine, “A new approach for the prediction of the neutron-induced SEU rate,” *IEEE Transactions on Nuclear Science*, vol. 45, no. 6, pp. 2915–2920, 1998.

[9] J. F. Ziegler and W. A. Lanford, “The effect of sea level cosmic rays on electronic devices,” *Journal of Applied Physics*, vol. 52, no. 6, pp. 4305–4312, 1981.

[10] R. C. Baumann, “Radiation-Induced Soft Errors in Advanced Semiconductor Technologies,” *IEEE Transactions on Device and Materials Reliability*, vol. 5, no. 3, pp. 305–316, 2005.

[11] D. M. Fleetwood, P. S. Winokur, and P. E. Dodd, "An overview of radiation effects on electronics in the space telecommunications environment," *Microelectronics Reliability*, vol. 40, pp. 17–26, 2000.

[12] E. Normand, "Single-event effects in avionics," *IEEE Transactions on Nuclear Science*, vol. 43, no. 2 PART 1, pp. 461–474, 1996.

[13] S. Duzellier, "Radiation effects on electronic devices in space," *Aerospace Science and Technology*, vol. 9, no. 1, pp. 93–99, 2005.

[14] P. E. Dodd, M. R. Shaneyfelt, J. R. Schwank, and J. A. Felix, "Current and Future Challenges in Radiation Effects on CMOS Electronics," *IEEE Transactions on Nuclear Science*, vol. 57, no. 4, pp. 1747–1763, 2010.

[15] H. Kobayashi, N. Kawamoto, J. Kase, and K. Shiraish, "Alpha Particle and Neutron-induced Soft Error Rates and Scaling Trends in SRAM," in *2009 IEEE International Reliability Physics Symposium*, no. 2, pp. 206–211, 2009.

[16] P. Roche, J.-l. Autran, G. Gasiot, and D. Munteanu, "Technology Downscaling Worsening Radiation Effects in Bulk: SOI to the Rescue," *IEDM13-766*, 2013.

[17] G. F. Knoll, *Radiation Detection and Measurement.* John Wiley & Sons, 3rd ed., 2000.

[18] F. Ravotti, "Dosimetry Techniques and Radiation Test Facilities for Total Ionizing Dose Testing," *IEEE Transactions on Nuclear Science*, vol. 65, no. 8, pp. 1440–1464, 2018.

[19] J. Lilley, *Nuclear Physics: Principles and Applications.* John Wiley & Sons, 1st ed., 2001.

[20] N. Arora, *MOSFET Modeling for VLSI Simulation—Theory and Practice.* New Jersey, London: World Scientific, 2007.

[21] D. Pederson, "A historical review of circuit simulation," *IEEE Transactions on Circuits and Systems*, vol. 31, no. 1, pp. 103–111, 1984.

[22] L. W. Nagel and D. . Pederson, "Simulation program with integrated circuit emphasis," in *Proc. 16th Midwest Symp. Circ. Theory,Waterloo, Canada*, 1973.

[23] L. W. Nagel, "SPICE2: A computer program to simulate semiconductor circuits," in *Univ. of California, Berkeley, ERL Memo UCB/ERL M75/520*, 1975.

[24] S. Selberherr and A. Schutz, "MINIMOS: A Two-Dimensional MOS Transistor Analyser," *IEEE Transactions on Electron Devices*, no. 27, pp. 1520–1532, 1980.

[25] C. M. Snowden, “Practical methods of device and circuit modelling,” in *IEEE International Symposium on Circuits and Systems*, 1988.

[26] G. Baccarani, R. Guerrieri, P. Ciampolini, and M. Rudan, “HFIELDS: A Highly Flexible 2-D Semiconductor Device Analysis Program,” in *Proc. NASCODE IV*, 1985.

[27] E. M. Buturla, P. E. Cottrell, B. M. Grossman, and K. Salsburg, “Finite-Element Analysis of Semiconductor Devices: The FIELDAY Program,” *IBM J. Res. Dev.*, no. 25, pp. 218–231, 1981.

[28] S. J. Polak, W. Schilders, and M. Driessen, “The Curry Algorithm,” in *Proc. of 2nd SSDP Conference, Pineridge Press*, 1986.

[29] M. Duane, “The role of TCAD in compact modeling,” in *Workshop on Compact Modeling*, pp. 22–25, 2002.

[30] J.-M. Sallese, “A global approach to model induced minority carrier parasitic currents in HV-MOSFET’s integrated circuits,” *SNSF Project*, 2009.

[31] F. Lo Conte, J.-M. Sallese, M. Pastre, F. Krummenacher, and M. Kayal, “Global Modeling Strategy of Parasitic Coupled Currents Induced by Minority-Carrier Propagation in Semiconductor Substrates,” *IEEE Transactions on Electron Devices*, vol. 57, pp. 263–272, jan 2010.

[32] F. Lo Conte, *Substrate Current Modeling for high Temperature Smart Power BCD Technology.* PhD thesis.

[33] C. Stefanucci, P. Buccella, M. Kayal, and J.-M. Sallese, “Spice-compatible modeling of high injection and propagation of minority carriers in the substrate of Smart Power ICs,” *Solid State Electronics*, vol. 105, pp. 21–29, 2015.

[34] C. Stefanucci, P. Buccella, M. Kayal, and J.-M. Sallese, “Modeling Minority Carriers Related Capacitive Effects for Transient Substrate Currents in Smart Power ICs,” *IEEE Transactions on Electron Devices*, vol. 62, pp. 1215–1222, apr 2015.

[35] P. Buccella, C. Stefanucci, H. Zou, Y. Moursy, R. Iskander, J.-M. Sallese, and M. Kayal, “Methodology for 3-D Substrate Network Extraction for SPICE Simulation of Parasitic Currents in Smart Power ICs,” *IEEE Transactions on Computer-Aided Design of Integrated Circuits and Systems*, vol. 35, pp. 1489–1502, sep 2016.

[36] P. Buccella, *Substrate Current Optimization in Smart Power ICs.* PhD thesis, École polytechnique fédérale de Lausanne (EPFL), 2016.

[37] M. A. Green and M. J. Keevers, “Optical properties of intrinsic silicon at 300 K,” *Progress in Photovoltaics: Research and Applications*, vol. 3, pp. 189–192, 1995.

[38] B. Jacob, B. Witzigmann, M. Klemenc, and C. Petit, “A TCAD methodology for high-speed photodetectors,” *Solid-State Electronics*, vol. 49, pp. 1002–1008, 2005.

[39] M. A. Marwick and A. G. Andreou, “A UV Photodetector with Internal Gain Fabricated in Silicon on Sapphire CMOS,” in *IEEE Sensors Conference*, pp. 535–538, 2007.

[40] J. K. Park and I. Yun, “Modeling of Avalanche Gain for High-speed InP/InGaAs Avalanche Photodiodes,” in *IEEE International Conference on Electron Devices and SOlid-State Circuits*, 2008.

[41] Z. Essa, P. Boulenc, C. Tavernier, F. Hirigoyen, A. Crocherie, J. Michelot, and D. Rideau, “3D TCAD Simulation of Advanced CMOS Image Sensors,” in *IEEE International Conference on Simulation of Semiconductor Processes and Devices*, pp. 187–190, 2011.

[42] V. Sorianello, A. De Iacovo, L. Colace, and G. Assanto, “Near-Infrared Photodetectors in Evaporated Ge: Characterization and TCAD Simulations,” *IEEE Transactions on Electron Devices*, vol. 60, no. 6, pp. 1995–2000, 2013.

[43] J.-B. Lincelles, O. Marcelot, P. Magnan, O. Saint-Pe, and M. Bréart de Boisanger, “Enhanced Near-Infrared Response CMOS Image Sensors Using High-Resistivity Substrate: Photodiodes Design Impact on Performances,” *IEEE Transactions on Electron Devices*, vol. 63, no. 1, pp. 120–127, 2016.

[44] X. Jin, Z. Jiang, and M. Tian, “TCAD simulations of Novel Interrupted-P-Finger UV/Blue Photodiode based on CMOS PROCESS,” in *IEEE International Conference on ASIC (ASICON)*, 2015.

[45] J. Yang, W. Shi, Z. Huang, Y. Xu, Y. Zheng, and X. Fang, “A 320x240-pixel Subcentimeter Resolution Time-of-Flight Image Sensor Design with Structure and Doping Optimized Pinned Photodiode Pixels,” in *IEEE International Conference on Integrated Circuits, Technologies and Applications*, pp. 174–175, 2019.

[46] N. R. Desai., K. V. Hoang, and G. J. Sonek, “Applications of PSPICE Simulation Software to the Study of Optoelectronic Integrated Circuits and Devices,” *IEEE Transactions on Education*, vol. 36, no. 4, pp. 357–362, 1993.

[47] R. Perry and K. Arora, "Using PSPICE to simulate the photoresponse of ideal CMOS integrated circuit photodiodes," in *Proceedings of SOUTHEASTCON*, 1996.

[48] L. Ravezzi, G.-F. Dalla Betta, D. Stoppa, and A. Simoni, "Applications of PSPICE Simulation Software to the Study of Optoelectronic Integrated Circuits and Devices," *Microelectronics Journal*, no. 31, pp. 277–282, 2000.

[49] G. Massobrio and P. Antognetti, *Semiconductor Device Modeling with SPICE*. McGraw-Hill, 2nd ed., 1993.

[50] B. Blanco-Filgueira, P. López, and J. B. Roldán, "A Review of CMOS Photodiode Modeling and the Role of the Lateral Photoresponse," *IEEE Transactions on Electron Devices*, vol. 63, no. 1, pp. 16–25, 2016.

[51] S. U. Ay, "Design issues and performance of large format scien- tific CMOS image sensors,," in *Ph.D. dissertation, Dept. Elect. Eng., Univ. Southern California, Los Angeles, CA, USA*, 2004.

[52] I. Shcherback and O. Yadid-Pecht, "Photoresponse analysis and pixel shape optimization for CMOS active pixel sensors," *IEEE Transactions on Electron Devices*, vol. 50, no. 1, pp. 12–18, 2003.

[53] I. Shcherback, T. Danov, and O. Yadid-Pecht, "A comprehensive CMOS APS crosstalk study: Photoresponse model, technology, and design trends," *IEEE Transactions on Electron Devices*, vol. 51, no. 12, pp. 2033–2041, 2004.

[54] I. Shcherback, T. Danov, and O. Yadid-Pecht, "A comprehensive CMOS APS crosstalk study: Photoresponse model, technology, and design trends," *IEEE Transactions on Electron Devices*, vol. 51, no. 12, pp. 2033–2041, 2004.

[55] B. Blanco-Filgueira, P. López, D. Cabello, E. J., H. Neubauer, and J. Hauer, "Sensitivity of photodiode-based CMOS APS in 0.18 um technology: Peripheral collection and optimum dimension," in *Proc. 23rd Conf. Design Circuits Integr. Syst.*, 2008.

[56] B. Blanco-Filgueira, P. López, D. Cabello, J. Hauer, and H. Neubauer, "Photoresponse model for photodiode-based CMOS APS in 180 nm and 90 nm technologies," in *Proc. 25th Conf. Design Circuits Integr. Syst.*, pp. 37–45, 2010.

[57] T. N. Swe and K. S. Yeo, "An accurate photodiode model for DC and high frequency SPICE circuit simulation," in *Proc. Int. Conf. Modeling Simulation Microsyst. Tech., vol. 1*, pp. 362–365, 2001.

[58] W.-J. Liu, O. T.-C. Chen, L.-K. Dai, P.-K. Weng, K.-H. Huang, and F.-W. Jih, "A CMOS photodiode model," in *Proc. 5th IEEE Int. Workshop Behavioral Modeling Simulation*, pp. 102–105, 2001.

[59] H. Holloway, "Theory of lateral-collection photodiodes," *Journal of Applied Physics*, vol. 49, no. 7, pp. 4264–4269, 1978.

[60] J. S. Lee and R. I. Hornsey, "Photoresponse of photodiode arrays for solid-state image sensors," *J. Vac. Sci. Technol. A, Vac., Surf., Films*, vol. 18, no. 2, pp. 621–625, 2000.

[61] C.-S. S. Lin, B. P. Mathur, and M.-C. F. Chang, "Analytical charge collection and MTF model for photodiode-based CMOS imagers," *IEEE Transaction on Electron Devices*, vol. 49, no. 5, pp. 754–761, 2002.

[62] D. Grois, I. Shcherback, T. Danov, and O. Yadid-Pecht, "Theoretical approach to CMOS APS PSF and MTF modeling—Evaluation," *IEEE Sensors Journal*, vol. 6, no. 1, pp. 118–124, 2006.

[63] A. Alexandra, F. Dadouche, and P. Garda, "Two dimensional model for lateral photodiode," in *Proc. Int. Conf. Design Test Integr. Syst. Nanoscale Technol.*, pp. 294–298, 2006.

[64] T. Naeve, M. Hohenbild, and P. Seegebrecht, "A new analytical compact model for two-dimensional finger photodiodes," *Solid-State Electronics*, vol. 52, no. 2, pp. 299–304, 2008.

[65] V. Dhar and V. Gopal, "Optimum diode geometry in a two-dimensional photovoltaic array," *Optical Engineering*, no. 8, pp. 2022–2030.

[66] B. Blanco-Filgueira, P. López, and J. B. Roldán, "Analytical modelling of size effects on the lateral photoresponse of CMOS photodiodes," *Solid-State Electronics*, vol. 73, pp. 15–20, 2012.

[67] B. Blanco-Filgueira, P. López, J. Doge, M. Suarez, and J. Roldán, "Evidence of the lateral collection significance in small CMOS photo- diodes," in *Proc. IEEE Int. Symp. Circuits Syst. (ISCAS)*, pp. 3098–3101, 2012.

[68] B. Blanco-Filgueira, P. López, and J. B. Roldán, "A Verilog-AMS photodiode model including lateral effects," *Microelectronics Journal*, vol. 43, no. 12, pp. 980–984, 2012.

[69] I. Brouk, Y. Nemirovsky, S. Lachowicz, E. A. Gluszak, S. Hinckley, and K. Eshraghian, "Characterization of crosstalk between CMOS photodiodes," *Solid State Electronics*, vol. 46, no. 1, pp. 53–59, 2002.

[70] B. Blanco-Filgueira, P. López, and J. B. Roldán, "Closed-Form and Explicit Analytical Model for Crosstalk in CMOS Photodiodes," *IEEE Transactions on Electron Devices*, vol. 60, no. 10, pp. 3459–3464, 2013.

[71] I. Djité, M. Estribeau, P. Magnan, G. Rolland, S. Petit, and O. Saint-Pé, "Theoretical Models of Modulation Transfer Function, Quantum Efficiency, and Crosstalk for CCD and CMOS Image Sensors," *IEEE Transactions on Electron Devices*, vol. 59, no. 3, pp. 729–737, 2012.

[72] D. Levy, S. E. Schacham, and I. Kidron, "Three-dimensional analytical simulation of self- and cross-responsivities of photovoltaic detector arrays," *IEEE Transactions on Electron Devices*, vol. 34, no. 10, pp. 2059–2070, 1987.

[73] J. S. Lee, R. I. Hornsey, and D. Renshaw, "Analysis of CMOS photodiodes. II. Lateral photoresponse," *IEEE Transactions on Electron Devices*, vol. 50, no. 5, pp. 1239–1245, 2003.

[74] W. De Soto, S. A. Klein, and W. A. Beckman, "Improvement and validation of a model for photovoltaic array performance," *Solar Energy*, vol. 80, pp. 78–88, 2006.

[75] V. Lo Brano, A. Orioli, G. Ciulla, and A. Di Gangi, "An improved five-parameter model for photovoltaic modules," *Sol Energy Mater Sol Cells*, vol. 94, pp. 1358–1370, 2010.

[76] M. G. Villalva, J. R. Gazoli, and E. R. Filho, "Comprehensive approach to modeling and simulation of photovoltaic arrays," *IEEE Transactions on Power Electronics*, vol. 24, pp. 1198–1208, 2009.

[77] A. N. Celik and N. Acikgoz, "Modelling and experimental verification of the operat- ing current of mono-crystalline photovoltaic modules using four- and five- parameter models," *Applied Energy*, vol. 84, pp. 1–15, 2007.

[78] T. Ma, H. Yang, and L. Lu, "Development of a model to simulate the performance characteristics of crystalline silicon photovoltaic modules/strings/arrays," *Solar Energy*, vol. 79, pp. 31–41, 2014.

[79] J. Bai, S. Liu, Y. Hao, Z. Zhang, M. Jiang, and Y. Zhang, "Development of a new compound method to extract the five parameters of PV modules," *Energy Conversion Management*, vol. 79, pp. 294–303, 2014.

[80] M. A. de Blas, J. L. Torres, E. Prieto, and A. Garcıa, "Selecting a suitable model for characterizing photovoltaic devices," *Renewable Energy*, vol. 25, pp. 371–380, 2002.

[81] J. A. Gow and C. D. Manning, "Development of a photovoltaic array model for use in power-electronics simulation studies," *IEE Proceedings Electric Power Applications*, vol. 146, pp. 193–200, 1999.

[82] J. Hyvarinen and J. Karila, "New analysis method for crystalline silicon cells," in *Proceedings of third world conference on photovoltaic energy conversion*, pp. 1521–1524, 2003.

[83] K.-I. Kurobe and H. Matsunami, "New two-diode model for detailed analysis of multicrystalline silicon solar cells," *Japanese Journal of Applied Physics*, vol. 44, no. 12, 2005.

[84] K. Ishaque, Z. Salam, and Syafaruddin, "A comprehensive MATLAB Simulink PV system simulator with partial shading capability based on two-diode model," *Solar Energy*, vol. 85, pp. 2217–2227, 2011.

[85] J. M. Gee and B. L. Sopori, "The effect of gettering on areal inhomogeneities in large-area multicrystalline-silicon solar cells," in *IEEE 26th Photovoltaic Spec. Conf., Anaheim, CA, USA*, 1997.

[86] D. Grote, M. Kasemann, M. Hermle, and W. Warta, "Analysing lateral inhomogeneities of silicon solar cells using a quasi 3D circuit simulation tool based on SPICE," in *Eur. Photovoltaic Solar Energy Conf., Milan, Italy*, 2007.

[87] P. O. Grabitz, U. Rau, and H. Werner, "Modelling of spatially inhomogeneous solar cells by a multi-diode approach," *Journal of Physica Status Solidi (a)*, vol. 202, no. 15, pp. 2920–2927, 2005.

[88] M. A. Green, "Limiting Efficiency of Bulk and Thin-film Silicon Solar Cells in the Presence of Surface Recombination," *Progress in Photovoltaics: Research and Applications*, vol. 7, pp. 327–330, 1999.

[89] J. Geist, "Silicon photodiode front region collection efficiency models," *Journal of Applied Physics*, vol. 51, pp. 3993–3995, jul 1980.

[90] C. Rossi, P. Buccella, C. Stefanucci, and J. M. Sallese, "Modeling Surface Recombination with Enhanced Devices Network for Optoelectronics," in *2018 16th IEEE International NEWCAS Conference*, pp. 35–39, 2018.

[91] H. Mackel and A. Cuevas, "Determination of the surface recombination velocity of unpassivated silicon from spectral photoconductance measurements," in *3rd World Conference on Photovoltaic Energy Conversion*, pp. 71–74, 2003.

[92] D. Baek, S. Rouvimov, B. Kim, T.-C. Jo, and D. K. Schroder, “Surface recombination velocity of silicon wafers by photoluminescence,” *Applied Physics Letters*, vol. 86, p. 112110, mar 2005.

[93] C. Rossi, P. Buccella, C. Stefanucci, and J.-M. Sallese, “SPICE modeling of light induced current in silicon with ‘Generalized’ lumped devices,” in *2017 47th European Solid-State Device Research Conference (ESSDERC)*, pp. 26–29, 2017.

[94] C. Rossi, P. Buccella, C. Stefanucci, and J.-M. Sallese, “SPICE Modeling of Photoelectric Effects in Silicon with Generalized Devices,” *IEEE Journal of the Electron Devices Society*, vol. 6, pp. 987–995, 2018.

[95] C. Rossi and J. M. Sallese, “Full SPICE Simulation of a CMOS Active Pixel Sensor with Generalized Devices,” in *2019 Latin American Electron Devices Conference (LAEDC)*, 2019.

[96] C. Rossi and J.-M. Sallese, “Simulation of CMOS APS Operation and Crosstalk in SPICE with Generalized Devices,” *IEEE Journal of the Electron Devices Society*, vol. 8, 2020.

[97] C. Rossi and J. M. Sallese, “Prediction of optically triggered amplification in phototransistor with SPICE circuit simulators,” in *Proc. SPIE 11274, Physics and Simulation of Optoelectronic Devices XXVIII, 112740X*, 2020.

[98] J. R. Haynes and W. Shockley, “The Mobility and Life of Injected Holes and Electrons in Germanium,” *Physical Review*, vol. 81, no. 5, 1951.

[99] H. Zimmermann, “Integrated Silicon Optoelectronics,” in *Springer Series in Optical Sciences*.

[100] P. Kostov, W. Gaberl, and H. Zimmermann, “Integrated Phototransistors in a CMOS Process for Optoelectronic Integrated Circuits,” in *2010 Proceedings of the European Solid State Device Research Conference*, pp. 250–253, IEEE, 2010.

[101] K. Y. J. Hsu, K. S. H. Shen, and Y.-S. Chang, “Enhancing the photoresponsivity of bipolar phototransistors for near-infrared detection,” *Appl. Phys. Lett.*, vol. 108, no. 031112, 2016.

[102] S. Vargas-Sierra, E. Roca, and G. Linan-Cembrano, “APS Design Alternatives in 0.18μm CMOS Image Sensor Technology,” *2009 European Conference on Circuit Theory and Design (ECCTD)*, pp. 1–4, 2009.

[103] N. Stevanovic, M. Hillebrand, B. J. Hosticka, and A. Teuner, “A CMOS image sensor for high-speed imaging,” in *Proc. IEEE Solid-State Circuits Conference*, 2000.

[104] T. Reiner, B. Mishori, T. Leitner, A. Horovitz, Y. Vainbaum, M. Hakim, A. Lahav, S. Shapira, and A. Fenigstein, "CMOS image sensor 3T Nwell photodiode pixel SPICE model," *IEEE Convention of Electrical and Electronics Engineers*, pp. 161–164, 2004.

[105] A. El Gamal and H. Eltoukhy, "CMOS Image Sensors," *Circuits and Devices Magazine, IEEE*, vol. 21, no. 3, pp. 6 – 20, 2005.

[106] L. Blockstein and O. Yadid-Pecht, "Crosstalk quantification, analysis, and trends in CMOS image sensors," *Applied Optics*, vol. 49, no. 24, p. 4483, 2010.

[107] H. Tsugawa, H. Takahashi, R. Nakamura, T. Umebayashi, T. Ogita, H. Okano, K. Iwase, H. Kawashima, T. Yamasaki, D. Yoneyama, J. Hashizume, T. Nakajima, K. Murata, Y. Kanaishi, K. Ikeda, K. Tatani, T. Nagano, H. Nakayama, T. Haruta, and T. Nomoto, "Pixel/DRAM/logic 3-layer stacked CMOS image sensor technology," in *International Electron Devices Meeting, IEDM*, vol. 1, pp. 3.2.1–3.2.4, 2018.

[108] S. Sukegawa, T. Umebayashi, T. Nakajima, H. Kawanobe, K. Koseki, I. Hirota, T. Haruta, M. Kasai, K. Fukumoto, T. Wakano, K. Inoue, H. Takahashi, T. Nagano, Y. Nitta, T. Hirayama, and N. Fukushima, "A 1/4-inch 8Mpixel back-illuminated stacked CMOS image sensor," in *Digest of Technical Papers - IEEE International Solid-State Circuits Conference*, vol. 56, pp. 484–485, IEEE, 2013.

[109] V. C. Venezia, A. C.-w. Hsiung, K. Ai, X. Zhao, Z. Lin, D. Mao, A. Yazdani, A. G. Eric, and L. A. Grant, "1.5μm Dual Conversion Gain , Backside Illuminated Image Sensor Using Stacked Pixel Level Connections with 13ke- Full-Well Capacitance and 0 . 8e- Noise," in *IEEE International Electron Devices Meeting (IEDM)*, pp. 10.1.1–10.1.4, IEEE, 2018.

[110] D. N. Yaung, B. C. Hsieh, C. C. Wang, J. C. Liu, T. J. Wang, W. D. Wang, C. C. Chuang, C. Chao, Y. L. Tu, C. S. Tsai, T. L. Hsu, F. Ramberg, W. P. Mo, H. Rhodes, D. Tai, V. C. Venezia, and S. G. Wuu, "High performance 300mm backside illumination technology for continuous pixel shrinkage," *nternational Electron Devices Meeting, IEDM*, pp. 175–178, 2011.

[111] H. Wakabayashi, K. Yamaguchi, M. Okano, S. Kuramochi, O. Kumagai, S. Sakane, M. Ito, M. Hatano, M. Kikuchi, Y. Yamagata, T. Shikanai, K. Koseki, K. Mabuchi, Y. Maruyama, K. Akiyama, E. Miyata, T. Honda, M. Ohashi, and T. Nomoto, "A 1/2.3-inch 10.3Mpixel 50frame/s back-illuminated CMOS image sensor," in *IEEE International Solid-State Circuits Conference*, vol. 53, pp. 410–411, IEEE, 2010.

[112] S. G. Wuu, C. C. Wang, B. C. Hseih, Y. L. Tu, C. H. Tseng, T. H. Hsu, R. S. Hsiao, S. Takahashi, R. J. Lin, C. S. Tsai, Y. P. Chao, K. Y. Chou, P. S. Chou, H. Y. Tu, F. L. Hsueh, and L. Tran, "A leading-edge 0.9μm pixel CMOS image sensor technology with backside illumination: Future challenges for pixel scaling," *nternational Electron Devices Meeting, IEDM*, pp. 332–335, 2010.

[113] Y. Kumagai, R. Yoshita, N. Osawa, H. Ikeda, K. Yamashita, T. Abe, S. Kudo, J. Yamane, T. Idekoba, S. Noudo, Y. Ono, S. Kunitake, M. Sato, N. Sato, T. Enomoto, K. Nakazawa, H. Mori, Y. Tateshita, and K. Ohno, "Back-Illuminated 2.74 μm-Pixel-Pitch Global Shutter CMOS Image Sensor with Charge-Domain Memory Achieving 10k e-Saturation Signal," *International Electron Devices Meeting, IEDM*, pp. 10.6.1–10.6.4, 2018.

[114] W. R. Leo, *Techniques for Nuclear and Particle Physics Experiments, A How-to Approach.* Springer-Verlag Berlin Heidelberg, 1994.

[115] J. F. Ziegler, M. D. Ziegler, and J. P. Biersack, "SRIM - The stopping and range of ions in matter (2010)," *Nuclear Instruments and Methods in Physics Research, Section B: Beam Interactions with Materials and Atoms*, vol. 268, no. 11-12, pp. 1818–1823, 2010.

[116] S. Serre, S. Semikh, S. Uznanski, J. L. Autran, D. Munteanu, G. Gasiot, and P. Roche, "Geant4 Analysis of n-Si Nuclear Reactions From Different Sources of Neutrons and Its Implication on Soft-Error Rate," *IEEE Transactions on Electron Devices*, vol. 59, no. 4, pp. 714–722, 2012.

[117] H. P. Muhlfeld, M. Nicewicz, C. A. Russell, W. Y. Wang, L. B. Freeman, P. Hosier, L. E. Lafave, J. M. Orro, J. M. Ross, O. Gorman, B. Messina, A. J. Sykes, H. Yourke, V. Tolat, A. H. Taber, and R. J. Sussman, "IBM experiments in soft fails in computer electronics (1978-1994)," *IBM Journal of Research and Development*, vol. 40, no. 1, pp. 3–18, 1996.

[118] T. P. Ma and P. V. Dressendorfer, *Ionizing radiation effects in MOS devices and circuits.* John Wiley & Sons, 1989.

[119] J. R. Srour and J. W. Palko, "Displacement Damage Effects in Irradiated Semiconductor Devices," *IEEE Transactions on Nuclear Science*, vol. 60, no. 3, pp. 1740–1766, 2013.

[120] V. Van Lint, "The Physics of Radiation Damage in Particle Detectors," *Nucl. Instruments Methods Phys. Res.*, vol. 253, pp. 453–459, 1987.

[121] J. Loferski and P. Rappaport, "Radiation damage in Ge and Si detected by carrier lifetime changes:Damage thresholds," *Physical Review*, vol. 111, no. 2, pp. 432–439, 1958.

[122] O. L. Curtis, J. W. Cleland, J. H. Crawford, and J. C. Pigg, "Effect of irradiation on the hole lifetime in n-type germanium," *Journal of Applied Physics*, vol. 28, no. 10, pp. 1161–1165, 1957.

[123] M. Nicolaidis, *Soft Errors in Modern Electronic Systems.* Springer, 2011.

[124] S. Agostinelli, J. Allison, K. Amako, J. Apostolakis, H. Araujo, P. Arce, M. Asai, D. Axen, S. Banerjee, G. Barrand, F. Behner, L. Bellagamba, J. Boudreau, L. Broglia, A. Brunengo, H. Burkhardt, S. Chauvie, J. Chuma, R. Chytracek, G. Cooperman, G. Cosmo, P. Degtyarenko, A. Dell'Acqua, G. Depaola, D. Dietrich, R. Enami, A. Feliciello, C. Ferguson, H. Fesefeldt, G. Folger, F. Foppiano, A. Forti, S. Garelli, S. Giani, R. Giannitrapani, D. Gibin, J. J. Gomez Cadenas, I. Gonzalez, G. Gracia Abril, G. Greeniaus, W. Greiner, V. Grichine, A. Grossheim, S. Guatelli, P. Gumplinger, R. Hamatsu, K. Hashimoto, H. Hasui, A. Heikkinen, A. Howard, V. Ivanchenko, A. Johnson, F. W. Jones, J. Kallenbach, N. Kanaya, M. Kawabata, Y. Kawabata, M. Kawaguti, S. Kelner, P. Kent, A. Kimura, T. Kodama, R. Kokoulin, M. Kossov, H. Kurashige, E. Lamanna, T. Lampen, V. Lara, V. Lefebure, F. Lei, M. Liendl, W. Lockman, F. Longo, S. Magni, M. Maire, E. Medernach, K. Minamimoto, P. Mora de Freitas, Y. Morita, K. Murakami, M. Nagamatu, R. Nartallo, P. Nieminen, T. Nishimura, K. Ohtsubo, M. Okamura, S. O'Neale, Y. Oohata, K. Paech, J. Perl, A. Pfeiffer, M. G. Pia, F. Ranjard, A. Rybin, S. Sadilov, E. di Salvo, G. Santin, T. Sasaki, N. Savvas, Y. Sawada, S. Scherer, S. Sei, V. Sirotenko, D. Smith, N. Starkov, H. Stoecker, J. Sulkimo, M. Takahata, S. Tanaka, E. Tcherniaev, E. Safai Tehrani, M. Tropeano, P. Truscott, H. Uno, L. Urban, P. Urban, M. Verderi, A. Walkden, W. Wander, H. Weber, J. P. Wellisch, T. Wenaus, D. C. Williams, D. Wright, T. Yamada, H. Yoshida, and D. Zschiesche, "GEANT4 - A simulation toolkit," *Nuclear Instruments and Methods in Physics Research, Section A: Accelerators, Spectrometers, Detectors and Associated Equipment*, vol. 506, no. 3, pp. 250–303, 2003.

[125] R. A. Reed, R. A. Weller, A. Akkerman, J. Barak, W. Culpepper, S. Duzellier, C. Foster, M. Gaillardin, G. Hubert, T. Jordan, I. Jun, S. Koontz, F. Lei, P. McNulty, M. H. Mendenhall, M. Murat, P. Nieminen, P. O'Neill, M. Raine, B. Reddell, F. Saigné, G. Santin, L. Sihver, H. H. K. Tang, P. R. Truscott, and F. Wrobel, "Anthology of the development of radiation transport tools as applied to single event effects," *IEEE Transactions on Nuclear Science*, vol. 60, no. 3, pp. 1876–1911, 2013.

[126] P. Roche, G. Gasiot, J. L. Autran, D. Munteanu, R. A. Reed, and R. A. Weller, "Application of the TIARA radiation transport tool to single event effects simulation," *IEEE Transactions on Nuclear Science*, vol. 61, no. 3, pp. 1498–1500, 2014.

[127] M. Glorieux, J. L. Autran, D. Munteanu, S. Clerc, G. Gasiot, and P. Roche, "Random-walk drift-diffusion charge-collection model for reverse-biased junctions embedded in circuits," *IEEE Transactions on Nuclear Science*, vol. 61, no. 6, pp. 3527–3534, 2014.

[128] S. Uznanski, G. Gasiot, P. Roche, S. Semikh, and J. L. Autran, "Combining GEANT4 and TIARA for neutron soft error-rate prediction of 65 nm flip-flops," *IEEE Transactions on Nuclear Science*, vol. 58, no. 6 PART 1, pp. 2599–2606, 2011.

[129] J.-l. Autran, S. Semikh, D. Munteanu, S. Serre, G. Gasiot, and P. Roche, "Soft-Error Rate of Advanced SRAM Memories : Modeling and Monte Carlo Simulation," in *Numerical Simulation – From Theory to Industry neutrons, Vienna: InTech 2012*, pp. 309–336, 2012.

[130] Q. Wang, H. Liu, S. Wang, and S. Chen, "Tcad simulation of single-event-transient effects in l-shaped channel tunneling field-effect transistors," *IEEE Transactions on Nuclear Science*, vol. 65, no. 8, pp. 2250–2259, 2018.

[131] A. Michez, S. Dhombres, and J. Boch, "Ecorce: A tcad tool for total ionizing dose and single event effect modeling," *IEEE Transactions on Nuclear Science*, vol. 62, no. 4, pp. 1516–1527, 2015.

[132] K. Tanaka, H. Nakamura, T. Uemura, K. Takeuchi, T. Fukuda, and S. Kumashiro, "Study on influence of device structure dimensions and profiles on charge collection current causing set pulse leading to soft errors in logic circuits," in *2009 International Conference on Simulation of Semiconductor Processes and Devices*, pp. 1–4, 2009.

[133] B. Narasimham, R. L. Shuler, J. D. Black, B. L. Bhuva, R. D. Schrimpf, A. F. Witulski, W. T. Holman, and L. W. Massengill, "Quantifying the reduction in collected charge and soft errors in the presence of guard rings," *IEEE Transactions on Device and Materials Reliability*, vol. 8, no. 1, pp. 203–209, 2008.

[134] G. Kaushal, S. S. Rathod, S. Maheshwaram, S. K. Manhas, A. K. Saxena, and S. Dasgupta, "Radiation effects in si-nw gaa fet and cmos inverter: A tcad simulation study," *IEEE Transactions on Electron Devices*, vol. 59, no. 5, pp. 1563–1566, 2012.

[135] C. Gao, Y. Xiong, and J. Huang, "Modeling of nmos transistors for simulation of atmospheric neutron environment and sees on sram-based fpgas," in *2016 Prognostics and System Health Management Conference (PHM-Chengdu)*, pp. 1–5, 2016.

[136] D. R. Ball, M. L. Alles, R. D. Schrimpf, and S. Cristoloveanu, "Comparing single event upset sensitivity of bulk vs. soi based finfet sram cells using tcad simulations," in *2010 IEEE International SOI Conference (SOI)*, pp. 1–2, 2010.

[137] L. Artola, G. Hubert, and M. Alioto, "Comparative soft error evaluation of layout cells in finfet technology," *Microelectronics Reliability*, vol. 54, no. 9, pp. 2300 – 2305, 2014. SI: ESREF 2014.

[138] K. Yamada, H. Maruoka, J. Furuta, and K. Kobayashi, "Sensitivity to soft errors of nmos and pmos transistors evaluated by latches with stacking structures in a 65 nm fdsoi process," in *2018 IEEE International Reliability Physics Symposium (IRPS)*, pp. P–SE.3–1–P–SE.3–5, 2018.

[139] R. Naseer, Y. Boulghassoul, J. Draper, S. DasGupta, and A. Witulski, "Critical charge characterization for soft error rate modeling in 90nm sram," in *2007 IEEE International Symposium on Circuits and Systems*, pp. 1879–1882, 2007.

[140] P. E. Dodd and L. W. Massengill, "Basic mechanisms and modeling of single-event upset in digital microelectronics," *IEEE Transactions on Nuclear Science*, vol. 50, no. 3, pp. 583–602, 2003.

[141] A. Fedoseyev, R. Arslanbekov, and M. Turowski, "Mixed-mode simulations of ics with complex nuclear events from mred/geant4 with 3d tcad," in *2009 MIXDES-16th International Conference Mixed Design of Integrated Circuits Systems*, pp. 468–471, 2009.

[142] Y. Fang and A. S. Oates, "Thermal neutron-induced soft errors in advanced memory and logic devices," *IEEE Transactions on Device and Materials Reliability*, vol. 14, no. 1, pp. 583–586, 2014.

[143] Y. Kawakami, M. Hane, H. Nakamura, T. Yamada, and K. Kumagai, "Investigation of soft error rate including multi-bit upsets in advanced sram using neutron irradiation test and 3d mixed-mode device simulation," in *IEDM Technical Digest. IEEE International Electron Devices Meeting, 2004.*, pp. 945–948, 2004.

[144] F. L. Yang and R. A. Saleh, "Simulation and analysis of transient faults in digital circuits," *IEEE Journal of Solid-State Circuits*, vol. 27, no. 3, pp. 258–264, 1992.

[145] S. Yoshimoto, T. Amashita, S. Okumura, K. Yamaguchi, M. Yoshimoto, and H. Kawaguchi, "Bit error and soft error hardenable 7t/14t sram with 150-nm fd-soi process," in *2011 International Reliability Physics Symposium*, pp. SE.3.1–SE.3.6, 2011.

[146] P. E. Dodd, "Physics-Based Simulation of Single-Event Effects," *IEEE Transactions on Device and Materials Reliability*, vol. 5, no. 3, pp. 343–357, 2005.

[147] N. Rostand, S. Martinie, J. Lacord, O. Rozeau, O. Billoint, J.-C. Barbé, T. Poiroux, and G. Huber, "Compact Modelling of Single Event Transient in Bulk MOSFET for SPICE: Application to Elementary Circuit," in *International Conference on Simulation of Semiconductor Processes and Devices (SISPAD)*, pp. 364–368, IEEE, 2018.

[148] G. C. Messenger, "Collection of Charge on Junction Nodes from ion tracks," *IEEE Transactions on Nuclear Science*, vol. NS-29, no. 6, pp. 2024–2031, 1982.

[149] R. Naseer, Y. Boulghassoul, J. Draper, S. DasGupta, and A. Witulski, "Critical Charge Characterization for Soft Error Rate Modeling in 90nm SRAM," in *IEEE International Symposium on Circuits and Systems*, pp. 1879–1882, 2007.

[150] J. Yang, P. Wang, Y. Zhang, Y. Cheng, W. Zhao, S. Member, Y. Chen, and H. H. Li, "Radiation-Induced Soft Error Analysis of STT-MRAM : A Device to Circuit Approach," *IEEE Transactions on Computer-Aided Design of Integrated Circuits and Systems*, vol. 35, no. 3, pp. 380–393, 2016.

[151] H. Huang and C. H. . Wen, "Layout-based soft error rate estimation framework considering multiple transient faults—from device to circuit level," *IEEE Transactions on Computer-Aided Design of Integrated Circuits and Systems*, vol. 35, no. 4, pp. 586–597, 2016.

[152] K. Mohanram, "Closed-form simulation and robustness models for seu-tolerant design," in *23rd IEEE VLSI Test Symposium (VTS'05)*, pp. 327–333, 2005.

[153] R. Naseer, Y. Boulghassoul, J. Draper, S. DasGupta, and A. Witulski, "Critical charge characterization for soft error rate modeling in 90nm sram," in *2007 IEEE International Symposium on Circuits and Systems*, pp. 1879–1882, 2007.

[154] A. Dharchoudhury, S. M. Kang, H. Cha, and J. H. Patel, "Fast timing simulation of transient faults in digital circuits," in *IEEE/ACM International Conference on Computer-Aided Design*, pp. 719–726, 1994.

[155] N. Rostand, S. Martinie, J. Lacord, O. Rozeau, O. Billoint, J. Barbé, T. Poiroux, and G. Hubert, "Compact modelling of single event transient in bulk mosfet for spice: Application to elementary circuit," in *2018 International Conference on Simulation of Semiconductor Processes and Devices (SISPAD)*, pp. 364–368, 2018.

[156] H. T. Nguyen and Y. Yagil, "A systematic approach to ser estimation and solutions," in *2003 IEEE International Reliability Physics Symposium Proceedings, 2003. 41st Annual.*, pp. 60–70, 2003.

[157] L. Artola, G. Hubert, K. M. Warren, M. Gaillardin, R. D. Schrimpf, R. A. Reed, R. A. Weller, J. R. Ahlbin, P. Paillet, M. Raine, S. Girard, S. Duzellier, L. W. Massengill, and F. Bezerra, "Seu prediction from set modeling using multi-node collection in bulk transistors and srams down to the 65 nm technology node," *IEEE Transactions on Nuclear Science*, vol. 58, no. 3, pp. 1338–1346, 2011.

[158] G. Hubert, J. . Palau, K. Castellani-Coulie, M. . Calvet, and S. Fourtine, "Detailed analysis of secondary ions' effect for the calculation of neutron-induced ser in srams," *IEEE Transactions on Nuclear Science*, vol. 48, no. 6, pp. 1953–1959, 2001.

[159] R. Ramanarayanan, V. S. Degalahal, R. Krishnan, J. Kim, V. Narayanan, Y. Xie, M. J. Irwin, and K. Unlu, "Modeling soft errors at the device and logic levels for combinational circuits," *IEEE Transactions on Dependable and Secure Computing*, vol. 6, no. 3, pp. 202–216, 2009.

[160] T. Misawa, "A Note on the Extended Theory of the Junction Transistor," *Journal of the Physical Society of Japan*, vol. 11, no. 7, pp. 728–739, 1956.

[161] C. M. Hsieh, P. C. Murley, and R. R. O'Brien, "Dynamics of Charge Collection from Alpha-Particle Tracks in Integrated Circuits," *19th International Reliability Physics Symposium*, pp. 38–42, 1981.

[162] S. Martinie, T. Saad-Saoud, S. Moindjie, D. Munteanu, and J. L. Autran, "Behavioral modeling of SRIM tables for numerical simulation," *Nuclear Instruments and Methods in Physics Research, Section B: Beam Interactions with Materials and Atoms*, vol. 322, pp. 2–6, 2014.

[163] C. Hsieh, P. Murley, and R. O'Brien, "A field-funneling effect on the collection of alpha-particle-generated carriers in silicon devices," *IEEE Electron Device Letters*, vol. 2, no. 4, pp. 2–4, 1981.

[164] P. E. Dodd, "Device Simulation of Charge Collection and Single-Event Upset," *IEEE Transactions on Nuclear Science*, vol. 43, pp. 561–575, 1996.

[165] P. E. Dodd, F. W. Sexton, and P. S. Winkour, “Three-dimensional simulation of charge collection and multiple-bit upset in Si devices,” *IEEE Transactions on Nuclear Science*, vol. 41, no. 6, pp. 2005–2017, 1994.

[166] F. Wang and V. D. Agrawal, “Single Event Upset : An Embedded Tutorial,” in *21st International Conference on VLSI Design 21st International Conference on VLSI Design Single*, pp. 429–434, 2008.

[167] F. B. McLean and T. R. Oldham, “Charge Funneling in N- and P-Type Si Substrates,” *IEEE Transactions on Nuclear Science*, vol. 29, no. 6, pp. 2017–2023, 1982.

[168] C. Rossi and J.-M. Sallese, “SPICE Simulation of Radiation Induced Charges and Currents in Silicon Substrate,” in *2020 IEEE Latin America Electron Devices Conference (LAEDC)*, 2020.

List of publications

C. Rossi, P. Buccella, C. Stefanucci, J.-M. Sallese, “SPICE Modeling of Light Induced Charges and Currents in Silicon with Generalized Lumped Device”, *47th European Solid-State Device Research Conference (ESSDERC)*, 2017, Online available.

C. Rossi, P. Buccella, C. Stefanucci, J.-M. Sallese„ “SPICE Modeling of Photoelectric Effects in Silicon with Generalized Devices”, *IEEE Journal of the Electron Devices Society*, vol. 6, pp. 987-995, 2018, Online available.

C. Rossi, P. Buccella, C. Stefanucci, J.-M. Sallese, “Modeling Surface Recombination with Enhanced Devices Network for Optoelectronics”, *16th IEEE International New Circuits and Systems Conference (NEWCAS)*, 2018, Online available.

C. Rossi, J.-M. Sallese, “Full SPICE Simulation of a CMOS Active Pixel Sensor with Generalized Devices”, *Latin American Electron Devices Conference (LAEDC)*, 2019, Online available.

C. Rossi, J.-M. Sallese„ “Simulation of CMOS APS Operation and Crosstalk in SPICE with Generalized Devices”, *IEEE Journal of the Electron Devices Society*, vol. 8, pp. 376-384, 2019, Online available.

C. Rossi, J.-M. Sallese, “Prediction of optically-triggered amplification in phototransistor with SPICE circuit simulators”, *SPIE Photonic West OPTO, Physics and Simulation of Optoelectronic Devices XXVIII, 112740X*, 2020, Online available.

C. Rossi, J.-M. Sallese, “SPICE Simulation of Radiation Induced Charges and Currents in Silicon Substrate”, *Latin American Electron Devices Conference (LAEDC)*, 2020, Online available.

C. Rossi, A. Chatel, J.-M. Sallese, “Modeling Funneling Effect with Generalized Devices for SPICE Simulation of Soft Errors”, submitted to *IEEE Transaction on Electron Devices.*

Chiara Rossi

chiararossi1993@gmail.com
Date of birth 18/04/1993
Nationality Italian
OrcID https://orcid.org/0000-0001-6976-7486

Research Experience

11/2016 - 11/2020

PhD student at EPFL

Laboratory of Electron Device Modeling and Technology (EDLAB)

Development of a novel approach for SPICE-compatible modeling of charge generation, transport and collection in a semiconductor substrate, using the so-called Generalized Devices, for simulation of optoelectronic devices and radiation-induce soft errors in ICs.

02/2016 - 08/2016

Master Thesis at CERN

Experimental Physics department, Detector Technology group

Design, TCAD numerical simulation, fabrication in cleanroom and characterization of a metal-semiconductor-metal photodetector for light detection in microfluidic scintillation detectors, novel particle detectors under investigation at CERN Experimental Physics Department.

06/2015 - 08/2015

Summer Intern at EPFL

Laboratory of Microsystem 2

Design and optimization, using COMSOL and analytical modeling, of a novel pumping system to replace the syringe pumps for liquid circulation in a microfluidic platform used in long-term multiplexed analyses on Caenorhabditis elegans nematodes.

Education

09/2014 - 10/2016

Master's Degree in Micro and Nano technologies for Integrated Systems

École Polytechnique Fédérale de Lausanne (EPFL), Politecnico Di Torino, Grenoble Institut Nationaux Polytechnique (INP) - Phelma

Core topics: Nanoelectronics, MEMS, Solid State Physics and Semiconductor Physics, Electronic Devices, Technological Processes for Integrated Circuits, Digital and Analog Electronics, EDA based design (full-custom digital and analog design and semi-custom digital design)

Overall Grade: 110/110 (cum laude)

09/2011 - 10/2014

Bachelor's Degree in Physics Engineering

Politecnico Di Torino

Core topics: Electronic Devices, Analog Electronics, Semiconductor Physics, Solid State Physics, Quantum Mechanics, Electronic Measurements

Overall Grade: 110/110

Recognitions

- Best Poster Award, EPFL Microsystems and Microelectronics Doctoral School
- LAEDC Conference reviewer and session chair
- ERASMUS scholarship
- Scholarships from the excellent students residence Collegio Universitario R. Einaudi di Torino: "Mobility scholarship" and "one year free rent"

Skills

- Programming Languages: Verilog-A, Matlab, C, LabVIEW, VHDL
- CAD and Simulations: Sentaurus TCAD, Cadence Virtuoso, Spectre, Silvaco TCAD, COMSOL
- Text processing / Spreadsheets: LaTeX, Origin, Office
- Microfabrication in cleanroom
- Device characterization: optical microscopy, scanning electron microscopy, electrical characterizations